

High performance photonic probes and applications of optical tweezers to molecular motors

DISSERTATION

zur Erlangung des akademischen Grades
Doctor rerum naturalium
(Dr. rer. nat.)

an der Fakultät Mathematik und Naturwissenschaften
der Technischen Universität Dresden
vorgelegt von

Dipl. Phys. Anita Jannasch

geboren am 07. November 1982
in Königs Wusterhausen

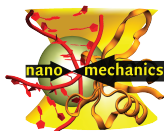
Dresden, im Juni 2012

1. Gutachter: Prof. Jonathon Howard, PhD

*Max Planck Institute of Molecular Cell Biology and Genetics (MPI-CBG)
Pfotenhauerstrasse 108, 01307 Dresden, Germany*

2. Gutachter: Prof. Dr. Stefan Diez

*B CUBE, TU Dresden
Arnoldstrasse 18, 01307 Dresden, Germany*



Die Doktorarbeit wurde unter der Aufsicht von Dr. Erik Schäffer in der Nanomechanics Gruppe am Biotechnologischen Zentrum (BIOTEC) der Technischen Universität Dresden durchgeführt.

Declaration

I herewith declare that I have produced this paper without the prohibited assistance of third parties and without making use of aids other than those specified; notions taken over directly or indirectly from other sources have been identified as such. This paper has not previously been presented in identical or similar form to any other German or foreign examination board.

The thesis work was conducted from September 2008 to June 2012 under the supervision of Dr. Erik Schäffer at the Biotechnology Center (BIOTEC) of the Technical University Dresden.

I declare that I have not undertaken any previous unsuccessful doctorate proceedings. I declare that I recognize the doctorate regulations of the Fakultät für Mathematik und Naturwissenschaften of the Technische Universität Dresden.

Erklärung

Hiermit versichere ich, dass ich die vorliegende Arbeit ohne unzulässige Hilfe Dritter und ohne Benutzung anderer als der angegebenen Hilfsmittel angefertigt habe; die aus fremden Quellen direkt oder indirekt übernommenen Gedanken sind als solche kenntlich gemacht. Die Arbeit wurde bisher weder im Inland noch im Ausland in gleicher oder ähnlicher Form einer anderen Prüfungsbehörde vorgelegt.

Die Doktorarbeit wurde von September 2008 bis Juni 2012 unter der Aufsicht von Dr. Erik Schäffer am Biotechnologischen Zentrum (BIOTEC) der Technischen Universität Dresden durchgeführt.

Hiermit erkläre ich, dass keine früheren Promotionsverfahren stattgefunden haben. Hiermit erkläre ich, dass ich die Promotionsordnung der Fakultät für Mathematik und Naturwissenschaften an der Technischen Universität Dresden anerkenne.

Anita Jannasch

Dresden, im Juni 2012

Abstract

Optical tweezers are a sensitive position and force transducer widely employed in physics and biology. In a focussed laser, forces due to radiation pressure enable to trap and manipulate small dielectric particles used as probes for various experiments. For sensitive biophysical measurements, microspheres are often used as a handle for the molecule of interest. The force range of optical traps well covers the piconewton forces generated by individual biomolecules such as kinesin molecular motors. However, cellular processes are often driven by ensembles of molecular machines generating forces exceeding a nanonewton and thus the capabilities of optical tweezers. In this thesis I focused, first, on extending the force range of optical tweezers by improving the trapping efficiency of the probes and, second, on applying the optical tweezers technology to understand the mechanics of molecular motors. I designed and fabricated photonic-structured probes: Anti-reflection-coated, high-refractive-index, core-shell particles composed of titania. With these probes, I significantly increased the maximum optical force beyond a nanonewton. These particles open up new research possibilities in both biology and physics, for example, to measure hydrodynamic resonances associated with the colored nature of the noise of Brownian motion. With respect to biophysical applications, I used the optical tweezers to study the mechanics of single kinesin-8. Kinesin-8 has been shown to be a very processive, plus-end directed microtubule depolymerase. The underlying mechanism for the high processivity and how stepping is affected by force is unclear. Therefore, I tracked the motion of yeast (Kip3) and human (Kif18A) kinesin-8s with high precision under varying loads. We found that kinesin-8 is a low-force motor protein, which stalled at loads of only 1 pN. In addition, we discovered a force-induced stick-slip motion, which may be an adaptation for the high processivity. Further improvement in optical tweezers probes and the instrument will broaden the scope of feasible optical trapping experiments in the future.

Ein Gelehrter in seinem Laboratorium ist nicht nur ein Techniker; er steht auch vor den Naturgesetzen wie ein Kind vor der Märchenwelt.

Marie Curie

Contents

1. Overview	1
1. Advanced optical tweezers	3
2. Principles of optical tweezers	5
2.1. Light carries momentum	5
2.2. Physics of trapping particles	6
2.2.1. Light scattering by particles	6
2.2.2. Optical tweezers toolbox	7
2.3. Optical tweezers setups	9
2.3.1. MPI-CBG setup	9
2.3.2. 'Aswad'	11
2.3.3. 'Pinky'	12
2.3.4. Flow cell	13
2.4. Calibration with positional detection in the back focal plane	15
3. Complete force field of an optical trap	17
3.1. Introduction	17
3.2. Measurement of the complete force field of an optical trap	18
3.3. Calculation of the complete force field of an optical trap	19
3.3.1. Mie theory calculations of the force map	19
3.3.2. Comparison between theory and experiments	19
3.4. Discussion	21
4. Nanonewton optical forces by trapping anti-reflection-coated titania microspheres	23
4.1. Maximum force of optical tweezers limits their applicability	23
4.2. Methods	24
4.2.1. Anti-reflection coating	24
4.2.2. Parameters for calculations	25
4.2.3. Optical tweezers setup	25
4.2.4. Sample preparation & calibration	25

4.3. Theory predicts nanonewton optical forces with anti-reflection coated titania microspheres	26
4.4. Synthesis of anti-reflection coated titania microspheres	28
4.5. High trap stiffness with anti-reflection coated titania microspheres	30
4.6. Nanonewton forces with anti-reflection coated titania microspheres	32
4.7. Discussion	34
5. Colored nature of the thermal noise of Brownian motion	37
5.1. Noise of Brownian motion	37
5.2. Ultra-stable trap and anti-reflection coated titania microspheres to measure the colored noise of Brownian motion	38
5.3. The noise of Brownian motion is colored	39
5.4. Discussion	42
II. Kinesin-8	45
6. Introduction	47
6.1. Biological background	47
6.1.1. Microtubules are important structures in cells	47
6.1.2. Kinesins are microtubule based motor proteins	48
6.2. Motivation	49
7. Kinesin-8 assay	51
7.1. Expression and purification of kinesin-8	51
7.2. Coupling of kinesin to PS microspheres	52
7.3. Stepping assay	54
7.3.1. Sample Preparation	54
7.3.2. TIRF assay	55
7.3.3. Optical tweezers assay	55
7.4. The kinesin-microsphere coupling is functional	55
7.5. Single-molecule conditions	56
7.6. Force feedback	57
8. Kinesin-8 is a low-force motor protein with a weakly-bound slip state	59
8.1. Kinesin-8 is a slow and weak motor protein	59
8.2. Kinesin-8 moves in 8 nm steps	61
8.3. Kinesin-8 slips on microtubules under load	63
8.4. Discussion	66
9. Outlook	69
A. Protocols	73
A.1. Titania particles synthesis	73

A.2. PS-PEG-anti-eGFP microspheres	74
A.3. Kinesin-8 stepping assay	75
Abbreviations	79
List of figures	82
List of tables	84
Contributions	87
Publications related to this thesis	89
Bibliography	91

Chapter 1

Overview

The thesis is separated into two parts. Each chapter within the parts has a separate abstract and introduction. In the first part, I focused on optical tweezers development and novel optimal tweezers probes. In the second part, I performed single-molecule mechanical measurements with the kinesin-8 motor proteins. With respect to the first part, I started to build an optical tweezers setup, called 'Pinky', together with Avin Ramayia. Apart from designing and building Pinky, I used several optical tweezers setups for the different measurements. A brief introduction to optical tweezers and the used setups is given in Chapter 2.

The applicability of optical tweezers is limited by the maximum force that can be generated. Together with Marcus Jahnel and Martin Behrndt (Grill group, MPI-CBG Dresden), we characterized the full nonlinear force and displacement response of an optical trap in two dimensions (2D) (Chapter 3). Only close to the trap center, this field is typically approximated as linear. Exact mapping of the complete optical force field enables the use of the full non-linear force range of an optical trap. In this manner, higher forces can be measured by the same laser intensity.

In order to increase the maximum force that can be generated by optical tweezers, I designed, synthesized and characterized anti-reflection-coated, high-refractive-index, core-shell particles composed of titania (Chapter 4). High-refractive index particles cannot be trapped in a single beam unless they are photonically structured to reduce the scattering force—in the simplest case, coated with an anti-reflection layer. With these probes, increased the maximum optical force in our optimized setup beyond a nanonewton.

Together with Mohammed Mahamdeh, we used the high trap stiffness of the anti-reflection-coated titania particles in combination with our ultra-stabil optical trap to measure the noise of Brownian motion (Chapter 5). The Brownian force acting on the particles is often approximated in Langevin models by a “white-noise” process. However, fluid entrainment results in a frequency dependence of this thermal force giving it a “color”. While theoretically well understood, direct experimental evidence for this colored nature of the noise term was still lacking.

In the second part of my thesis I used optical tweezers to characterize the mechanics of kinesin-8. Kinesin-8 is a highly conserved, microtubule plus-end-directed motor protein that plays an important role during mitosis. The kinesin assay is described in Chapter 7.

I tracked the motion of yeast (Kip3) and human (Kif18A) kinesin-8s with high precision under varying loads. The results are presented in Chapter 8.

In the last chapter (Chapter 9) of my thesis, I give a short outlook.

Part I.

Advanced optical tweezers

Chapter 2

Principles of optical tweezers

Tractor beams, known from 'Star Trek' are no longer science fiction. The real-world analogue to the tractor beam is called optical tweezers. Optical tweezers have become a powerful tool to study the physics and chemistry of life and thereby revolutionized the single-molecule biophysics. High-resolution experiments are feasible that were pure fiction only two decades ago.

2.1. Light carries momentum

Light carries momentum. This was first realized by Kepler in 1619 [1]. In 1873, Maxwell supplied the theoretical evidence that light itself can exert an optical force [2]. In 1901, Hull and Lebedev [3, 4] succeeded in the first experimental detection of a radiation pressure on macroscopic objects. Arthur Ashkin was the first who used this effect to trap particles by a focused laser in 1986 [5, 6]. Ashkin and co-workers employed optical trapping from manipulating live bacteria and viruses [7, 8] to the cooling and trapping of neutral atoms [9, 10]. Since then, optical tweezers have developed into a very powerful tool and are widely employed in biophysics, colloid research, micro-rheology, and physics [11–17].

By using light to trap microscopic objects non-invasively, optical tweezers provide a sensitive position and force transducer. For many experiments, trapped microspheres are the object of interest or are used as handles for the measurements. In practice, forces up to several hundred piconewton with sub-piconewton resolution and sub-nanometer displacements are feasible [18–23]. This is the range for exerting forces on biological systems like single biopolymers (such as DNA), cell membranes, molecular motors (such as myosin, kinesin) *et cetera* [15].

In this chapter I will give a short introduction to the physics of trapping, the used optical tweezers setups and our calibration method.

2.2. Physics of trapping particles

2.2.1. Light scattering by particles

How is a particle trapped in a focused beam and how can we calculate the forces acting on the particles? To answer this questions it is necessary to understand the interaction of light with particles. When incident light interacts with a particle some is scattered in a variety of directions, while some may be absorbed. Both effects transfer momentum from the incident photons onto the particle. Due to the conservation of momentum, an optical force acts on the particle.

In a simplified picture, the force decomposes into an attractive gradient force in the direction of the light gradient pointing toward the focus and a scattering force in the direction of light propagation [11]. The laser traps the particle when the gradient force is large enough to overcome the scattering force, the effective weight, and the thermal fluctuations of the particle. The calculation of the optical force on a particle is relatively straightforward in the regime, where the particle diameter d is either much smaller (Rayleigh regime) [24] or much larger (ray optics) [25] than the wavelength λ of the laser. The typical size range of trapped particles in optical tweezers is between the geometric optic ($\lambda \ll d$) and the Rayleigh scattering regime ($\lambda \gg d$). Therefore, the treatment is a problem in electromagnetic theory. The scattering of a plane wave by a spherical particle can be calculated exactly using Mie theory [26, 27].

Geometric optics When the radius of the particle is much larger than the wavelength of the trapping laser, the conditions for geometrical optics are satisfied. Thus, the optical forces can be computed from ray optics (Fig. 2.1). When a light ray impinges on a sphere, the ray is refracted two times according to Snell's law. If the particle has a different refractive index compared to the surrounding medium, the momentum of the light ray changes. This change in momentum is transferred onto the particle because of the conservation of momentum. A laser beam can be described as a collection of light rays weighted according to their intensity. For the calculation of the total optical force, the momentum transfer of all rays must be summed. When the particle has a refractive index higher than the medium, the gradient force acts in the direction of highest intensity. The scattering force arises from the rays that are reflected at the interface of the particle to the medium [11].

Rayleigh scattering Rayleigh scattering, named after Lord Rayleigh, is the scattering of light by particles much smaller than the wavelength of the incident light [28]. He calculated forces on such a particle by treating the particle as an induced point dipole that scatters light elastically. Through absorption and re-radiation of the light from the trapping beam, a scattering force is exerted on the induced dipole. If the induced dipole is in an electromagnetic field with an intensity gradient, the particle also experience a gradient force, the so-called Lorentz force. The gradient force is directed toward the highest light intensity point. The scattering force strongly depends on the diameter d of the particle ($F_{scat} \propto d^6$). The gradient force increase only with $F_{grad} \propto d^3$. Therefore, the trap should becomes unstable for larger particles [28].

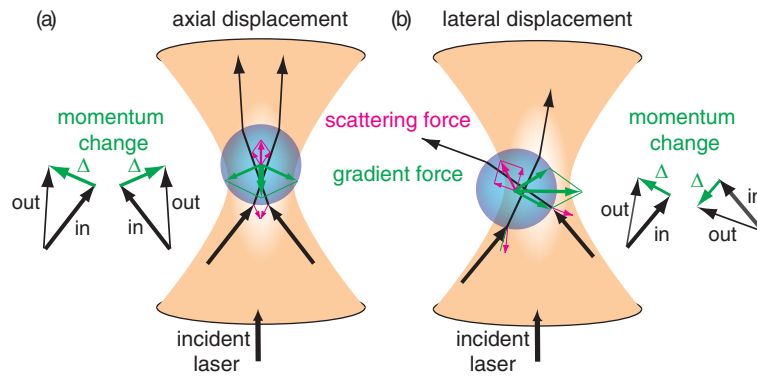


Figure 2.1.: *Geometric optics description of gradient and scattering force.* A transparent, dielectric particle is trapped by a focused laser beam. Two representative rays with their intensities (represented by black lines of different thickness) are shown. The incoming rays are refracted two times. Thereby the momentum is changed. This is illustrated by the difference Δ of the momentum of the entering (in) and leaving ray (out) (vector diagram in (a) and (b)). Due to the conservation of momentum, the momentum of the particle changes by an equal but opposite amount, which results in a **gradient force** depicted by the green arrows. In (a) the particle is displaced above the light focus. The change in momentum leads to an axial force toward the focus point of the laser. In (b) the particle is displaced laterally, which leads to a lateral force, also acting in the direction of highest light intensity. (a), (b) The incoming rays are also reflected (magenta arrows). This leads to the so-called **scattering force**, which acts in the propagation direction and therefore destabilize the trap.

Lorenz-Mie theory When the dimension of the trapped particle is comparable to the wavelength of the laser, neither the ray optics nor the point-dipole approach in the Rayleigh regime are valid. In the electro-magnetic theory, trapping is a scattering problem. An electro-magnetic field incident on a scatterer creates a field inside the scatterer and a field outside the scatterer. If we know the three fields and the scattering cross section, we can calculate the optical forces.

The Lorenz-Mie theory gives an analytical solution for how a *plane wave* is scattered by a spherical particle [29–31]. In this theory, the electric and magnetic fields are calculated by solving the Helmholtz wave equations. The incident and scattered waves are expressed as sums of vector spherical wavefunctions. The relation between the incident, scattered, and internal fields determined by the boundary conditions gives us the Mie expansion coefficients. Using the Mie coefficients the extinction, scattering, and absorption efficiency factors can be calculated. Thus, we know the efficiency for the radiation pressure—the proportion of the total incident momentum that is transferred to the particle—and therefore the trapping force.

To trap a sphere a, *tightly focused laser beam* typically with a Gaussian profile is used. This complicates the calculation due to the theoretical difficulty to describe the focused Gaussian beam. Several solutions exist [25, 27, 32–36]. However, many of them extended the Rayleigh [34, 35] or the geometric regime [25] to obtain the trapping force. A possible solution is the generalized Lorenz-Mie theory, which is computationally demanding.

2.2.2. Optical tweezers toolbox

The Optical Tweezers Computational Toolbox was developed by Nieminen *et al.* [37] and is implemented in Matlab. The toolbox uses a point matching method for a multipole

expansion of the strongly focused laser beam [38] and the T-matrix method [39] to calculate the forces and torques on a particle. All important parameters (refractive indices of the solution and the sphere, sphere diameter d , wavelength λ , polarization and profile of the trapping laser, numerical aperture (NA) of the focusing objective, overfilling of the objective) can be varied. Spherical aberrations when using an oil immersion objective are not treated.

T-Matrix method The T-Matrix method for light-scattering calculations is based on the expansion of the incident and scattered fields. The method can be used for scalar waves or vector waves in a variety of geometries. The T-matrix approach was initially introduced by Waterman in 1971 [40] and has been shown to be an efficient method for scattering calculations involving rotational-symmetric particles.

The essence of this method is a relationship between the incident and scattered field of a single particle. The incoming and outgoing fields can be expanded in terms of vector spherical wavefunctions. Due to the linearity of Maxwell's equations and the boundary conditions, the relationship between the scattered and incident coefficients must be linear and is given by the so-called transition matrix (or T-matrix). If the T-matrix is known, the scattered field can be calculated. The T-matrix depends only on the physical and geometric characteristics of the scattering particle (the refractive index, size, shape, and orientation with respect to the incident light beam) and is completely independent of the position of the particle and of the propagation direction and polarization states of the incident and scattered fields. This means that for any particle, the T-matrix only needs to be calculated once, and can then be used for repeated calculation. This is a significant advantage over many other methods of calculating scattering cross sections [41, 42].

In principle, any method to calculate the scattering by the particle can be used to determine the T-matrix. However, the method of choice in the Optical Tweezers Toolbox is the extended boundary condition method. In this method, the internal field within the object is expanded in terms of vector spherical wavefunctions. One problem of the extended boundary condition method is the numerical stability. The field expansions and the T-matrix have to be truncated at some point. Therefore, the extended boundary condition method is inapplicable for extremely non-spherical particles. If the scattering particle has no symmetries, which can be used to optimize the computation of the T-matrix, numerical difficulties may occur [29, 31, 39]. For a spherical symmetric scatterer, the T-matrix must be diagonal and can be solved analytically.

Multipole expansion of strongly focused laser beams A multipole expansion of the incident field is essential for theoretical light scattering methods such as the T-matrix method. Unfortunately, laser beams present some serious theoretical problems. The standard paraxial forms of the beam are not solutions of the vector Helmholtz equation. Therefore, some method must be used to approximate the standard laser beam with a radiation field. The point matching method is an efficient method to obtain multipole expansion equivalents of focused scalar paraxial beams. The incident, internal, and scattered fields are matched at points on the particle surface, using the boundary condition of continuity of the tangential components of the electric and magnetic fields. At these points, the expansion coefficients can be found. The point matching method

can be readily implemented within the T-matrix method, because both methods use vector spherical wavefunctions to expand the fields [38].

Theory for core-shell particles We extended the toolbox to calculate the trapping parameters for coated microspheres. To this end, we had to change the T-matrix elements [43]. Since the T-matrix elements are identical with the Mie coefficients, we had to calculate the scattering of a plane by a coated sphere. The expansion of the field inside the shell yields two new coefficients, which are determined by the boundary condition of the interfaces. The scattering coefficients for the coated sphere can be calculated analytically and are given by Bohren and Huffman [29].

2.3. Optical tweezers setups

Optical tweezers with high position and force sensitivity were not commercially available until recently. Last year, JPK (Berlin, Germany) sold the first generation of high-resolution optical tweezers (Nanotracker), which are capable to study single molecules. Nevertheless, the commercial setups still have limits in resolution and stability. Thus, optical tweezers are typically home-built setups including self-written software for controlling. Depending on the application every optical tweezers setup is an art of its own. A basic optical tweezers setup is composed of a high power trapping laser, a high numerical aperture objective, steering optics to move the trap and/or piezo stages to move the sample, a camera or an eyepiece to observe the trapped specimen, a position detector, and devices to control the setup.

For the work presented in this thesis, I used different home-built optical tweezers setup. The setup in the Howard group (Max Planck Institute for Cell Biology and Genetics, MPI-CBG, Dresden) was used for the kinesin measurements (Part II). The ultra-stable setup in our group, called 'Aswad' (Arabic word for black) was used for the characterization of the titania core-shell particles (Chapter 4) and the measurement of the colored noise of the Brownian motion (Chapter 5). Furthermore, I started to build a new setup, called 'Pinky'. The measurements of the complete force field of an optical trap were performed at a dual-optical trap in the Grill group (MPI-CBG, Dresden) by Marcus Jahnel and Martin Behrndt (see Chapter 3). This setup will be described briefly in Section 3.2.

2.3.1. MPI-CBG setup

The optical tweezers setup in the Howard lab was built around an *inverted microscope* (Zeiss Axiovert 135 TV) on an air damped optical table. A schematic drawing with all elements and the light path is illustrated in Fig. 2.2 [18]. The whole setup was controlled via custom-written software using LabView (National Instruments, USA).

The setup employed a diode-pumped neodymium yttrium orthovanadate crystal (Nd:YVO_4) *laser* with 1.5 W power at a wavelength of 1064 nm (Smart Laser System GmbH, Berlin, Germany). This laser was characterized by a beam quality factor M^2 of 1.2 and a linear polarization normal to the optical table, which corresponded to the y-direction in the image plane. To obtain high-resolution measurements, the stability of the trapping laser with regard to intensity and pointing angle had to be improved. Therefore, the pumping

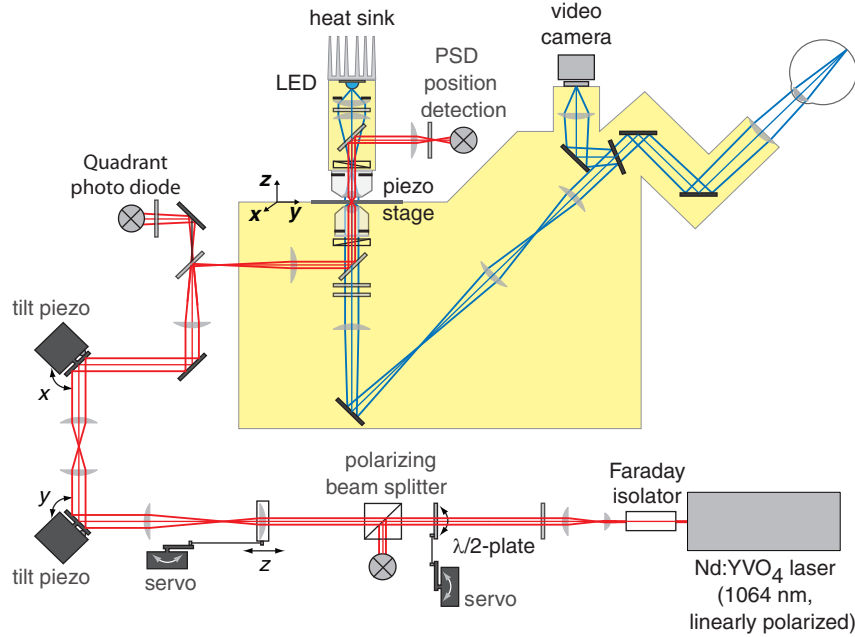


Figure 2.2.: Schematic drawing of the MPI-CBG optical tweezers setup. Shown are all optical components, the inverted microscope (■), the laser path for trapping (—), and the image path (—).

laser was passively cooled and directly mounted onto the optical table. Furthermore, I used the laser power feedback of the setup. Using the power signal, measured by a quadrant photo diode (QPD) at the epi-fluorescence port of the microscope, the pumping laser current was modulated to keep the laser power constant.

The laser beam was steered laterally in the image plane by two *piezo-steering mirrors* (S-226.00, Physik Instruments, Karlsruhe). To get a constant trap stiffness while steering, the mirrors were placed in conjugate planes of the back aperture of the objective [44]. In addition, to move the laser in the axial direction relative to the image plane, a telescope with a moveable lens was implemented. The position of the lens was chosen such that the laser power did not change while moving the lens with a servo [44].

Furthermore, the sample holder was mounted on small x-y-translation stage (07 TMC 511, Melle Griot), which was again mounted on a three-axis *piezo-electric translation stage* (xyz: P-733.3DD, Physik Instrument). This enabled us to move the sample relative to the laser in three-dimension with nanometer precision.

The laser was expanded through two *beam expanders* with a total magnification of 10 to a final beam diameter of ≈ 6 mm. All lenses were anti-reflection coated achromats (LINOS Photonics, Göttingen). An anodized aluminum box enclosed all optics, which were mounted on four rods (Microbench system, LINOS Photonics) clamped to the optical table.

The laser intensity was controlled by a *half wave plate* ($\lambda/2$, zero order 02WRC027/1064, Melles Griot, Bensheim, Germany) placed in front of the polarizer (Linios, Germany). By rotating the plate with a toy model servo, the laser intensity could be varied.

To prevent unwanted light reflection into the laser crystal that may destabilize the laser or lead to mode jumping, we used a *Faraday isolator* (IO-3-1064-VHP, Optics for Research, Caldwell, USA), which transmits light only in one direction.

The three-dimensional position of the microsphere was detected in the back focal plane, using a *position sensing device* (PSD, DL100-7PCBA, Pacific Silicon Sensors Inc., USA). The signals were recorded with a 24-bit data acquisition card (NI-4472, National Instruments). The card had a 45 kHz alias-free bandwidth achieved by the delta-sigma filtering technique and analog filters on the card. As *trapping objective* we used a Zeiss Plan-Neofluar 100, 1.3 numerical aperture (NA), oil-immersion objective.

For visualisation the sample, we used a *custom-built condenser* rested on three fine-adjustment screws on top of the static part of the microscope stage. Advantage of this construction was the enhanced stability against mechanical vibration. Embedded in the condenser was a Zeiss Plan-Apochromat 63x, 1.2 NA, water-immersion objective and a dichroic mirror. The mirror reflected the laser light onto the PSD for back-focal-plane detection in three dimensions [21]. The light emitting diode (blue, Luxeon V star emitter with 3 W) mounted on the top of the condenser enabled video-enhanced differential interference contrast with a standard video camera (LCL-902HS Watec, Japan). We used a light emitting diode because it emitted much less heat and therefore reduced drift [45].

2.3.2. 'Aswad'

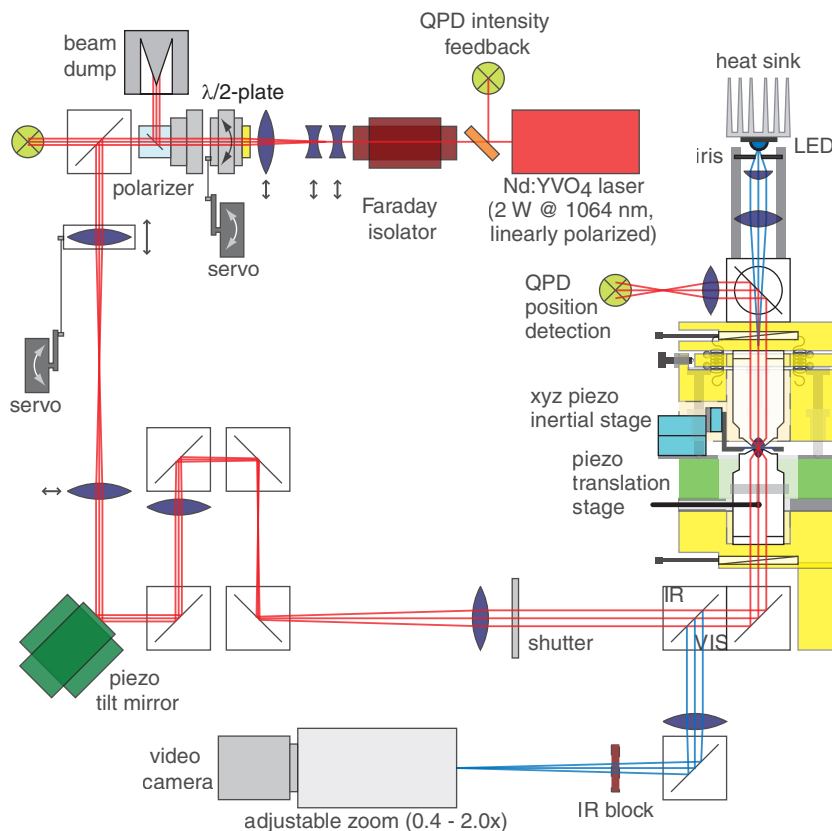


Figure 2.3.: Schematic drawing of the BIOTEC optical tweezers setup 'Aswad'. Shown are all optical components, the home-built microscope (■), the laser path for trapping (—), and the image path (—).

This optical tweezers is the second generation after the Howard lab setup and tuned

for *high stability* and *strong trapping* [46, 47]. A schematic drawing is illustrated in Fig. 2.3.

The inverted microscope was exchanged by a *home-built microscope*. To reduce temperature drift and fluctuations, the setup was built in an isolation box in a separate room and the objectives (infinity corrected CFI S Fluor 100 \times 0.7–1.3 oil objectives, Nikon, Japan) were temperature controlled with millikelvin precision [46]. For minimizing mechanical noise, the optical table was mounted on an actively damped system (Vario Basic 60-300, Accurion GmbH, Göttingen, Germany).

Higher trapping efficiency was achieved with an optimized expansion of the laser relative to the objective [47] and a *high-power laser* with 5 W at a wavelength of 1064 nm (Nd:YVO₄, Smart Laser System GmbH, Berlin, Germany).

The trap was steered laterally in the sample plane by a two-axis *piezo tilt mirror* (Nano-MTA2/2X, MadCity Labs, Madison, USA) positioned in a conjugate plane to the objective back focal plane. In addition, to move the laser in the axial direction relative to the image plane, a telescope with a moveable lens was implemented.

The laser was expanded in two stages (i) using a three-lens *Galilean telescope* and (ii) using a *Kepler telescope*. Using the Galilean telescope the laser was expanded by $3.5\times$ to 2.9 mm diameter beam. The 3-lens Galilean telescope allowed to change the magnification in a smooth, continuous fashion by moving two lenses along the optical axis without the need to replace any of the lenses.

The *laser power* was controlled by a *half wave plate* ($\lambda/2$) placed in front of the polarizer. As in the 'MPI-CBG setup', to reduce back-scattering, a *Faraday isolator* was placed after the laser.

The three-dimensional position of the microsphere was detected in the back focal plane, using a *quadrant photo diode* (QPD, QP154-Q-HVSD, Pacific Silicon Sensors Inc., USA). The IR-optimized silicon based QPD had a cut off frequency of 150 kHz operated in a reverse-bias mode.

Instead of the translation stage for rough positioning of the sample of the 'MPI-CBG setup' a three-dimensional piezo-inertia stage (2x MS30, 1x MS15, Mechonics Ag, München, Germany) was used. This stage was again mounted on a three-axis *piezo-electric translation stage* (xyz: P-733.3DD, Physik Instrument). This allowed us to control the whole setup with a computer from a separate room.

2.3.3. 'Pinky'

The optical tweezers setup 'Pinky' is almost identical to 'Aswad' (Fig. 2.4). I designed the whole setup, in particular the condenser, in a 3D mechanical computer-aided design program (SolidWorks, Fig. 2.5). The main changes concerned the laser steering in the sample plane.

I did not build in piezo-tilt mirrors for lateral steering of the laser. Thus, the laser path became shorter and therefore more stable. Furthermore, the laser alignment became simpler and the setup cheaper.

The moveable lens was replaced by a *deformable membrane mirror* [48]. The deformable mirror (MMDM 10 mm 1 ch defocus corrector, Flexible Optical B.V, Rijswijk, Netherlands) was placed in the back focal plane of the objective. By applying a voltage to the membrane mirror, it changed its curvature. This led to de- or focusing of the beam and an axial movement of the trap in the sample plane.

As a *piezo translation stage*, I used a small and compact nano-positioning system with 50 μm travel range (Nano3D50, Mad City Labs, Madison, United States).

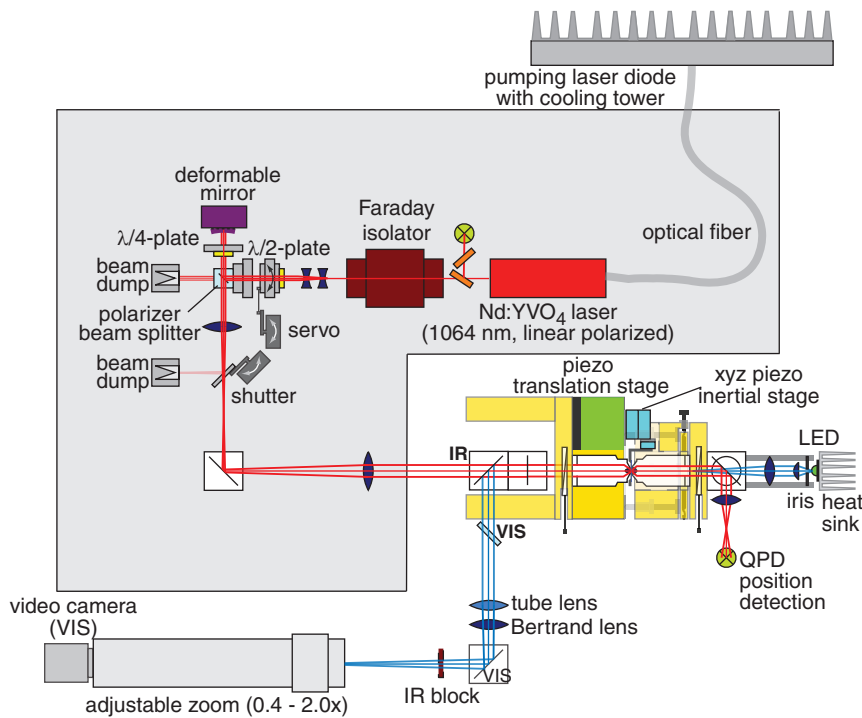


Figure 2.4.: Schematic drawing of the BIOTEC optical tweezers setup 'Pinky'. Shown are all optical components, the home-built microscope (■), the laser path for trapping (—), and the image path (—).

2.3.4. Flow cell

Samples were prepared in a flow cell system (Fig. 2.6). The flow cells were made of two coverslips, a $18 \times 18 \text{ mm}^2$ Menzel coverslip (# 1) on top of a $22 \times 22 \text{ mm}^2$ Corning coverslip (# 1 1/2). The two coverslips were separated by three parallel Parafilm stripes. Finally, the Parafilm was shortly melted on a hot stage to seal the channel walls. This resulted in two channels with a width of $\approx 2 \text{ mm}$, a length of 18 mm, and a height of $\approx 100 \mu\text{m}$ with two open ends. For the experiments, I used easy cleaned or silanized coverslips:

Easy cleaned coverslips To get easy-cleaned coverslips, the coverslips were sonicated in mucasol (1:20) for 15 min, rinsed with demineralized water (ddH₂O), sonicated in pure ethanol for 10 min, and rinsed again in ddH₂O. After repeating these steps, the coverslips were dried in a nitrogen gas stream.

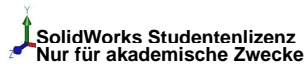
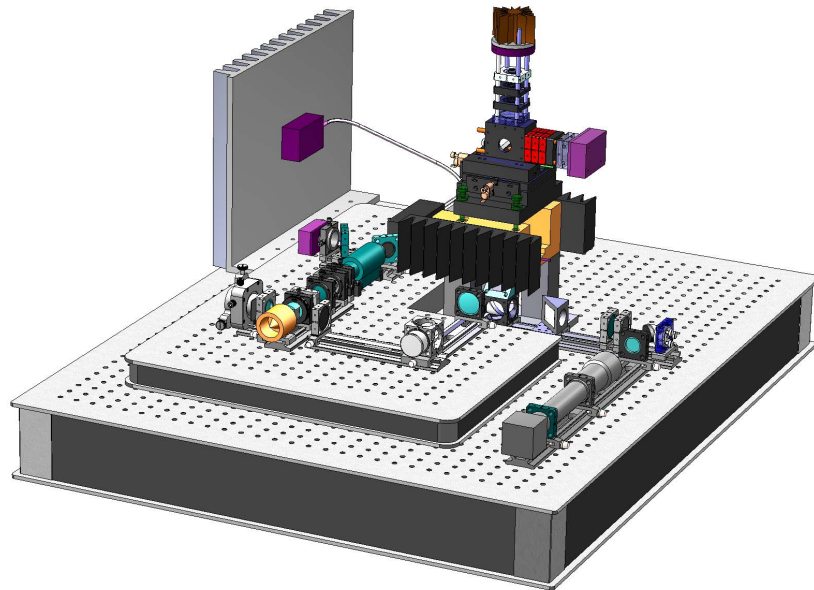


Figure 2.5.: Solid works drawing of the BIOTEC optical tweezers setup 'Pinky'.

Silanized coverslips For silanization, the coverslips were cleaned in different solutions with the following order: 55 min in acetone, 10 min in ethanol, 1 min in nano-pure water, 60 min in Piranha solution (3:5 H₂O₂:H₂SO₄), three 1-min water rinses, 0.1 M KOH, and finally two 1-min water rinses before drying in nitrogen. After washing, the coverslips were silanized in 0.05% dichlorodimethylsilane in trichloroethylene for 1 h. Finally, the coverslips were washed 4 times in methanol while sonicated and after 3 min rinsed further with nano-pure water and stored dry.

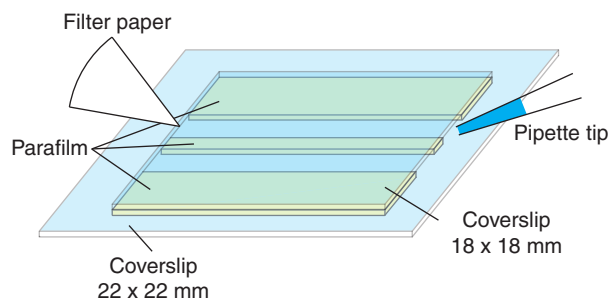


Figure 2.6.: Schematic drawing of a flow cell. The two channels are separated by three parallel Parafilm stripes. The parafilm spacer is $\approx 100 \mu\text{m}$ thick.

2.4. Calibration with positional detection in the back focal plane

The application of an optical tweezers as an accurate position and force sensitive tool depends crucially on the used detection and calibration method. A sensitive detection method is back-focal-plane interferometry [21]. In this method, the alteration of the light field due to a trapped microsphere is monitored in the back-focal-plane of the condenser by a position sensitive detector. From the detector signal the displacement of the microsphere with respect to the trap center and the corresponding forces acting on the microsphere can be determined by calibration. I used a calibration technique developed by Simon F. Nørrelykke and Erik Schäffer *et al.* [18, 49]. The idea of this calibration is shortly described in this chapter.

For a harmonic trap potential, the trapping force of a particle can be described by Hooke's law $F_{trap} = \kappa \cdot \Delta x$, where κ is the trap stiffness and Δx is the relative displacement between the particle position and the equilibrium position near the laser focus. For a known trap stiffness, a known displacement leads to a known force and vice versa; a known force produces a known displacement. Different forces contribute to the total force acting on the particle. One force is the thermal force causing Brownian motion. In addition, the motion is damped by the viscous force $F_{vis} = \gamma \cdot \dot{x}$, where γ is the drag coefficient and \dot{x} denotes the time derivative of the position. Inertial forces can be neglected to first order, however have to be taken into account for accurate results [18, 49]. The resulting dynamics of Brownian motion in a parabolic potential is well characterized by a Lorentzian-type power spectrum [20, 50]. When the power spectral density is fitted with a Lorentzian-type function [49], it returns a plateau value P_0 and a characteristic corner frequency f_c with high precision (Fig. 2.7). From this fits, the trap stiffness $\kappa = 2\pi\gamma f_c$ and the volt-to-meter calibration factor (also called displacement sensitivity β) can be calculated, if the drag coefficient is known. The drag coefficient γ depends on the viscosity η of the surrounding solution, the proximity to a nearby surface, and the radius R of the microsphere [18]. Since this parameters are typically not known exactly, the drag coefficient is not known precisely. Thus, the calibration involves three unknowns: the trap stiffness κ , the displacement sensitivity β , and the drag coefficient γ . Often, two of these values are measured while one is assumed.

To solve this under-determined problem, several calibration methods need to be combined. In our setups, we combined the power spectral analysis with a drag force method, which measures the displacement of the trapped particle in response to a known flow [18, 49]. The piezo stage, holding the flow cell moves sinusoidally relative to the optical trap in the lateral direction with a frequency ν_{stage} and a small amplitude (≈ 500 nm). Due to the harmonically driven stage, a known motion is added to the particle's Brownian motion. In the power spectrum, this motion generates a sharp spike at the oscillation frequency ν_{stage} with a defined peak height (Fig. 2.7). The amplitude of the spike serves as a kind of scale bar for the volt-to-meter factor. Thus, the combination of these two calibration methods enabled us to characterize the system without relying on assumptions.

Due to spherical aberrations, the trap stiffness κ and the displacement sensitivity β depend on the microsphere-surface distance l . Using this method, the trap stiffness κ and the displacement sensitivity β were measured for all spatial directions as a function of microsphere-surface distance l . Additionally, for the driven direction the drag coefficient

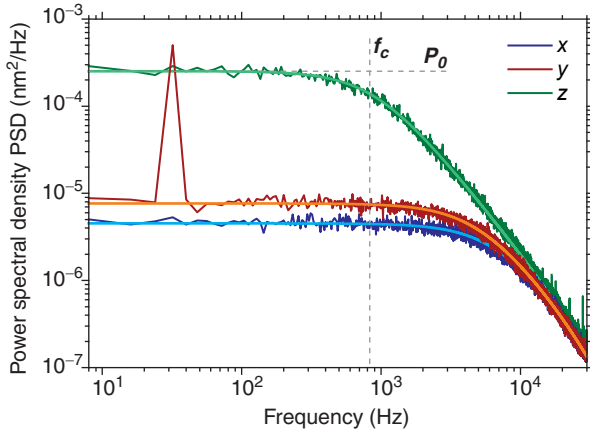


Figure 2.7: *Power spectral density.* Calibrated power spectral density for all spatial directions (x , y , z) of a $0.59\ \mu\text{m}$ diameter PS microsphere. All power spectra were an average over 100 independent measured power spectra. The sampling rate was $65536\ \text{Hz}$, with $8\ \text{Hz}$ resolution. The differences between the lateral directions arise from the laser polarization in the y -direction. The calibration spike at the frequency of $\nu_{\text{stage}} = 32\ \text{Hz}$ in the y -direction results from the sinusoidal stage moving in this direction. Each power spectrum is fitted with a Lorentzian (brighter color). For the axial direction, the corner frequency f_c and the plateau value P_0 are marked.

γ was measured. By fitting the lateral drag coefficient with Faxén's law, the surface position was obtained with nanometer precision. Far away from the surface the measured drag is equivalent to the Stokes drag $\gamma_0 = 3\pi\eta d$ such that $\gamma/\gamma_0 = 1$. Due to an accurate temperature measurement, the viscosity can be calculated and therefore, the microsphere diameter d can be determined.

For the measurements, the raw data were automatically analyzed by a global fitting routine, written in Matlab [18]. The surface position, the drag coefficient, the trap stiffness, and the displacement sensitivity for all directions were calculated for every microsphere.

Chapter 3

Complete force field of an optical trap

The use of optical traps to measure or apply forces on the molecular level requires a precise knowledge of the trapping force field. Close to the trap center, this field is typically approximated as linear in the displacement of the trapped microsphere. However, applications demanding high forces at low laser intensities can probe the light-microsphere interaction beyond the linear regime. Here, we measured and calculated the full nonlinear force and displacement response of an optical trap in two dimensions. We observed a substantial stiffening of the trap beyond the linear regime that depended on the microsphere size. Surprisingly, we found that the linear detection range for forces exceeded the one for displacements by far. Our approach allows a complete calibration of an optical trap.

3.1. Introduction

The assumption of a harmonic optical trapping potential with constant trap stiffness apply only near the trap center. The harmonic potential model breaks down at larger displacements. In the non-harmonic region, the trap stiffness and the displacement sensitivity are not constant anymore. Exact mapping of the complete optical force field enables the use of the full force range of an optical trap. So higher force can be measured by the same laser intensity. In this manner, photo damage in biophysical experiments can be reduced.

In Section 3.2, a procedure to characterize the interaction between a trapped microsphere and the trapping laser for the complete trapping region is reported. The measurements were performed by Marcus Jahnel and Martin Behrndt (Grill group, Max Planck Institute of Molecular Cell Biology and Genetics). In Section 3.3, I compared the experimental results with Mie-theory calculation. The work presented in this chapter has been published in Optics Letter in 2011 [51].

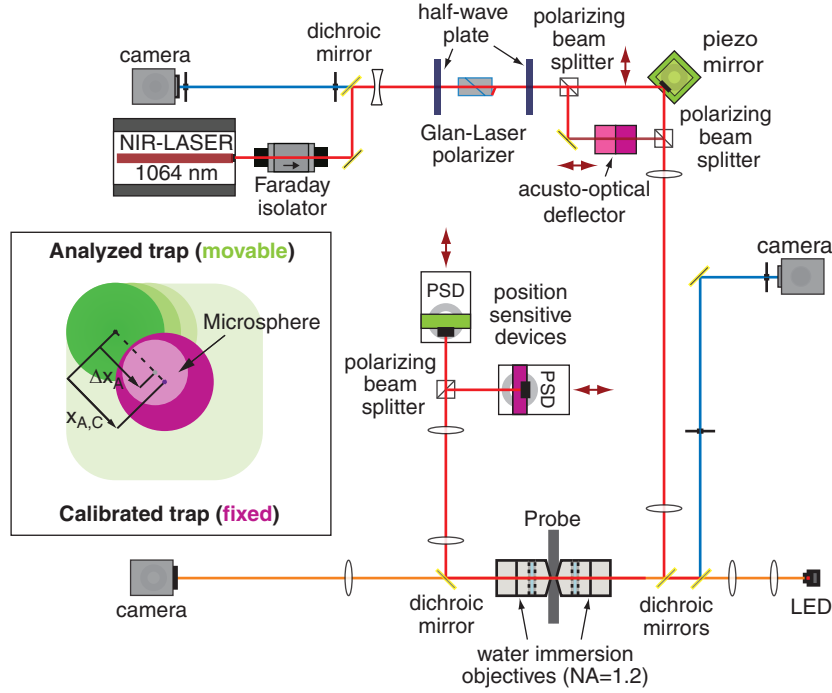


Figure 3.1.: *Dual-optical trap setup.* Laser path (—), back reflection path (—), imaging path (—), polarization state (dark red arrows). Shown are all optical components: Faraday isolator, dichroic mirrors, half-wave plate, Glan-Laser polarizer, polarizing beam splitter, acousto-optical deflector, piezo mirror, water immersion objectives (NA= 1.2), position sensitive devices (PSD), charge-coupled device. Inset: *Schematic of the experiment.* The **strong calibration trap** was stationary, while the **weaker analyzing trap** was scanned across the microsphere. The trap distance is defined by $x_{C,A}$; Δx_A is the microsphere displacement from the center of the analyzing trap.

3.2. Measurement of the complete force field of an optical trap

The measurement of the force field landscape was done with a *single-beam dual-trap* optical tweezers (Fig. 3.1). The two optical traps were separated by polarization and individually maneuverable with variable intensities. To reduce polarization crosstalk between the two traps to below 1%, each element was aligned via both transmission and backreflected light [52]. One trap, the *strong calibration trap*, was fixed, while the weaker, *analyzing trap*, scanned the whole microsphere-trap interaction regime. The forces exerted by the two optical traps acting on the microsphere at the position Δx_A are in general described by the Langevin equation

$$m\Delta\ddot{x}_A(t) + \gamma\Delta\dot{x}_A(t) + \mathbf{F}_C(\Delta x_A, t) + \mathbf{F}_A(\Delta x_A, t) = \mathbf{F}_{\text{thermal}}(t(t)) , \quad (3.1)$$

where m the mass of the microsphere, γ the bulk friction coefficient, $\mathbf{F}_{C/A}(\Delta x_A, t)$ the optical forces of the two traps respectively, and $\mathbf{F}_{\text{thermal}}(t)$ the random thermal forces. For stationary traps and measurement times long enough to average over thermal fluctuations Eq. 3.1, can be simplified to $\langle \mathbf{F}_C(\Delta x_A) \rangle_{t_{av}} = -\langle \mathbf{F}_A(\Delta x_A) \rangle_{t_{av}}$. Instead of using a low-power observation laser to detect the position of the microsphere (e.g. as described in Neumann *et al.* [13]), Jahnel *et al.* used a strong calibration trap, at least 10 times stronger than the weak analyzing trap. This assured that the trapped microsphere

never left the linear regime of the strong calibration trap. In this manner, the force \mathbf{F}_A can be determined by

$$\hat{\kappa}_C \langle (\Delta x_A - x_{C,A}) \rangle_{t_{av}} = \langle \mathbf{F}_A(\Delta x_A) \rangle_{t_{av}}. \quad (3.2)$$

where $\hat{\kappa}_C$ is the diagonal trap stiffness tensor of the calibration trap obtained via thermal calibration [50] and $x_{C,A}$ the distance vector between both traps. Thus, staying in the linear regime of one strong trap allows to measure the optical forces for arbitrary displacement of a microsphere with respect to a second weaker optical trap.

In a typical experiment, the weak, analyzing trap ($\kappa_A \lesssim 60 \text{ pN}/\mu\text{m}$) was laterally scanned in a 2D grid with a 5 nm step size. With the calibration trap ($\kappa_C \lesssim 2500 \text{ pN}/\mu\text{m}$) fixed, this scan covered the entire interaction region ($x_{C,A} > d/2$) of the analyzing laser light with the trapped microsphere with a diameter d in solution. The microsphere displacement with respect to the stiff calibration trap, was less than 150 nm in the lateral direction and less than 100 nm in the axial direction. This ensured the validity of the Hookean approximation for the calibration trap to within 5%. Measuring times at each grid point (10 ms) were chosen longer than the characteristic equilibration time, f_c^{-1} , resulting in accurate force response curves. Data were recorded with both detectors at 10 kHz and averaged to a bandwidth of 1 kHz for saving. All microsphere sizes were determined to within 5% accuracy using the combined drag-force power spectrum analysis method (see Section 2.4, [49]).

Jahnel *et al.* determined a 2D map of the optical forces exerted by the analyzing trap on polystyrene microsphere with different diameters (Fig. 3.2 c). They obtained the net force by combining the parallel (F_x) and perpendicular (F_y) force components relative to the trap polarization. The optical forces were nearly radially symmetric (Fig. 3.2 d). Therefore, further measurements and discussions were restricted to cross-sections of the force map in x (dashed line in Fig. 3.2 c). Results for the other directions were qualitatively the same.

3.3. Calculation of the complete force field of an optical trap

3.3.1. Mie theory calculations of the force map

For the numerical calculations, I employed the optical tweezers toolbox (see Section 2.2.2) adapted to the dual trap setup (Fig. 3.1). I used the following parameters: The numerical aperture was fixed to 1.1; the laser had a linear polarization along the x -axis; no truncation of the laser at the back aperture and no spherical aberration were taken into account. Furthermore, the microsphere was not displaced axially from the laser focus. The forces acting on a microsphere were calculated as a function of lateral displacements. Absolute force values were determined by scaling to the experimental data.

3.3.2. Comparison between theory and experiments

Figure 3.2 a shows the two-dimensional map of the optical forces exerted on a polystyrene microsphere of diameter $1.26 \mu\text{m}$. The net force $|\mathbf{F}| = \sqrt{F_x^2 + F_y^2}$ is almost radially symmetric (Fig. 3.2 b). Figure 3.2 c, d shows the measured force response along the

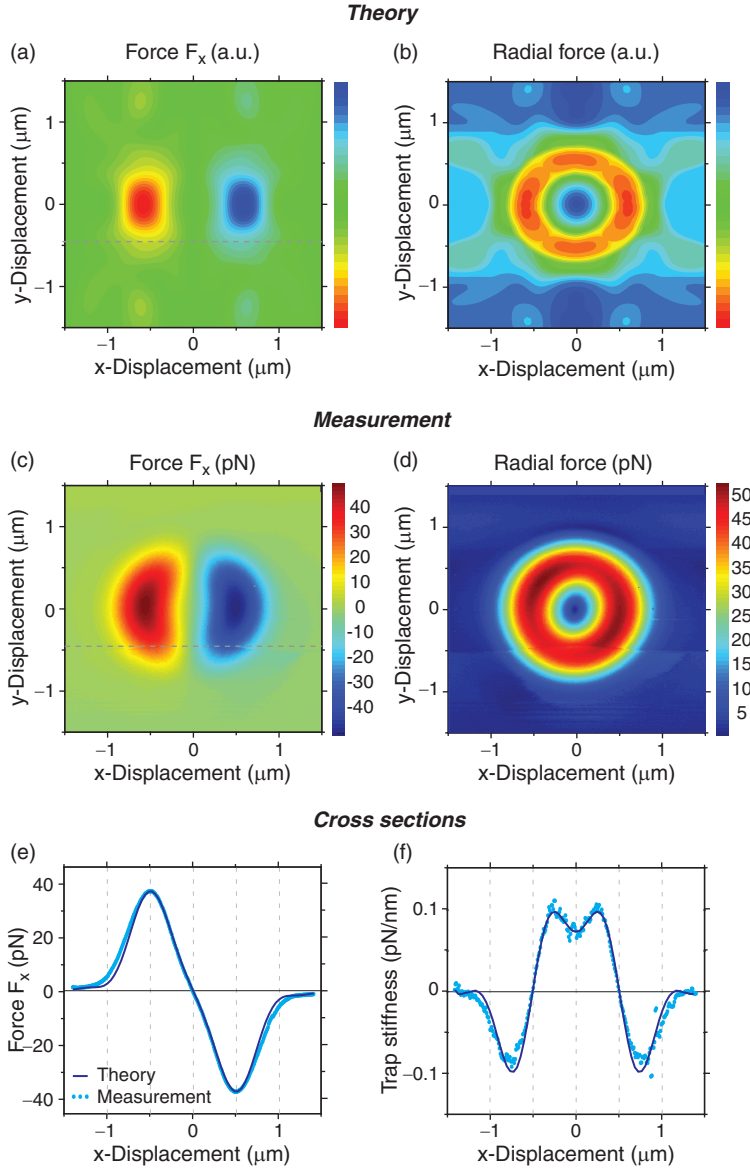


Figure 3.2: *Force map.* Theoretical (a,b) and experimental (c,d) two-dimensional maps of optical forces on a $1.26\ \mu\text{m}$ microsphere in the direction of polarization (a,c) and of the magnitude of the radial force (b,d). Force magnitudes are color-coded by corresponding heat maps. (e) Complete force response and (f) trap stiffness along the polarization axis for experimental data (\cdots) and theory ($-$).

polarization axis and the net force. Data and theory were in excellent agreement. Compared to the theoretical force profile, the experimental one was slightly broader beyond the extrema (Fig. 3.2e). We attributed this difference to diffraction effects at the back aperture of the trapping objective, which were not taken into account by the optical tweezers toolbox.

Close to the origin, a constant trap stiffness—assuming Hooke’s law—was expected. However, numerical differentiation of the measured force curve ($\kappa(x) = -\partial_x F(\Delta x_A)$) proved that the trap stiffness continuously deviated from its value at the origin (Fig. 3.2e). Displacing the microsphere from the center, the trap stiffness increased moderately within the first 300 nm towards a maximum, before it fell off, and eventually became negative. In this region, the analogy between optical traps and mechanical springs fails; the trap stiffness is negative for a decreasing, yet, still restoring force. The stiffening effect was substantial even for small displacements. A displacement from the trap center of 250 nm already lead to a deviation of the trap stiffness of more than 30 % as compared with its value at the origin.

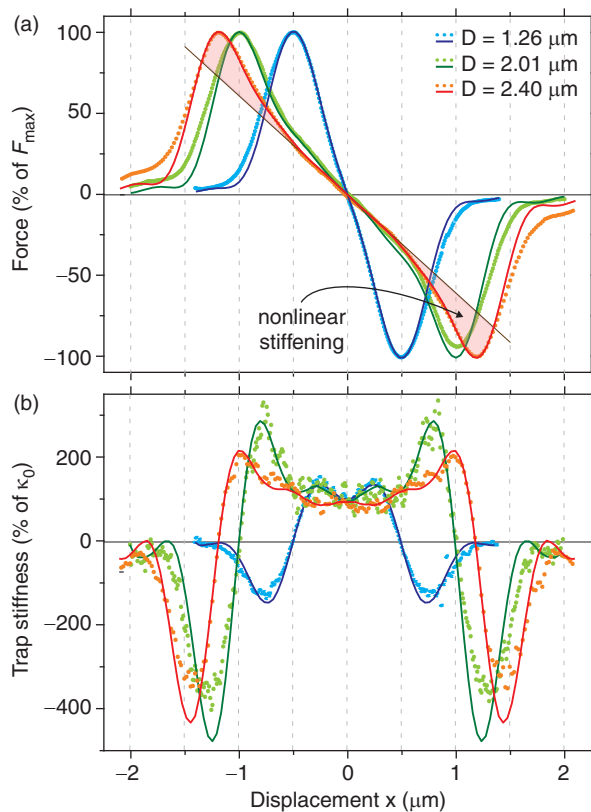


Figure 3.3: Force profile and trap stiffness. (a) Normalized force-extension curve and (b) normalized trap stiffness for three different polystyrene microspheres (1.26 μm \cdots —; 2.01 μm \cdots —; 2.4 μm \cdots —). The lines correspond to the theory, whereas the points mark the measurements.

A distinct second linear regime of higher constant trap stiffness was recently reported for 2.01 μm microspheres [53]. To study the microsphere size dependence of the observed stiffening effect in more detail, we compared the 1.26 μm microspheres with larger ones of diameters 2.01 μm and 2.40 μm in Fig. 3.3 a, b. Indeed, the stiffening was more pronounced for larger microspheres and depended sensitively on their exact size. Figure 3.3 b shows that the measured stiffness landscapes were complex, displaying ripples, yet no extended linear regime.

Next, we used the assay to evaluate the accuracy of the back-focal-plane detection method [54]. This method infers both the displacement and force from a single differential voltage signal on a position-sensitive device. For small displacements, both measures were well approximated as linear functions of the differential voltage signal. For larger displacements, we found that the linear force-displacement relation broke down (Figs. 3.2 e and 3.4 a). As depicted in Fig. 3.4a, b for microspheres of diameter 2.01 μm assuming a linear relationship between force and voltage signal was correct to within $\pm 5\%$, even for very large displacements close to the force maximum. On the other hand, inferring microsphere position from the same voltage signal—again assuming linearity—lead to significantly larger errors of up to 40% (Fig. 3.4 b).

3.4. Discussion

Without any preliminary assumptions, we measured and calculated the complete 2D force field of an optical trap. The calibration by Jahnke *et al.* described in Section 3.2 provided a robust method for the study of the complete light-microsphere-interactions,

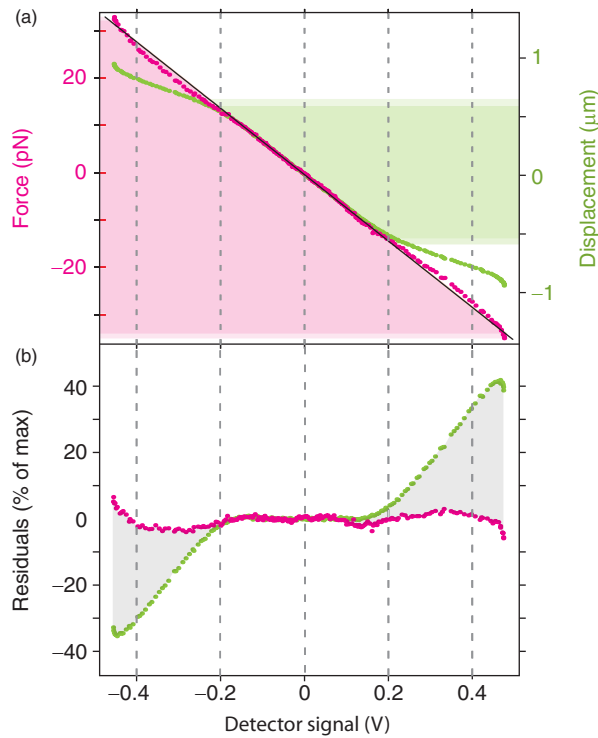


Figure 3.4: Force - detector signal relation. (a) Force (left axis, \cdots) and displacement (right axis, \cdots) as a function of the detector signal for $2.01\ \mu\text{m}$ microsphere. Shaded areas indicate where residuals of linear fit were less than 5% (dark) or less than 10% (bright). (b) Force (\cdots) and displacement (\cdots) residuals of the fit in (a).

including accurate measurements beyond the linear regime. Importantly, the measurements were well described by the Mie theory calculations. These allowed us a detailed validation of the linear force-displacement approximation. The treatment of optical tweezers as springs is an approximation, valid only close to the trap center, and its validity depends sensitively on the size of the trapped object. Furthermore, we found that an optical trap with back-focal-plane detection is foremost a sensor of force and not of position. Positional information was inferred from a linear approximation, which does not hold far away from the trap center and for large microsphere displacements.

Chapter 4

Nanonewton optical forces by trapping anti-reflection-coated titania microspheres

The applicability of optical tweezers is limited by the maximum force that can be generated. While improvement of the technique has largely focussed on improving the instrument and shaping the light beam [55, 56], little work has been done on shaping the trapped object [57]. Here, I designed efficient, photonically-structured probes: Anti-reflection-coated, high-refractive-index, core-shell particles composed of titania. With these probes, I significantly increased the maximum optical force beyond a nanonewton. The increased force range broadens the scope of feasible optical trapping experiments. Photonically structuring arbitrarily-shaped objects will pave the way for efficient light-driven miniature machines.

4.1. Maximum force of optical tweezers limits their applicability

The force range of optical tweezers limits the applicability of the technique. For example, forces are often not sufficient to unfold proteins [58]. Usually, trapping forces range from sub-piconewton to about 100 pN (e.g. [58–62]). The maximum force is limited by the available laser power and the trap efficiency. An increase in laser power, however, leads to heating [63] and, in case of biological applications, to photo damage. The trapping efficiency can be improved, for example, by using a Laguerre-Gaussian laser mode [64], exploiting near-field effects [65], compensating spherical aberrations [66], choosing the optimal laser expansion [47], or choosing a probe size close to the first Mie resonance [47, 67]. While these measures mostly aim at improving the instrument, all of them are limited by the material properties and structure of the photonic probe.

The photonic properties of the probes can be optimized to increase the trap efficiency. To this end, an increase in the refractive index mismatch between the trapped particle and its surrounding medium, increases the stabilizing gradient forces and thereby the

efficiency. However, there is an upper limit to this mismatch since the destabilizing scattering force increases stronger with the mismatch than the gradient force [67]. Thus, high-refractive index particles ($n > 1.73$ immersed in water [68]) *cannot* be trapped by a *single* gradient trap [69] unless, as predicted by theory, they are photonically structured to reduce the scattering force—in the simplest case, coated with an anti-reflection layer [67, 68]. In previous work [67], silica-coated polystyrene microspheres moderately improved trapping and reduced back-scattered light. For these low-refractive index materials, a coating was not an essential requirement for being able to trap..

Here we took the decisive and difficult step of coating high-refractive index particles to make so far untrappable probes trappable. We fabricated coated titania particles according to the specifications of Mie theory calculations and characterized them in an optical trap in terms of their trap stiffness per laser power and escape force. I found a significantly higher trap efficiency, in agreement with the calculations, compared to all other probes in use. By this measurements, I extended the applicability of optical tweezers with respect to two aspects: first, by reducing photo damage in biophysical experiments since the same force can be achieved with much less laser power and, second, by bringing the force range of optical tweezers in the nanonewton range, which I demonstrate by using an optimized optical tweezers setup at maximum laser power. The trapping properties of our photonically-structured, anti-reflection-coated titania particles are superior to homogeneous ones opening up new possibilities for light-driven probes and optical tweezers experiments.

The work presented in this chapter has been published in Nature Photonics.

4.2. Methods

4.2.1. Anti-reflection coating

In an optical trap micron-sized dielectric particles can be trapped by a tightly focused laser beam. The optical force on the particle is composed of an attractive gradient force and a destabilizing scattering force (see Section 2.2). I optimized the photonic properties of the probe by using an anti-reflection coating to reduce the scattering forces. The anti-reflection coating is based on destructive interference between the two reflected waves from the core and the coating layer. The principle of an anti-reflection is best understood for a planar coating [70]. To achieve destructive interference, a coating has to fulfill two conditions: First, the amplitude of the two reflected waves has to be equal (*amplitude condition*). This is the case when the coating n_{coat} has a refractive index corresponding to the geometric mean of the two surrounding media ($n_{\text{core}}, n_{\text{H}_2\text{O}}$):

$$n_{\text{coat}} = \sqrt{n_{\text{core}}n_{\text{H}_2\text{O}}} \quad (4.1)$$

The second condition—the *phase condition*—determines the thickness of the coating. The path difference of the two waves has to be half a wavelength in the coating. Therefore, I obtain a thickness of

$$d_{\text{coat}} = \frac{\lambda}{4n_{\text{coat}}} \quad (4.2)$$

where λ is the wavelength in air. Under these conditions, the reflected waves extinguish each other and the reflection coefficient is equal to zero [71].

The above arguments are true for normal incidence (plane wave and a plane surface). In case of a focused beam and a sphere, I have to consider the angles of the incoming light. Furthermore, the dimension of the particle is in the dimension of the laser wavelength. Thus, neither the ray optics nor the point-dipole approach in the Rayleigh regime are valid. Therefore, I used the Lorenz-Mie theory for calculations (see Section 2.2).

4.2.2. Parameters for calculations

We used two methods to calculate the trap efficiency in terms of the trap stiffness per power. Both calculations were based on scattering of light by small particles as described either by the T-matrix method (see Section 2.2) or by the generalized Lorenz-Mie theory [69]. For both calculations, we used the following parameters: refractive indices of $n_{\text{core}} = 2.3$, $n_{\text{coat}} = 1.78$, and $n_{\text{H}_2\text{O}} = 1.326$ at a laser wavelength of $\lambda = 1064\text{ nm}$. A thin silica layer for one batch of particles (Table 4.1, Section 4.4) was neglected in the calculations. The first calculation was based on an extended version of the optical tweezers toolbox (see Section 2.2.2). For the toolbox, I used an effective numerical aperture of 1.25, an overfilling described by a truncation angle (80°), and a polarization in the y -direction. The second calculation was done by Peter D. J. van Oostrum and included the effect of spherical aberrations produced by refraction at the interface between the glass of the sample cell and the water in which the particles are immersed. For this calculation, the geometric focus of the trap was $5\ \mu\text{m}$ away from the glass surface. The numerical aperture of the objective was 1.22 and the ratio between the focal lengths and the beam waist was 0.903. With these parameters, both methods gave consistent results at the surface where spherical aberrations are minimal.

4.2.3. Optical tweezers setup

The measurements were performed with the optical tweezers setup 'Aswad' (see Section 2.3.2). I used 4.5 W laser output power. For the trap stiffness measurements, the overfilling of the objective [47] was 1.5 with a maximum power of 1.4 W in the focus. For the drag force measurements, which were done in water-immersion oil, I used an overfilling of 2 with a maximum power of 1.1 W in the focus. The larger filling ratio enabled to trap microspheres in oil more easily.

4.2.4. Sample preparation & calibration

I prepared samples as described in Section 2.3.4. All microspheres were washed in distilled water (aqua bidestillata: $18.2\ \text{M}\Omega\text{cm}$). All measurements were done in distilled water close to the glass surface ($l \approx 2\ \mu\text{m}$ microsphere-center surface distance). For each microsphere type, I acquired data for at least 6 microspheres. Using the calibration (see Section 2.4), I measured the distance to the surface l , the drag coefficient γ and associated diameter of the microsphere d , the displacement sensitivity β , and the trap stiffness κ for all spatial directions. Calibration measurements were performed at $\approx 5\%$ laser power (0.23 W output power). Control measurements confirmed the linearity between trap stiffness and laser power P (Fig. 4.7b). For comparison, I used

0.6–1.5 μm -diameter polystyrene microspheres ($n_{\text{PS}} = 1.57$, Bangs Laboratories, USA). For the escape force measurements, I used 100% laser power (4.5 W output power). The particles were dried at room temperature for 60 min and then re-suspended in water immersion oil ($n = 1.33$; Immersol W, Zeiss) with a dynamic viscosity of 1.08 Pas at 20 °C (0.32 Pas at 40 °C). To achieve a nearly linear increase in drag force with time, the piezo translation stage holding the sample was accelerated with 40 mm/s² relative to the stationary laser.

I estimated the amount of laser-induced heating when trapping in immersion oil according to the following calculation: With the in-oil-measured drag coefficient, I calculated an oil viscosity of 0.42 ± 0.03 Pas using the average microsphere diameter (batch \blacktriangleright , Table 4.1), also accounting for the distance to the surface l . Based on a linear interpolation between manufacturer-given values, this viscosity corresponded to a temperature of 37 ± 1 °C an increase of 9 °C relative to the temperature of the objective.

4.3. Theory predicts nanonewton optical forces with anti-reflection coated titania microspheres

To design an optimal anti-reflection coated titania microsphere, I used T-matrix and Mie theory calculations (Fig. 4.1). I optimized the core and shell size and the shell refractive index to achieve the highest trapping efficiency for a laser wavelength of $\lambda = 1064$ nm. In the calculations, I fixed the refractive index of the core to $n_{\text{core}} = 2.3$, which corresponds to the measured value of anatase titania [72], and varied the shell refractive index n_{coat} . Surprisingly, even for Mie scatterers, the optimal shell refractive index of 1.78 was very close to the geometric mean 1.75 of the indices from the core and the medium. This geometric mean is expected for an optimal, single-layer anti-reflection coating on flat, macroscopic substrates as described in Section 4.2.1 [73]. For $n_{\text{coat}} = 1.78$ (measured value for amorphous titania was ≈ 1.7 –1.8, see Section 4.4), I calculated the trap stiffness as a function of core d_{core} and core-shell diameter d (Fig. 4.1). In the absence of spherical aberrations, the *highest* lateral trap stiffness resulted for a core size of $d_{\text{core}} = 0.5 \pm 0.05$ μm with a coating thickness of $d_{\text{coat}} = 0.23 \pm 0.04$ μm (intense magenta region in Fig. 4.1 a). The latter value is significantly larger than $\lambda/(4n_{\text{coat}}) = 0.15$ μm —the thickness expected for planar coatings. Thus, calculations were necessary to determine optimal parameters. Particles with a thinner or thicker shell than the optimal one cannot be trapped according to the calculation (white regions in Fig. 4.1). Also, certain particles—in particular smaller ones—cannot be trapped further away from the surface because of spherical aberrations at the glass-water interface (Fig. 4.1 b). Plots for the axial trap stiffness resembled the lateral ones, however, with smaller values for the trap stiffness and slightly shifted sizes for the maxima (Fig. 4.1 c, d). Based on these calculations, we fabricated microspheres designed for “ideal” trapping conditions (no spherical aberrations): either using (i) an oil-immersion objective trapping close to a surface or (ii) a water-immersion objective for trapping far away from a surface. The calculations showed that such optimized probes should have an overall diameter of about 1 μm . However, the specifications were stringent with respect to the refractive indices and in particular the shell thickness.

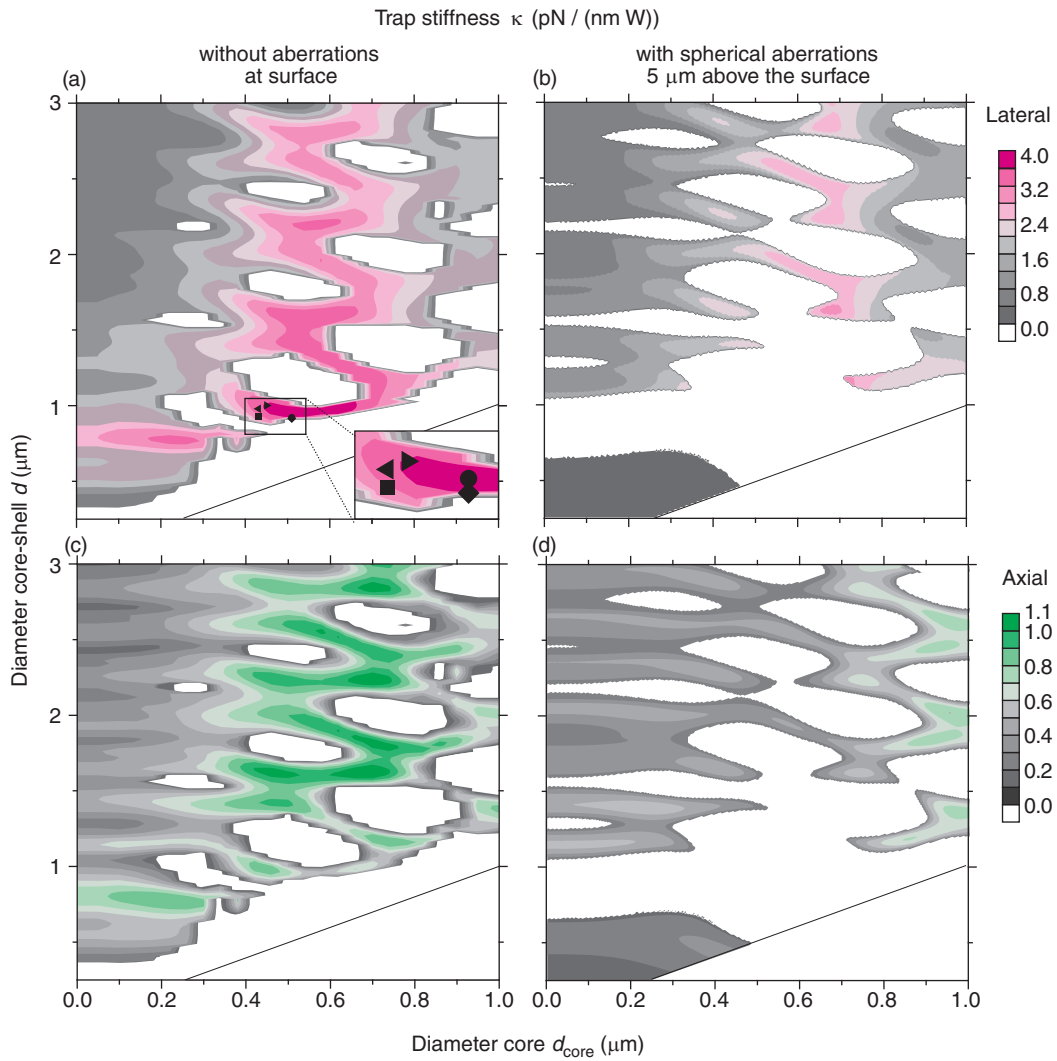


Figure 4.1.: *Mie theory calculations.* Mie theory predictions of lateral (top row) and axial (bottom row) trap stiffness per power in the focus as a function of the core diameter d_{core} and total core-shell diameter d (see Section 4.2.4). White areas correspond to particles that cannot be trapped. The black line demarcates zero-shell thickness. (a,c) T-matrix calculations based on the optical tweezers toolbox. The symbols (see Table 4.1) mark the size of the fabricated titania core-shell particles. (b,d) Calculations including spherical aberrations. The geometric focus of the trap was $5 \mu\text{m}$ away from the glass surface.

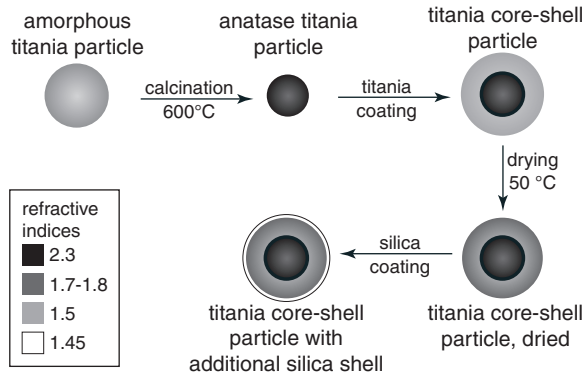


Figure 4.2: *Synthesis of titania core-shell particles.* Amorphous titania particles were calcined and coated with amorphous titania. The refractive index of the shell was increased by an additional drying step. For some particles, we coated a thin silica shell on the surface.

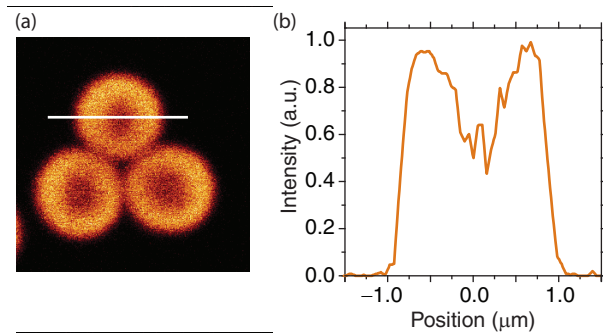


Figure 4.3: *Fluorescence confocal image.* (a) Fluorescence microscopy image of titania core-shell particles after addition of fluorescent dye, where dye can only reach the shell. (b) Intensity profile of the cross section (white line in (a)).

4.4. Synthesis of anti-reflection coated titania microspheres

Due to special catalytic, electric and optical properties, titania is an important material in modern materials science, chemistry, and physics. I was in particular interested in the high-refractive index of titania. We used a novel method to synthesize colloidal particles with a high-refractive index crystalline titania, anatase core and a lower refractive index amorphous titania shell. In the following part, these particles will be called titania core-shell. We improved the synthesis regarding monodispersity and accurate particle size tunability. Both criteria were crucial factors for trapping. A schematic representation of the procedure for fabrication is given in Figure 4.2.

We started with the synthesis of amorphous titania cores according to the procedure of Yu *et al.* with slight modifications [74]. The anatase core particles ($n_{\text{core}} = 2.3$) were obtained after calcination—a heating step yielding fully crystalline titania. In the next step, the anatase particles were coated with amorphous titania ($n_{\text{coat}} = 1.5$) according to the procedure of Eiden-Assmann *et al.* [75]. Afterwards, we dried the particles at 50 °C for 30 min to increase the refractive index of amorphous titania (n_{coat}) to $\approx 1.7\text{--}1.8$. One batch of particles was finally coated with a thin silica shell ($n_{\text{SiO}_x} = 1.45$).

To test whether we got an amorphous coating, we added a fluorescent dye (rhodamine isothiocyanat) to the dispersion of the titania core-shell particles and centrifuged them afterward to remove excess dye. Fluorescence confocal microscopy images showed only a labeling in the outer area (Fig. 4.3). The dye was small enough to diffuse into the amorphous coating, but not into the crystalline anatase core.

The size of the core and the core-shell particles was determined with transmission electron microscopy (TEM). The TEM pictures showed homogeneous core sizes and coatings (Fig. 4.4). We observed that amorphous titania particles shrank by observing them with the electron beam. Due to this heating effect, the size of amorphous titania

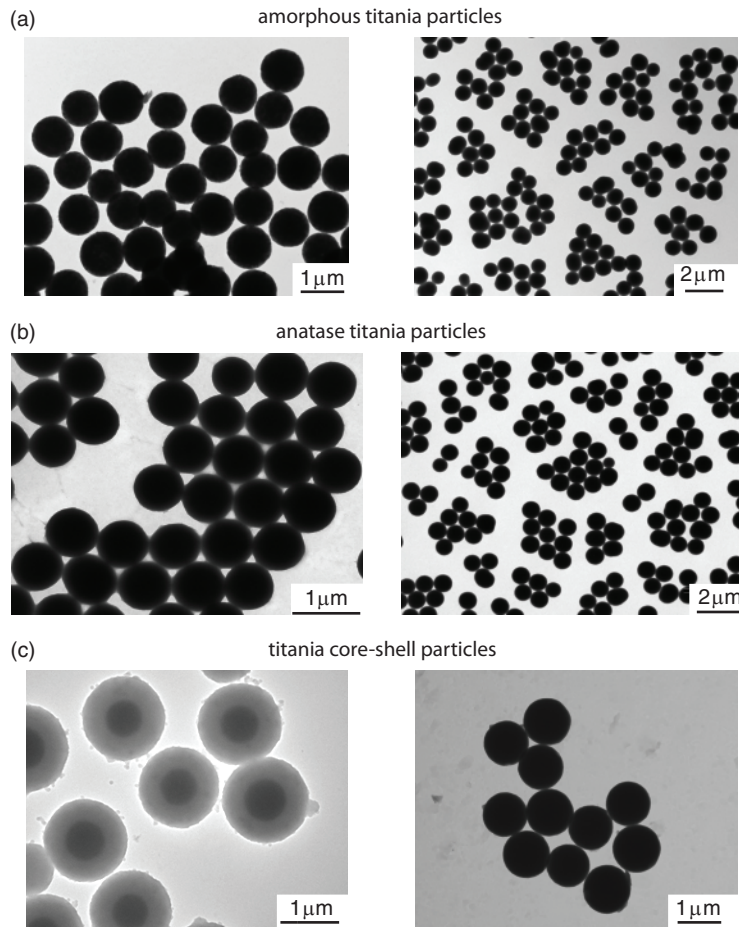


Figure 4.4.: *Transmission electron microscope pictures.* TEM pictures of (a) amorphous titania particles. (b) anatase titania particles and (c) titania core-shell particles.

particles and the titania core-shell particles was slightly underestimated. Therefore, I determined the exact size of the core-shell diameter with our combined drag-force power spectrum analysis method (see Section 2.4, [49]).

Furthermore, we estimated the size, the polydispersity and the refractive index of the titania particles with static light scattering (SLS). SLS is a technique that measures the intensity of scattered light as a function of angle. In Figure 4.5 experimental curves of amorphous, anatase and titania core-shell particles are plotted against the scattering angle. The experimental curves were fitted to theoretical calculations of the full Mie solutions. The locations of the minima and maxima depend sensitively on the particle size and refractive index, whereas the depth of the minima gives an estimate of the polydispersity. The SLS measurements gave good agreements with TEM measurements for the pure amorphous or anatase particles sizes. The estimation of the size of the core-shell particles with SLS was delicate.

The refractive indices were determined with digital holographic microscopy. Light scattered by a particle propagates to the microscope focal plane, where it interferes with the undiffracted fraction of the beam. The resulting interference pattern was magnified by a microscope objective lens onto the sensor of a gray scale video camera. Fitting these digitized holograms to a model that includes the analytic description of light scattering

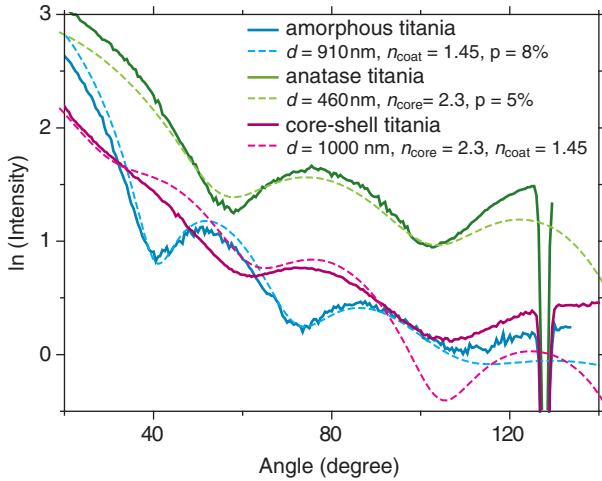


Figure 4.5: Static light scattering measurements. SLS experimental curves of amorphous (—), anatase (—) and core-shell titania particles (—) in ethanol fitted to theoretical calculations of the full Mie solutions (---, ---, ---, respectively). Fit parameters were the particle diameter d , the refractive index n and the polydispersity p .

by Lorenz-Mie yielded the particles three-dimensional position, its diameter d , and its refractive index n (Fig. 4.6) [76].

The density of the anatase-titania core was $\rho_{anatase} = 4200 \text{ kg m}^{-3}$ and the amorphous shell was $\rho_{amorphous} = 1.320 \text{ kg m}^{-3}$. The density of the amorphous titania was determined by the amount of shrinkage during calcination of amorphous titania particles to anatase titania particles ($d_{amorphous} = 418 \text{ nm}$, $d_{anatase} = 312 \text{ nm}$). By calculating the total mass of the core and the shell divided by the total volume, the average titania core-shell density was $\rho_{titania} = 2500 \text{ kg m}^{-3}$.

The synthesis of the titania core-shell particles was done together with Ahmet F. Demirörs in the Soft Condensed Matter group of Alfons van Blaaderen at the Utrecht University in Netherlands. The results were published by Demirörs and Jannasch *et al.* in Langmuir [72].

4.5. High trap stiffness with anti-reflection coated titania microspheres

We synthesised different batches of titania core-shell particles with a core size of around $0.5 \mu\text{m}$ and a final diameter of about $1 \mu\text{m}$ (see Section 4.4). Using a 1.3 NA oil immersion objective, I could stably trap microspheres of only half the batches at over-filling ratio $\gtrsim 1.5$ at distances $l \lesssim 5 \mu\text{m}$ away from the surface. This shows how critical the correct parameters were, in particular with respect to spherical aberrations that are minimal close to the surface. Particles that could be successfully trapped are listed in Table 4.1.

For these microspheres (marked with black symbols in Fig. 4.1 a), I measured the trap stiffness as a function of diameter (magenta open symbols in Fig. 4.7) and compared the values to those of polystyrene microspheres (hexagons in Fig. 4.7). For the titania microspheres, I measured a lateral trap stiffness of up to $3.8 \text{ pN}/(\text{nm W})$ and an axial trap stiffness of up to $0.9 \text{ pN}/(\text{nm W})$. Compared to the maximum lateral (axial) trap stiffness for polystyrene microspheres, this was a two-fold (1.3-fold) improvement. The measurements agreed well with the predictions (black symbols, Fig. 4.7) showing that I achieved the maximum possible trapping efficiency.

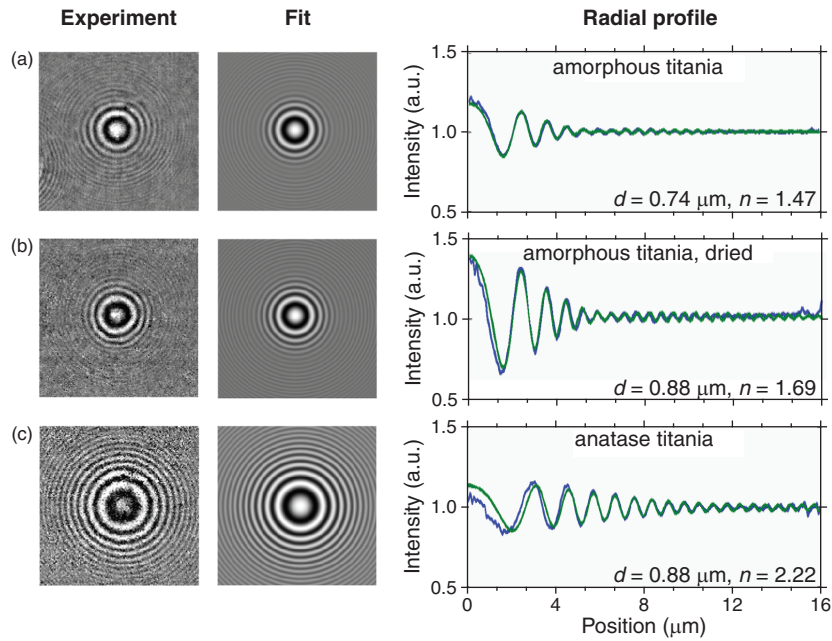


Figure 4.6.: *Digital holographic microscope measurements.* Holographic measurements (Experiment, left column) and simulations (Fit, middle column) of (a) amorphous titania particles, (b) dried amorphous titania particles and (c) anatase titania particles. The right column shows the comparison of experiment (—) and fit (—). Fit parameters were the particle diameter d and the refractive index n .

Table 4.1.: *Size of different titania core-shell particle batches.* Sizes are stated as mean \pm SEM (N, number of measurements) in μm . The core diameter was measured with transmission electron microscope and the core-shell diameter with our optical tweezers calibration. The shell thickness is based on the difference between total and core diameter.

	Core diameter d_{core}	Shell thickness d_{coat}	Shell thickness	Total diameter d
	Anatase titania	Amorphous titania	Silica	
\triangleright	0.45 ± 0.006 (12)	0.28	-	1.00 ± 0.02 (6)
\triangleleft	0.43 ± 0.006 (42)	0.28	-	0.98 ± 0.020 (6)
\square	0.43 ± 0.006 (42)	0.25	-	0.93 ± 0.01 (6)
\diamond	0.51 ± 0.005 (32)	0.20	-	0.91 ± 0.02 (6)
\circ	0.51 ± 0.007 (21)	0.20	0.02	0.95 ± 0.01 (6)

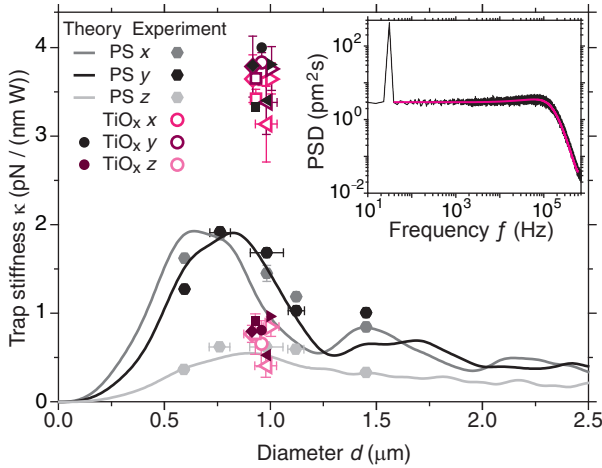


Figure 4.7: *Trap stiffness.* Trap stiffness per power P in the focus of anti-reflection coated titania (TiO_x , \circ x , \circ y , \bullet y theory; different symbols correspond to the batches listed in Table 4.1) and polystyrene microspheres (PS, \bullet x , \bullet y) as a function of microsphere diameter d . Plotted are mean \pm standard deviation. The solid lines ($-$ x , $-$ y) correspond to the T -matrix calculations. Inset: *Power spectral density* (average of 100 individual power spectra) for a titania core-shell microsphere trapped at maximum laser power in water. The spectrum ($-$) features a calibration peak at 32 Hz ($-$ fit to theory, see Section 5.3).

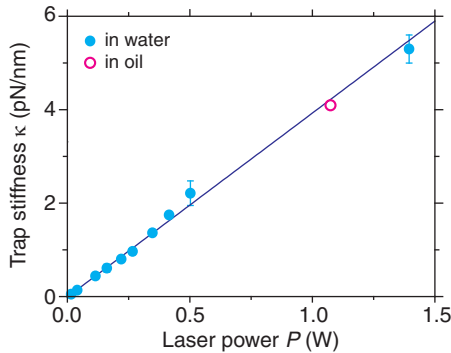


Figure 4.8: *Trap stiffness κ as a function of laser power P in the focus.* The measurements were done in water or oil (\bullet water, \circ oil). The maximum power in water (1.4 W) was higher than in oil (1.1 W) due to a different overfilling ratio (see Section 4.2)

The trap stiffness increased linearly with the laser power P in the focus (Fig. 4.8). At maximum laser power, a power spectral analysis of the particle motion revealed an extremely high corner frequency f_c implying a large trap stiffness $\kappa = 2\pi\gamma f_c$. For a typical power spectrum shown in Fig. 4.7 inset, these values were $f_c = 115$ kHz and $\kappa = 5.1$ pN/nm, respectively. With such a large trap stiffness, I was able to exert large optical forces.

4.6. Nanonewton forces with anti-reflection coated titania microspheres

To demonstrate forces exceeding 1 nN, I performed drag force measurements (Fig. 4.9). First, I measured the drag coefficient γ using the calibration technique automatically accounting for Faxén's law (Section 2.4). Next, I accelerated the sample relative to the stationary laser until the microsphere escaped the trap while simultaneously recording both the microsphere detector signal and the stage position (Fig. 4.9 a). From the speed at escape v_{escape} , I determined the maximum force according to $F_{\text{max}} = \gamma v_{\text{escape}}$. Due to a limiting maximum speed of our piezo-electric translation stage, I had to increase the viscosity of the medium to achieve a sufficiently high drag force to beat the optical trap. I chose water immersion oil with a refractive index comparable to water, however, with a 1000-fold higher viscosity compared to water (see Section 4.2.4). In the oil, I measured a drag coefficient of $\gamma = 3.9 \pm 0.2 \mu\text{Ns/m}$. At a speed of $v_{\text{escape}} \approx 0.3$ mm/s, the titania

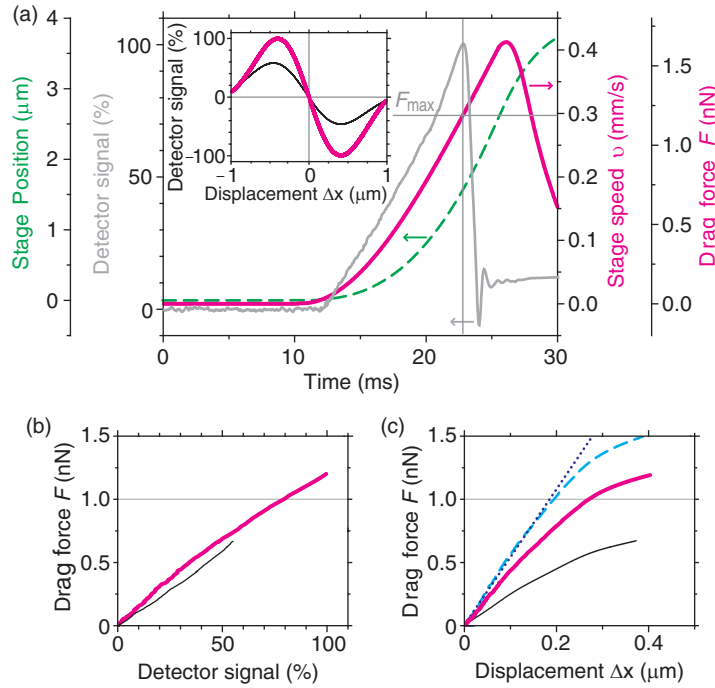


Figure 4.9.: *Escape force measurements in oil.* (a) Simultaneous recording of the microsphere detector signal (—) and sample stage position (---) as a function of time. The stage speed v_{stage} corresponds to the derivative of the stage position. The drag force was $F = \gamma v_{\text{stage}}$ using the measured drag coefficient γ . The vertical (horizontal) gray line marks the escape time (escape speed and maximum force). Ordinate zeros were offset for clarity. Inset: Lateral detector response for an immobilised $1 \mu\text{m}$ diameter titania (—) and $0.992 \mu\text{m}$ diameter polystyrene particle (—) as a function of displacement relative to the trap centre Δx . Drag force as a function of (b) detector signal and (c) displacement inferred from a scan through an immobilised microsphere [inset in (a)]. At the highest detector signal, the microsphere escaped the trap. When the escape force of the titania microsphere was scaled to the maximum trap stiffness measured in water (---), the force was linear in displacement (\cdots) up to $\approx 1 \text{ nN}$. All detector voltage signals were scaled by the maximum voltage $V_{\text{max}}^{\text{titania}}$ recorded for the titania microspheres.

core-shell particles escaped from the trap (Fig. 4.9 a). Based on this speed, I measured a maximum force of $F_{\text{max}} = 1.20 \pm 0.07 \text{ nN}$ (mean \pm SEM) for six different microspheres. The maximum force corresponded to a trapping efficiency $cF_{\text{max}}/(n_{\text{H}_2\text{O}}P) = 0.25$, where c is the speed of light, $P = 1.1 \text{ W}$ was the maximum power in oil (see Fig. 4.8), and $n_{\text{H}_2\text{O}} = 1.33$. Thus, 25 percent of the light power was utilized to exert a force. In comparison, efficiencies for silica-coated polystyrene or $3 \mu\text{m}$ -diameter polystyrene microspheres were only 0.09 and 0.14, respectively [67]. The recorded maximum detector voltage signal at escape was consistent with the maximum value recorded when scanning through an immobilized microsphere (inset Fig. 4.9 a). Furthermore, as expected (see Section 3.3), the drag force scaled almost linearly with the detector signal all the way up to the escape point (Fig. 4.9 b).

4.7. Discussion

My measurements demonstrated both a significant increase in trap efficiency and escape forces exceeding a nanonewton. The increase in trap stiffness was comparable to the difference between polystyrene and silica [67]. Thus, with the anti-reflection-coated titania particles, I had at least a four-fold (two-fold) improvement compared to silica (polystyrene) particles depending on the size [67]. In oil, the nanonewton escape forces were achieved in the regime of the non-linear displacement response of the trap (Fig. 4.9 c) [51]. In water, I achieved a higher maximum laser power in the focus (see Fig. 4.7 b). Therefore, for some microspheres used during the calibration in water, I expected to reach a nanonewton force even within the linear displacement response of $x_{\max}^{\text{linear}} \approx 200 \text{ nm}$ (10 % deviation, see inset of Fig. 4.9 a and Fig. 4.9 c). With a maximum trap stiffness of $\kappa_{\max} = 5.4 \text{ pN/nm}$, I estimated that the maximum force in the linear response range should be $F_{\max}^{\text{linear}} = \kappa_{\max} x_{\max}^{\text{linear}} \approx 1 \text{ nN}$ (Fig. 4.9 c).

The $\approx 1 \mu\text{m}$ diameter of the particles is a compromise between small particles that have a fast response and large particles that provide a contact point for lateral, biomolecule attachment beyond the trapping focus. Microspheres with a larger core diameter of $\approx 0.75 \mu\text{m}$ and outer diameter of $\approx 1.2 \mu\text{m}$ would also enable trapping in the presence of spherical aberrations, however, with a $\approx 20 \%$ lower efficiency compared to the maximum (Fig. 4.1). Fabricating larger particles with high trapping efficiencies should be possible (higher order Mie resonances in Fig. 4.1), though the synthesis of a large, homogeneous shell thickness, according to our knowledge, is nontrivial and was not possible in a general way with a relatively high, non-absorbing refractive index (>1.7) until recently [72]. For smaller diameters with preserved, high trap efficiency, the trapping wavelength would have to be reduced.

The high trap efficiency is either useful to reduce radiation damage in case of sensitive samples, to increase the number of simultaneously trappable particles when splitting the laser into multiple traps [56], or to generate very high optical forces. For high-force measurements, laser-induced heating [63] might be a concern. For the measurements in oil, I estimate that I heated the sample by about 8°C (see Section 4.2.4). In water at maximum laser power, I heated the sample by 3°C (16°C) close to (far away from) the surface—the glass surface acting as a heat sink [63, 77]. To reduce heating, experiments could be performed at a different (smaller) trapping wavelength, in heavy water [78], or other liquids. Since titanium with a native oxide layer is often used as a bio-compatible material and can be functionalized with biomolecules [79], our anti-reflection-coated titania microspheres should be useful for biological applications. Furthermore, an additional thin silica coating on the titania core-shell particles (batch \circ , Table 4.1) did not negatively influence the trapping; silica particles can be readily used for biological experiments (e.g. [58, 67]).

The high trap stiffness in combination with significantly larger microspheres compared to ours, should enable new experiments, for example, to measure resonances associated with the colored nature of thermal noise that drives Brownian motion (see Chapter 5, [77, 80]). Moreover, it has already been demonstrated that high-index particles can also be detected in 3D with unprecedented accuracy using holography, which is fully compatible with a tweezers setup [76]. To increase the working distance, counter-propagating traps with low-numerical aperture lenses have been used. Trapping our coated microspheres in such a geometry should be possible, however, I expect only minor im-

provements compared to uncoated, high-refractive index particles [69]. The advantage of a coating is that lower NA objectives should already be sufficient for trapping in *single-beam* tweezers [68], making the technique simpler and more compatible with other methods. The extended force range of optical tweezers also increases the overlap in force with other techniques such as atomic force microscopy (AFM). Thus, experiments so far restricted to AFM are also feasible with high-resolution optical traps. Apart from 3D scanning with a "stiff" photonic probe, optical tweezers experiments in the nanonewton force range with sub-pN resolution, for instance for protein unfolding or intra- and intercellular measurements, are feasible, can complement or replace AFM approaches, and open up new possibilities taking advantage of the three-dimensional capabilities of optical trapping. Sculpturing optimised photonic structures [57], for example, using two-photon polymerisation [81] to generate gears, rotors, pumps, cell pokers [82] and so forth, will be an essential ingredient for complex, light-driven miniature tools and objects.

Chapter 5

Colored nature of the thermal noise of Brownian motion

The thermal agitation of fluids leads to the random, jiggling motion of suspended particles known as Brownian motion. The random thermal force acting on the particles is often approximated in Langevin models by a “white-noise” process. However, fluid entrainment results in a frequency dependence of this thermal force giving it a “color”. While theoretically well understood, direct experimental evidence for this colored nature of the noise term was still lacking. Here, we tracked the motion of a particle confined in a very strong and ultra-stable optical trap near a surface. By the confinement, we were able to directly measure the color of the thermal noise intensity. Far away from the surface, the noise intensity increased with the frequency approaching a square-root dependence with hints of a resonant enhancement. Close to the surface, the colored-noise amplitude strongly decreased and even reversed its sign. All our measurements were in quantitative agreement with the theoretical predictions, experimentally verifying a key aspect of Brownian motion. Since Brownian motion is important for microscopic, in particular, biological systems and high-resolution biophysical measurements, the colored nature of the noise and its distance dependence to nearby objects need to be accounted for and may even be utilized for advanced sensor applications.

5.1. Noise of Brownian motion

In the Ornstein-Uhlenbeck theory of Brownian motion, the motion is a purely random, markovian—i.e., memoryless—Gaussian process with “white noise” [83, 84]. White noise implies that the noise intensity, i.e., the power spectral density of the noise term in a Langevin model, does not depend on frequency; its power spectral density is flat or constant. “Color” is introduced to the noise by the fluid entrainment of the particle [85–89]. Through its motion, the particle accelerates the entrained fluid [90]. This acceleration depends on the past motion of the particle and introduces an inertial memory effect. In the equation of motion, this non-markovian process is reflected by a frequency-dependent

thermal force that fulfils the fluctuation-dissipation theorem [86–88]. In analogy to filtering white light, this frequency-dependent fluctuation process is often called “colored noise” [84]. Through simulations of Brownian particle motion, the colored-noise effect became evident as a $t^{-3/2}$ -power-law tail at long times of the velocity auto-correlation [91]. Equivalently, the noise intensity is expected to scale with the square root of the frequency $f^{1/2}$ when a confined particle’s position power spectral density is analyzed [92]. The effect is theoretically well-established, but, since it is small, it has not been measured directly [92].

To directly measure the color of thermal noise of classical Brownian motion, i.e. in an incompressible fluid, we used our very stable and strong optical trap (see Section 2.3) in combination with the anti-reflection-coated titania microspheres (see Chapter 4). A trapped microsphere is typically described by an over-damped harmonic oscillator with a relaxation time $\tau = \gamma/\kappa$ with the microsphere drag coefficient γ and the Hookean spring constant or trap stiffness κ . The efficient titania core-shell particles enabled us to achieve a large trap stiffness and, therefore, a small relaxation time or large characteristic frequency $f_c = 1/(2\pi\tau)$. For frequencies $f \ll f_c$, inertial and viscous forces can be neglected in the equation of motion [92]. Then the optical force $F_{\text{trap}} = \kappa x$ directly balances the random, thermal force $F_{\text{thermal}} = F_{\text{trap}}$. Thus, in this limit, the displacement x in a strong, calibrated optical trap is a direct measure for the thermal force and its dependence on the frequency and distance to a nearby surface [49, 92]. Here, we measured this dependence and found quantitative agreement between theory and experiment.

The work presented in this chapter has been published by Jannasch, Mahamdeh and Schäffer in Physical Review Letters in 2011 [77].

5.2. Ultra-stable trap and anti-reflection coated titania microspheres to measure the colored noise of Brownian motion

To quantitatively measure the small colored-noise effect, we used our ultra-stable optical tweezers setup ‘Aswad’ (see Section 2.3). The objective overfilling was 2 (Section 2.3), resulting in a diffraction limited spot with 1.05 W power. The sampling rate was 1.25 MHz (NI PXI-6251, National Instruments, Austin, TX). To minimize drift, the temperature of the two objectives was kept constant at $33.000 \pm 0.001^\circ\text{C}$.

Resolution and noise At low frequencies, our measurements were limited by $1/f$ noise. At high frequencies, the characteristic frequency f_c of the trapped particle was limiting. Slow drift sometimes affected the whole frequency range, e.g., due to fluctuations of the detector sensitivity or the room temperature. Since the magnitude of the colored-noise effect was on the percent level, drift and resolution of the measurement had to be smaller. To reach a $N^{-1/2} = 1\%$ precision in a power spectral analysis, at least $N = 10\,000$ power spectra have to be averaged [50, 92]. To acquire enough power spectra in a time window that is not affected by drift, we decreased the frequency resolution of the measurement and, therefore, the total measurement time t_{msr} . The system was stable over 500 s such that we achieved a 0.3% rms-noise level ($N = 100\,000$) with a 200 Hz resolution. In this time period, the magnitude of drift was less than the relative displacements

in the trap. For a strong trap, the displacements were on the order of $1 \text{ pm}/\sqrt{Hz}$ (see Section 5.3, Fig. 5.1) imposing stringent stability conditions on the apparatus. To ensure that our measurements were not affected by drift, we acquired one 12.5 s-long calibration spectrum before and after each long-duration, high-precision measurement (Fig. 5.1). Only if the two calibration spectra, the high-precision spectrum, and the according fits to the data agreed within error bars, the drift was low enough. In this manner, we acquired high-precision power spectra as a function of distance from the surface l . To trap at the largest distance, $\approx 20 \mu\text{m}$ from the surface, we used an immersion oil with a refractive index of 1.53 to compensate for spherical aberrations [18, 47, 66]. At this distance, we could acquire only $N = 10\,000$ spectra; our measurements were limited by low-frequency noise presumably due to laser heating [63] and subsequent convective currents [93].

Anti-reflected coated titania microspheres as probes As probes we used the anti-reflection-coated titania microspheres (see Chapter 4). The microspheres had a diameter of $1.00 \pm 0.04 \mu\text{m}$ and were suspended in aqua bidestillata ($18.2 \text{ M}\Omega\text{cm}$, $\rho_{\text{water}} = 1000 \text{ kg m}^{-3}$). The average density of the titania core-shell microspheres was $\rho_{\text{titania}} = 2500 \text{ kg m}^{-3}$ (see Section 4.4).

5.3. The noise of Brownian motion is colored

The measured power spectra were in quantitative agreement with the theoretical predictions. The Langevin equation of motion for the position $x(t)$ of the trapped microsphere with diameter d and mass m moving parallel to a surface at a distance ℓ from the microsphere center is $m\ddot{x} + \gamma(f, d/2\ell)\dot{x} + \kappa x = F_{\text{thermal}}$ with the thermal noise $F_{\text{thermal}}(f) = [2k_{\text{B}}T\text{Re}\{\gamma(f, d/2\ell)\}]^{1/2}\xi(f)$ [92]. The white-noise process is characterized by $\langle \xi(t) \rangle = 0$ and $\langle \xi(t)\xi(t') \rangle = \delta(t-t')$ where δ is Dirac's delta function and $\langle \dots \rangle$ denotes the expectation value. The hydrodynamically correct one-sided power spectral density for the microsphere's position with Fourier transform $\tilde{x}(f)$ is then given by [49, 94]

$$P_{\ell}(f) = \langle |\tilde{x}(f)|^2 \rangle = \frac{(D_0/\pi^2) \text{Re}\{\gamma/\gamma_0\}}{(f_c + f \text{Im}\{\gamma/\gamma_0\} - f^2/f_m)^2 + (f \text{Re}\{\gamma/\gamma_0\})^2} \quad (5.1)$$

The frequency- and distance-dependent drag coefficient is Padé approximated to [49]

$$\gamma(f, d/2\ell) = \frac{\gamma_0 \left[1 + (1-i)\sqrt{f/f_{\nu}} - i\frac{2}{9}(f/f_{\nu}) \right]}{1 - \frac{9}{16}(d/2\ell) \left\{ 1 - \frac{1}{3}(1-i)\sqrt{f/f_{\nu}} + i\frac{2}{9}(f/f_{\nu}) - \frac{4}{3} \left[1 - \exp\left(- (1-i)[(4\ell/d) - 1]\sqrt{f/f_{\nu}}\right) \right] \right\}} + \dots \quad (5.2)$$

where $\gamma_0 = 3\pi\eta d$ is the Stokes drag coefficient with the viscosity η . The diffusion coefficient far away from the surface is $D_0 = k_{\text{B}}T/\gamma_0$ with the Boltzmann constant k_{B} and the temperature T . There are three characteristic frequencies for (i) the power spectral density corner $f_c = \kappa/(2\pi\gamma_0)$, (ii) inertial effects $f_m = \gamma_0/(2\pi m)$, and (iii)

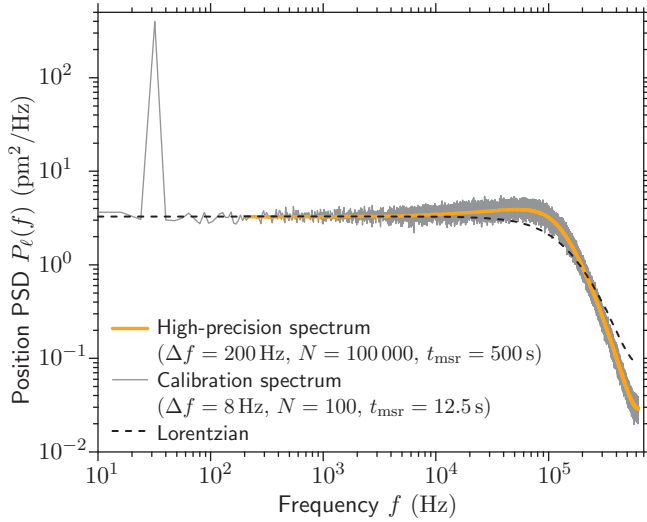


Figure 5.1: *Power spectral density.* “High-precision” and “calibration” position power spectral density of an anti-reflection-coated titania microsphere held in an optical trap at a distance $2\ell/d = 12$ from the surface. The calibration (—) and high-precision (—) spectrum shown are the average of 100 and 100 000 independent power spectra, respectively. On the scale of the figure, fits of Eq. 5.1 to the data are indistinguishable from the high-precision spectrum. The calibration spectrum with a $\Delta f = 8$ Hz frequency resolution features a peak at the 32 Hz stage driving frequency used for calibration. A Lorentzian (---) is plotted for comparison. Deviations from the Lorentzian are due to the “colored noise” intensity of the thermal force.

viscous entrainment effects $f_\nu = 4\nu/(\pi d^2)$ where $\nu = \eta/\rho$ is the kinematic viscosity with the liquid density ρ . Re and Im are the real and imaginary part of a complex number, respectively.

We fitted Eq. (5.1) in the range of 1–100 kHz to a “high-precision” and “calibration” position spectral density of an anti-reflection coated titania microsphere held in the optical trap (Fig. 5.1) at a surface distance of $2\ell/d = 12$. The calibration and high-precision spectra are the average of 100 and 100 000 independent power spectra, respectively. The fit parameters were the corner frequency f_c and the diffusion coefficient D^{volt} defined as $D_0 = \beta^2 D^{\text{volt}}/[1 - (9/16)(d/2\ell)]$. Constant parameters in the fit were the microsphere diameter $d = 0.51 \mu\text{m}$, its density $\rho_{\text{core-shell}}$ (see Section 4.4), the water density ρ_{water} , the distance ℓ , and the number of averaged power spectra $N = 100\,000$. The calibration spectrum with a $\Delta f = 8$ Hz frequency resolution features a peak at the 32 Hz stage driving frequency. From the power in the “calibration peak”, the displacement sensitivity β was calculated. In addition, we used a low pass with filter frequency $f_{3\text{dB}} = 360$ kHz to account for the finite bandwidth of the photo diode [50]. A Lorentzian is plotted for comparison. Deviations from the Lorentzian are due to the “colored noise” intensity of the thermal force.

Furthermore, we fitted Eq. (5.1) to high-precision spectra at different distances from the surface, normalized the power spectral density by its extrapolated, fit-based value at $f = 0$, and subtracted one (Fig. 5.2). The frequency axis was scaled by the corner frequency f_c because three different microspheres were used and the different distances lead to different temperatures (see below). The resulting fit parameters are listed in Table 5.1. Based on the assumption that the microsphere diameter and its distance to the surface is known, we determined the temperature by varying T until the experimentally measured value for the drag coefficient γ_{ex} at $f = 0$ was equal to the theoretically expected one: $\gamma_{\text{ex}} - \gamma = k_B T / (\beta^2 D^{\text{volt}}) - 3\pi\eta(T)d/[1 - (9/16)(d/2\ell)] = 0$. Since the viscosity $\eta(T)$ is a non-linear function of temperature, we numerically solved for it. The standard error of the temperature was dominated by the error of the microsphere size amounting to about $\pm 2^\circ\text{C}$. The measured temperature increased with distance from the surface [grey

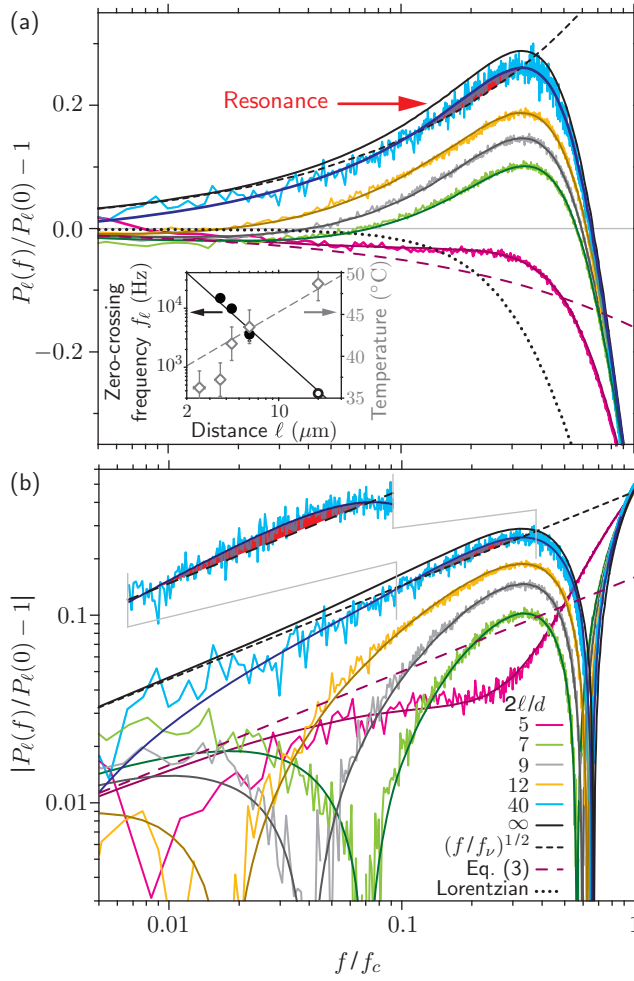


Figure 5.2: High-precision power spectra as a function of surface distance. High-precision power spectra for different microsphere-center-surface distances $2\ell/d$ on (a) a semi-log and (b) the absolute value on a log-log scale. Smooth solid lines are fits of Eq. 5.1 to the data. The parameters are given in Table 5.1. Equation (1) for $2\ell/d \rightarrow \infty$ (—), a Lorentzian (\cdots), and the positive and negative square-root scaling $\sqrt{f/f_\nu}$ (---) and Eq. (5.3) (--- for $2\ell/d = 5$), respectively, are drawn for comparison. The frequency axis was scaled by the corner frequency f_c . The red shaded area is a resonant enhancement of the colored noise intensity. Inset: Zero-crossing frequency. Zero-crossing frequency [\bullet (\circ) based on data (fit)], $f_\ell = \nu/(2\pi\ell^2)$ (---), temperature (\diamond , Table 5.1), and temperature model (---, [63]) as a function of distance ℓ .

diamonds, inset Fig. 5.2(a)]. This increase was due to laser heating and the surface acting as a heat sink—in quantitative agreement with a model (grey dashed line) with no adjustable parameters [63]. Over the fitted range and for all distances, Eq. (5.1) deviated on average less than $\sqrt{\chi_{\text{red}}^2/N} \lesssim 1\%$ from the experimental power spectral density (see Table 5.1).

The magnitude and scaling with frequency of the colored noise intensity strongly depended on the distance to the surface (Fig. 5.2). In the limit of $2\ell/d \rightarrow \infty$, a Taylor expansion in frequency around $f = 0$ of the power spectral density [Eq. (5.1)] results to lowest order in $P_{\ell=\infty}(f)/P_{\ell=\infty}(0) = 1 + \sqrt{f/f_\nu} + \dots$ [92]. Thus, far away from the surface, the color of the noise intensity scales with the square root of the frequency and only depends on the particle size and the *kinematic* viscosity—it is an *inertial* effect of the entrained fluid [92]. This scaling is plotted in Fig. 5.2 with a black short-dashed line. For *finite* values of $2\ell/d$, the resulting scaling is

$$P_\ell(f)/P_\ell(0) = 1 - \frac{\sqrt{f/f_\nu}}{2[1 - \frac{9}{16}(d/2\ell)]} + \dots \quad (5.3)$$

Interestingly, in this case, the colored part of the noise intensity depends on ℓ and is negative. For a low enough bandwidth, this sign reversal means that noise is suppressed

Table 5.1.: *Fit parameters.* Fit parameters of Eq. (5.1) for the power spectral density measurements for different surface distances $2\ell/d$ (data and fits shown in Fig. 5.2). Based on the number of fitted data points, the error of the reduced χ^2 -value is ± 0.06 . For the farthest surface measurement ($2\ell/d=40$), the number of averaged power spectra was only 10 000.

$2\ell/d$	f_c (kHz)	D^{volt} (V^2/s)	β (nm/V)	T ($^\circ\text{C}$)	χ_{red}^2
5	71.54 ± 0.02	1010 ± 1	23.59 ± 0.01	36	1.21
7	148.2 ± 0.1	1402 ± 2	20.61 ± 0.02	37	1.07
9	156.9 ± 0.2	1485 ± 3	21.15 ± 0.03	42	1.13
12	155.7 ± 0.2	1484 ± 4	21.81 ± 0.03	44	1.59
40	181.0 ± 0.8	1820 ± 20	21.12 ± 0.09	49	1.11

due to the entrained fluid and coupling to the surface. We indeed observed such a suppression up to a characteristic frequency f_ℓ at which a zero-crossing occurred in the normalized plot of Fig. 5.2. The frequency of these zero-crossings (black circles, inset Fig. 5.2 a) scaled with ℓ^{-2} and was well-approximated by an estimate of $f_\ell \approx \nu/(2\pi\ell^2)$ (black solid line, inset Fig. 5.2 a). Up to which frequency noise is reduced depends on the exponential term in Eq. (5.2). Setting the real part of the exponent to -2 , meaning a reduction by $e^{-2} \approx 86\%$ and assuming $\ell \gg d/2$, results in the stated estimate for the frequency f_ℓ . The negative-square-root scaling of the colored noise according to Eq. (5.3) was approached for the $2\ell/d = 5$ data (magenta long-dashed line in Fig. 5.2). The positive-square-root scaling (black short-dashed line in Fig. 5.2) was nearly reached for our $2\ell/d = 40$ data set. However, even at this distance, there was still a significant deviation from the scaling behavior expected at infinite distance (black solid line in Fig. 5.2).

For this largest distance, we measured a small resonant enhancement of the colored noise intensity. For $f_\nu \rightarrow f_c$, the harmonic oscillator is not over-damped anymore. This results in a resonance that shows up as increased noise beyond the positive-square-root scaling [80]. The red-shaded area in Fig. 5.2 marks this small, but significant, resonant enhancement. To enhance this effect even further, f_ν/f_c needs to be decreased. Since for our setup f_c was already maximized and our microsphere size was fixed [72], we reduced the kinematic viscosity. However, excessive heating of various liquids precluded such experiments.

5.4. Discussion

We directly measured the colored nature of the thermal noise of Brownian motion. By the scaling of the noise amplitude with $(f/f_\nu)^{1/2}$, we could confirm that the origin of this colored noise was due to the acceleration of the entrained fluid, i.e. an inertial effect. Furthermore, the strong dependence of the colored-noise amplitude and scaling on the distance may open up the possibility to use the effect as a sensitive means to determine the presence of far away objects. Since the frequency f_ℓ at which the sign-reversal occurred scaled with ℓ^{-2} , this frequency may be used as a sensitive indicator. Brownian motion is key to biological systems. Thus, the colored nature of the underlying noise process—and in particular its dependence on distance—may play a significant role in the crowded cellular environment. Furthermore, for sensitive biophysical measurements (e.g. [94–96]) the effect has to be accounted for. The resonance—once enhanced further—may even be exploited for advanced force spectroscopy measurements. Finally,

other colors of noise are often based on the frequency of visible light [97]. Since the here-discussed noise has a weak, square-root dependence on frequency resulting in a lower frequency band than, for example, blue noise ($\propto f$), we suggest the color of thermal noise of Brownian motion to be yellow.

Part II.

Kinesin-8

Chapter 6

Introduction

6.1. Biological background

6.1.1. Microtubules are important structures in cells

The cytoskeleton is a cellular scaffold and composed of three types of filaments: actin filaments, intermediate filaments and microtubules. Microtubules play a major role in the mechanical stability of the cell and controlling the cell shape. They are also the structural basis of cilia and flagella and therefore affect cell motility. Furthermore, microtubules are forming the spindle during mitosis and serve as tracks for transport of vesicles and organelles by motor proteins [98].

Microtubules consist of tubulin α - β heterodimers with a length of 8.2 nm. Both tubulins have a negative charged C-terminus (E-hook). The tubulin dimers associate in a head-to-tail fashion to form linear protofilaments. Several protofilaments (*in vivo* usually 13) bind laterally to form a sheet. Finally, the sheet curves to form a hollow cylinder of approximately 25 nm diameter and several micrometer length, that gives the microtubule a high rigidity [99]. Furthermore, the protofilaments are slightly shifted against each other, which results in a helical structure. Due to the asymmetry of the dimer, the microtubules are polar. (Fig. 6.1) [100].

Microtubules show dynamic instability [100–102]. It is widely believed that the dynamic instability of microtubules is linked to the GTPase activity of the tubulin heterodimer [103]. Each heterodimer binds two guanosine-5'-triphosphate (GTP) molecules. While growing, GTP-tubulin gets incorporated into the microtubule lattice. The GTP in the

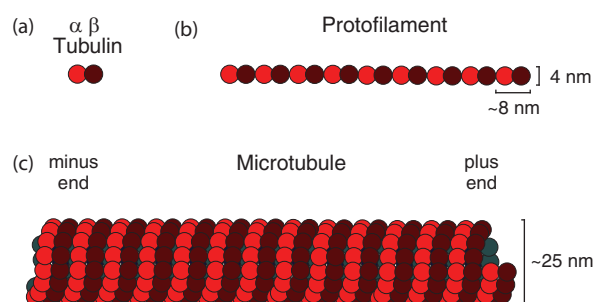


Figure 6.1: Schematic structure of a microtubule. (a) α - β -tubulin dimer (b) associate head-to-tail to form linear protofilaments. (c) Several protofilaments bind laterally to form a hollow cylindrical tube. The orientation of the tubulin heterodimers defines the microtubule polarity.

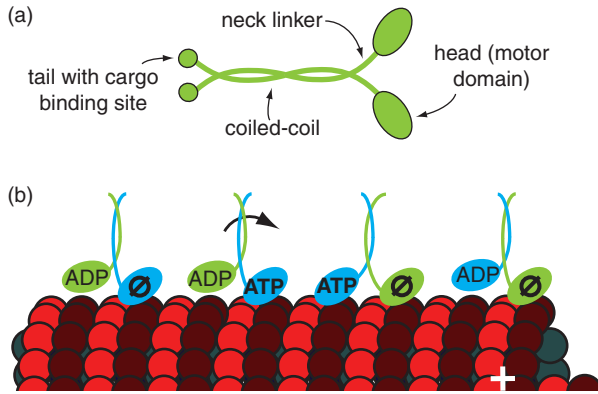


Figure 6.2: (a) *Schematic structure of conventional kinesin.* The dimeric kinesin contains two motor domains, a neck linker, a coiled-coil region and a tail with a cargo binding site. (b) *Walking mechanism of kinesin-1.* Kinesin-1 walks in a hand-over-hand mechanism along the microtubule towards the plus end. Each step is associated with one cycle of ATP hydrolysis. The motor domain is tightly-bound to the microtubule in the ATP and in the nucleotide free (\emptyset) state.

α -tubulin is non-exchangeable and not hydrolyzed. The GTP of the β -tubulin can be hydrolyzed to guanosine-5'-diphosphate (GDP), but the GTPase activity of a free tubulin dimer is very slow. The hydrolysis activity is stimulated upon incorporation of the dimer into the growing plus end and accelerated by addition of the next tubulin dimer. Thus, the microtubule lattice is composed mainly of GDP-tubulin, with a cap of GTP-tubulin at the growing microtubule plus end. A GTP-tubulin cap is suggested to be crucial for the stabilized microtubule plus end, since a pure GDP-tubulin lattice would depolymerize immediately. For *in vitro* measurements, microtubules can be stabilized by using the slowly hydrolyzable GTP analogue guanosine-5' [α , β -methylene]-triphosphate (GMPCPP) [104].

In order to fulfil the various functions of the microtubule cytoskeleton, controlling the microtubule network is very important. *In vivo* microtubule-associated proteins (MAPs) play an important role in regulating the dynamic instability. There are several MAPs known, which polymerize (e.g. XMAP215 [105]), depolymerize (e.g. MCAK, Kip3, Kif18A [106–110]) or stabilize (e.g. Map2/Tau [111]) microtubules.

6.1.2. Kinesins are microtubule based motor proteins

Kinesins are classified in 14 subfamilies [112, 113]. They share an evolutionary-conserved motor domain, which hydrolyzes adenosine triphosphate (ATP) and can bind to microtubules. The motor domain is most often found close to the N-terminus of the protein. Most kinesins contain a coiled-coil region that is necessary for forming dimers or tetramers and a neck linker. The rest of the domains are usually referred to as tail (Fig. 6.2 a)[113]. Beside the motor domain, other sequences of the protein are poorly conserved and important for the specific functions of the different kinesins [114]. For example, kinesin-1 is an anterograde axonal transport motor [114], kinesin-5 is a tetramer and slides anti-parallel microtubules in the mitotic spindle [115], kinesin-8 move processively on microtubules towards the plus end and depolymerizes them [107], kinesin-10 contains a DNA binding motif and is associated to chromosomes [116], kinesin-13 diffuses on microtubules and de-stabilizes them [106], kinesin-14 has a motor domain located in the C-terminus and moves to the microtubule minus end [117].

Conventional kinesin moves with a velocity of ≈ 800 nm/s and can generate forces of up to 7 pN at saturated ATP concentrations [118]. It takes about one hundred 8 nm steps (the size of tubulin heterodimers composed of α and β subunits) before it detaches from the microtubule [119–121]. It walks in a hand-over-hand mechanism processively

towards the microtubule plus end with a run length of more than $1\ \mu\text{m}$ [122, 123]. Each step is associated with one cycle of ATP hydrolysis, which is illustrated in Figure 6.2 b [124, 125]. The stepping is triggered by conformational changes in the ATP-bound head of kinesin [126]. In this manner, kinesins are able to convert chemical energy from ATP hydrolysis into mechanical work.

During processive movement, it has been shown that at least one head is tightly-bound to the microtubule. The binding mode of kinesin depends on the nucleotide states. The motor domain binds tightly to the microtubule in the ATP and in the nucleotide free state [100, 121]. In the presence of ADP, the motor domains are weakly-bound and diffuse on the microtubule lattice [67, 127, 128].

6.2. Motivation

Control of microtubule length is crucial for chromosome alignment and separation during mitosis, but how length is controlled exactly is unknown [129–131]. Recently, it was shown that members of the kinesin-8 motor family regulate the dynamics of microtubules. The budding yeast kinesin-8, Kip3, acts cooperatively to mediate length-dependent microtubule depolymerization [107, 109, 132]. Human kinesin-8, Kif18A, also antagonizes microtubule growth, though the mechanism is still under debate [108, 131, 133, 134]. To modulate microtubule dynamics, it is essential for these motors to reach the microtubule plus ends. Kinesin-8s are highly processive motor proteins. Their run length is about $10\ \mu\text{m}$ [107, 135–137], which is the longest observed for microtubule-related motor proteins. This high processivity is surprising given that there is no evidence that kinesin-8s function as cargo transporters like kinesin-1, for which processive motility is an obvious functional adaptation. The high processivity of kinesin-8s has recently been shown to be due, in part, to a second microtubule-binding domain in the non-motor domain, which increases the run lengths up to four-fold [135–137]. Thereby, plus-end localization is facilitated [137–139], which is important for the microtubule-regulating activities [135, 136]. However, even without the additional microtubule-binding domain, the run lengths of truncated kinesin-8s are still up to about $4\ \mu\text{m}$ and at least twice that of kinesin-1 [140].

In this thesis I wanted to better understand the stepping mechanism of this kinesin class, in particular its high processivity. Therefore, I tracked precisely the translocation of kinesin-8 motors subjected to both hindering and assisting load forces *in vitro* with an optical tweezers. We found that kinesin-8 is a slow, low-force motor with a weakly-bound slip-state, which is off the main pathway of its regular mechano-chemical cycle [141]. These results are consistent with preliminary results obtained by Volker Bormuth [142]. Weakly-bound or frictional states [143] are important for the force generation by muscle myosin [144], collective properties of molecular motors [145], and for efficient search of target sites via one-dimensional diffusion in the case of DNA enzymes [146] and microtubule-associated proteins [105, 106, 147, 148]. For kinesin-8, we argue that the weakly-bound state may contribute to the motor's high processivity.

Chapter 7

Kinesin-8 assay

Kinesin-8 is a highly conserved, microtubule plus-end-directed motor protein. Different kinesin-8 family members have been shown to play an important role during mitosis. In order to study the function of the budding yeast (Kip3) and the human (Kif18A) kinesin-8 in detail, optical tweezers were used as a force and position sensitive tool. The kinesin-8 proteins were expressed and purified to homogeneity. To manipulate the molecule, the green fluorescent protein tagged kinesin-8's were attached to the microsphere surface via an elastic polyethyleneglycol linker without affecting their function.

7.1. Expression and purification of kinesin-8

All constructs were expressed in insect cells. We used the BAC-TO-BAC expression system (Invitrogen, Paisley, UK). The constructs were transferred in Sf+ cells. Cells were grown at 27 °C for several days and the expression of GFP was monitored by fluorescence microscopy. The cells were lysed and the lysate centrifuged. The supernatant was frozen and stored in liquid nitrogen.

The budding yeast kinesin-8 construct—6xHis-Kip3-eGFP (Kip3)—was purified from the cleared cell lysate by a combination of cation-exchange (HiTrap SP-HP, Amersham Biosciences) and metal-affinity chromatography (HiTrap HP, Amersham Biosciences). The metal-affinity chromatography yielded fractions of highly enriched and purified recombinant proteins. SDS-PAGE (sodium dodecyl sulfate polyacrylamide gel electrophoresis), a technique to separate proteins according to their size, showed dominant bands at 130 kDa (Fig. 7.1). The purified proteins were snap frozen in liquid nitrogen in the elution buffer with 1 mM dithiothreitol (DTT) [107].

The concentration of Kip3 was determined with a Bradford assay (Bio-Rad protein assay). Bradford is a simple and accurate procedure for determining concentration of solubilized protein. It involves the addition of a protein assay dye reagent (containing dye, phosphoric acid, and methanol) to the protein solution, and subsequent absorption measurement at 595 nm with a micro-plate reader. Comparison to a standard curve provides a relative measurement of protein concentration [149]. As a standard, I used

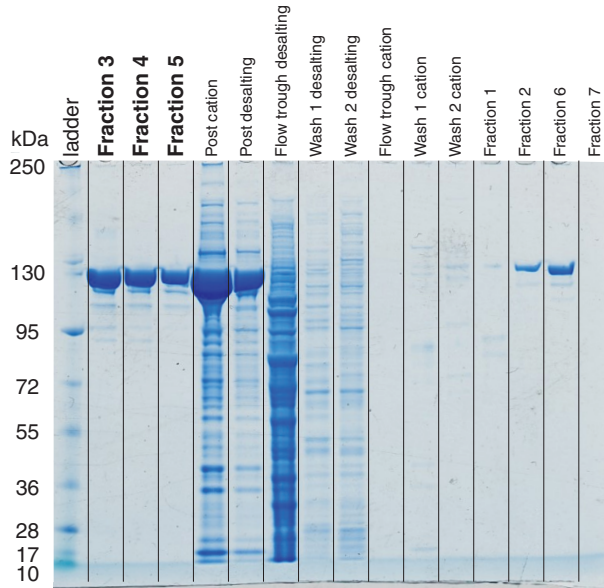


Figure 7.1: *SDS-Page of purification of 6xHis-Kip3-eGFP.* SDS-PAGE of Kip3 lysate and purified fractions of Kip3 after metal affinity chromatography. The purified Kip3 fractions show a dominant band at 130 kDa.

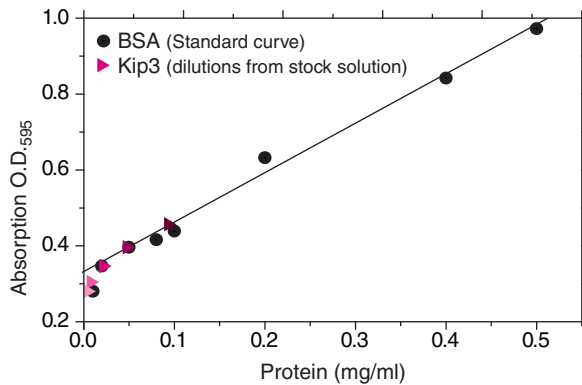


Figure 7.2: *Bradford measurement.* Different dilutions of Kip3 (2×, 4×, 8×, 16×, 32×, from stock solution) are plotted relative to the standard curve (BSA, ●).

BSA (bovine serum albumin). With this method I determined a Kip3 concentration of ≈ 0.16 mg/ml (Fig. 7.2).

The human kinesin-8 constructs—6xHis-Kif18A-eGFP (full length, Kif18A) and 6xHis-Kif18A777-eGFP (truncated, AA 1-777, Kif18AT777)—were purified from the cleared cell lysate by a cation-exchange (HiTrap SP-HP, Amersham Biosciences). The expression and purification of the Kif18A constructs were done by Marko Storch (MPI-CBG, Dresden). The expressions and purifications of all investigated proteins (Kip3, Kif18A, Kif18AT777) is described in further detail in [107, 108, 150].

7.2. Coupling of kinesin to PS microspheres

Functional coupling of kinesin-8 proteins to microspheres is essential for position and force measurements with optical tweezers. For a functional coupling of the motor protein to the microsphere, I used polyethylene-glycol (PEG) as an elastic linker. PEGs are non-toxic, highly water soluble and able to couple with proteins, maintaining functionality.

First, I covalently attached a PEG layer to the carboxylated polystyrene (PS) microsphere. In the next step, I covalently bound an enhanced-green-fluorescent-protein anti-body (anti-eGFP). After incubating the PS-PEG-anti-eGFP microspheres with the

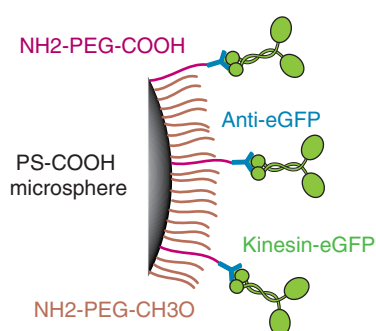


Figure 7.3: Schematic drawing of the kinesin-8 microsphere coupling. (not to scale) The reactive PEGs (NH₂-PEG-COOH) and the non-reactive methylated PEGs (NH₂-PEG-CH₃O) (1:9) that form non-reactive spacers on the microsphere surface are covalent bound to the microsphere. At the activated carboxyl groups of the PEG, anti-eGFP are covalently bound. Finally, the eGFP-tagged kinesin-8 tail bound to the anti-eGFP.

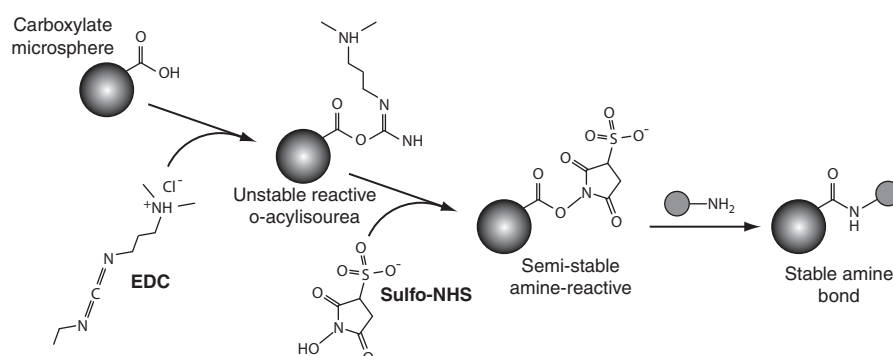


Figure 7.4.: Schematic of a carboxyl group activation and cross linking with EDC and Sulfo-NHS. (adapted from Bioconjugated Techniques [151])

eGFP-tagged kinesin-8 proteins, the proteins were bound with the tail fused GFP to the microsphere (Fig. 7.3). The detailed protocol is described in the Appendix A.3.

Activation of carboxylated polystyrene microspheres (PS-COOH) The polystyrene microspheres with a size of 0.59 μm , were functionalized with carboxyl groups. The carboxyl groups were activated by using EDC and Sulfo-NHS. EDC is a zero-length cross linking agent used to couple carboxyl groups to primary amines. It reacts with the carboxyl group, forming an amine-reactive O-acylisourea intermediate. The intermediate is susceptible to hydrolysis, making it unstable and short-lived in aqueous solution. The addition of Sulfo-NHS stabilizes the amine-reactive intermediate by converting it to an amine-reactive Sulfo-NHS ester, thus increasing the efficiency of EDC-mediated coupling reactions (Fig. 7.4, adapted from [151]). The half-life of NHS ester is dependent on the pH. I used a solution with pH = 6.0.

Pegylation (PS-PEG) I used functionalized (i) reactive PEGs with carboxyl groups on one end and amine groups on the other (3 kDa, NH₂-PEG-COOH) as linker and (ii) non-reactive methylated PEGs (1:9, 2 kDa, NH₂-PEG-CH₃O) that form non-reactive spacers on the microsphere surface. The contour lengths of the PEGs were 23.4 nm and 15.7 nm, respectively. The activated carboxyl groups on the microsphere surface reacted with amine groups of both PEG spacer molecules (Fig. 7.3).

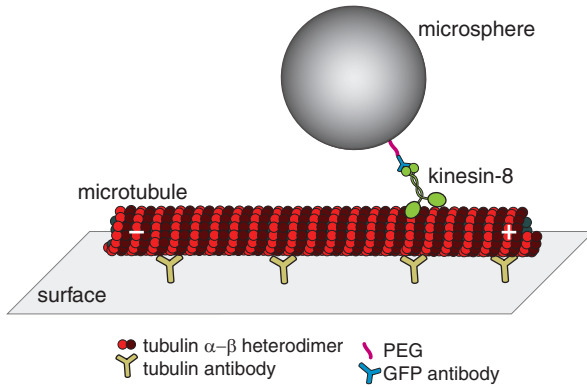


Figure 7.5: Schematic of a stepping assay. A single kinesin-8 protein—bound to a microsphere—walks on a microtubule. The microtubule is attached via a tubulin antibody to the surface (not to scale).

Anti-body coupling to PEG (PS-PEG-anti-eGFP) The carboxyl groups at the other end of the 3 kDa PEGs were activated by a second carbodiimide reaction identical to the first activation. The eGFP anti-bodies reacted with the activated carboxyl groups of the PEGs. The microspheres were stored in PBS (phosphate buffered saline) buffer at 4 °C and used for three weeks. The microsphere concentration was determined by comparison of the transmission curves of the PS-PEG-anti-eGFP microspheres with the transmission curve of different dilutions of the stock PS microsphere solution. I lost $\approx 60\%$ of the microspheres, because of the different washing steps between the activations.

Kinesin-8 binding to the microsphere (PS-PEG-Kinesin-8) Before every experiment, kinesin-8 was incubated with the prepared microspheres. The eGFP at the tail of the kinesin-8 bound to the eGFP antibody at the end of the PEGs (Fig. 7.3).

7.3. Stepping assay

In the stepping assay, microtubules were attached to a surface, where they form tracks for the kinesin motor (Fig. 7.5). In my case, the motor was attached to a microsphere, which I used as a handle for optical tweezers measurements. The detailed protocol is described in Appendix A.3.

7.3.1. Sample Preparation

GMPCPP microtubules For the measurements, I used GMPCPP-stabilized microtubules. GMPCPP is a slowly hydrolyzable GTP analog. The microtubules were assembled in BRB80 supplemented with 1 mM MgGMPCPP (Bioscience, Jena) containing porcine brain, rhodamine-labeled tubulin (0.5 μ M rhodamine-labeled tubulin and 1.5 μ M unlabeled tubulin). The mixture was incubated for 2 hours at 37 °C, pelleted in an airfuge and re-suspended in BRB80 (for detailed protocol, see Appendix A.3).

Flow cell preparation Stepping assay measurements were performed in passivated flow cells (see Section 2.3.4). To immobilize microtubules, the channels were incubated with a series of buffers. First, tubulin antibody in PBS buffer (pH = 7.4) was incubated for 5 min, followed by a 20 min incubation with 1 % Pluronic F-127 in BRB80. Subsequently,

channels were rinsed with 80 μ l of BRB80 and finally GMPCPP-stabilized microtubules in BRB80 were added to the antibodies for 15 min (for detailed protocol, see Appendix A.3).

7.3.2. TIRF assay

For control measurements we performed total internal reflection fluorescence (TIRF) stepping assays. The kinesin-8 motors were diluted in motility solution and then flushed into the prepared flow cell containing the immobilized microtubules. The motility solution consisted of BRB80 with 112.5 mM KCL, 0.1 mg/ml casein, 1 mM Mg-ATP, and an anti-fade mix consisting of 0.5 Vol% β -mercaptoethanol, 20 mM D-glucose, 20 μ g/ml glucose oxidase and 8 μ g/ml catalase. Single kinesin-8 proteins—labeled with eGFP (green)—were visualized by TIRF microscopy. The microtubules—labeled with rhodamin (red)—were observed by epifluorescence microscopy.

7.3.3. Optical tweezers assay

Kinesin-8 was incubated with the prepared PS-PEG-anti-eGFP microspheres for 7 min at room temperature. The kinesin-8-functionalized microspheres were diluted in motility solution (the same as for TIRF) and then added to the flow cell with the immobilized microtubules (for detailed protocol, see Appendix A.3). The measurements were performed at 24.5 °C in the 'MPI-CBG' optical tweezers setup (see Section 2.3.1). Signals were recorded in three dimensions with a position-sensitive photodiode in the back-focal plane. Time traces were recorded with 20 kHz. All measurements were done with approximately the same trap stiffness $\kappa = 0.04$ pN/nm.

7.4. The kinesin-microsphere coupling is functional

The purified Kip3, Kif18A and Kif18AT777 molecules showed full functionality. In TIRF assays, the proteins translocated highly processive along microtubules. An example kymograph of single Kip3 movements on a microtubule is shown in Figure 7.6 a. The average speed was 41 ± 4 nm/s (mean \pm SEM, N=10). Furthermore, at high protein concentrations, the Kip3 construct showed length-dependent microtubule depolymerization (Fig. 7.6 b). In conclusion, the expressed and purified kinesin-8s were functional.

The kinesin-coated microsphere showed motility with preserved motor functionality.

For testing the functionality, kinesin-8-coated microspheres were positioned on a microtubule with the optical trap. Then, I blocked the laser by closing the shutter. At high kinesin concentration, almost all tested microspheres showed motility. To test, if the coupling of kinesin-8 to the microsphere affected the functionality of the motor, I compared the average velocity of free motors (measured with TIRF) to the one of motors attached to microspheres (with optical trap switched off). The microsphere position and velocity was tracked by differential interference contrast (DIC) microscopy images employing a light emitting diode (Fig. 7.7) [45]. Under single-molecule conditions (see Section 7.5), the microsphere velocity was 45 ± 2 nm/s (SEM, N=10) for Kip3, 162 ± 10 nm/s (SEM, N=6) for Kif18A and 173 ± 11 nm/s (SEM, N=4) for Kif18AT777. Within the error

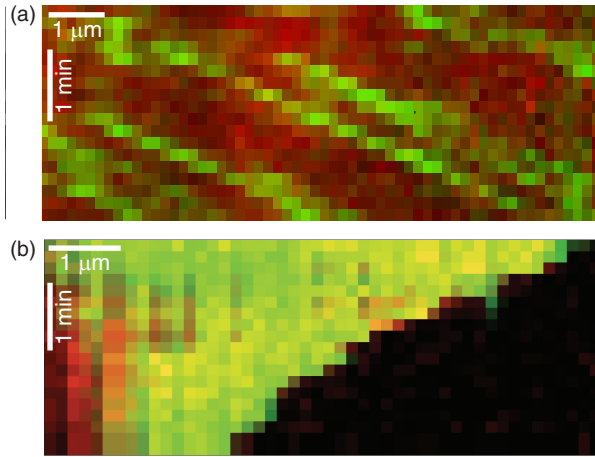


Figure 7.6: *Kymographs of Kip3 molecules.* Kymograph of (a) single Kip3 molecules translocating along a microtubule with an average velocity of 40 ± 6 nm/s (SEM, $N = 4$) and (b) multiple Kip3 molecules depolymerizing a microtubule. The microtubule depolymerization was length dependent with a depolymerization rate of up to $2.1 \mu\text{m}/\text{min}$. The measurements were performed at room temperature and 1 mM ATP.

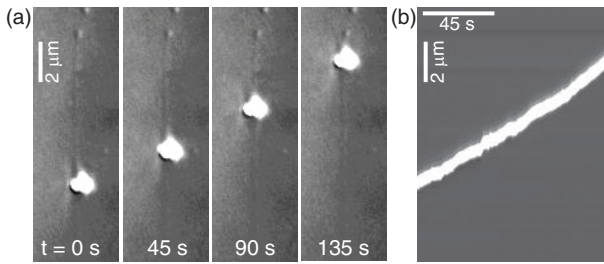


Figure 7.7: *DIC movie of Kip3 functionalized microsphere.* (a) DIC time-lapse images of a Kip3 functionalized microsphere moving along a microtubule. (b) Kymograph of the DIC movie along the microtubules. The microsphere moved with a velocity of 44 nm/s.

margins, these speeds were consistent with the TIRF measurements [107, 135, 143] and confirmed the functionality of the motor when attached to a microsphere.

7.5. Single-molecule conditions

Which kinesin concentration should we choose that we have at least 98% confidence of observing a single molecule? Single-molecule conditions were obtained according to a statistical analysis of the interaction probability of motor-coated microspheres with immobilized microtubules [119]. This probability as a function of the motor-to-microsphere ratio follows Poisson statistics. Therefore, I sequentially reduced the concentration of motors incubated with the microsphere and measured the fraction of microspheres that showed motility (Fig. 7.8). The probability $P_\lambda(k)$ that a number of k motors pulling the microsphere is

$$P_\lambda(k) = \frac{\lambda^k}{k!} e^{-\lambda}, \quad (7.1)$$

where λ is the mean number of pulling motors. This number is proportional to the number of motors per microsphere n ($\lambda = \Gamma n$, with proportional factor Γ). The probability of one pulling motor is $P_\lambda = \lambda e^{-\lambda}$. The probability of a microsphere being pulled by at least one motor in dependence of the motor/microsphere ratio n is

$$P_{\geq 1}(n) = 1 - e^{-\Gamma n}, \quad (7.2)$$

and the probability for at least two motors is

$$P_{\geq 2}(n) = 1 - e^{-\Gamma n} - \Gamma n e^{-\Gamma n}. \quad (7.3)$$

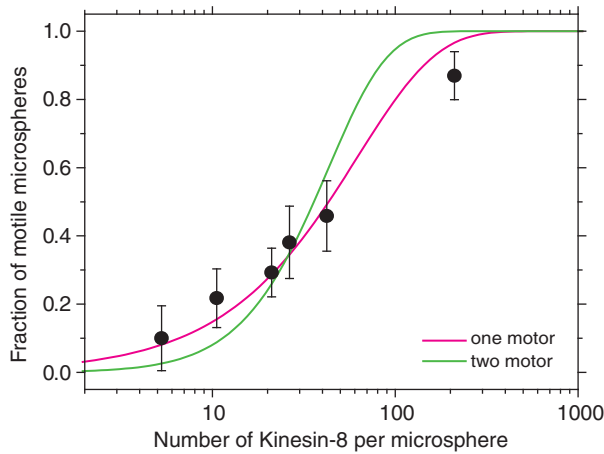


Figure 7.8: *Single molecule conditions determined with Poisson statistics.* Fraction of motile microspheres as function of number of Kip3 per microsphere. The experimental data (number of tested microspheres per concentration ≥ 21) are fitted with Eq. (7.2) for at least one functional molecule per microsphere (—) and Eq. (7.3) for two or more molecules per microsphere (—).

At the kinesin to microsphere ratio of $\Gamma n = 0.3$, the probability that at least one motor is pulling is $P_{\geq 1} = 0.26$, the probability for at least two motors is $P_{\geq 2} = 0.04$. The effective probability that these motors could bind at the same time to a microtubule is reduced by a geometric factor: $P_{\geq 2}^{\text{eff}} = P_{\geq 2} \cdot P_{\text{geom}}$. For example, if two motors with a length of $L \approx 60$ nm (Kip3 length plus PEG linker) are bound opposite to each other on the microsphere with a diameter $d = 590$ nm, simultaneous interaction with one microtubule is impossible. The geometric factor for two motors can be calculated by $2L/d(2 - 2L/d) \approx 0.4$. This reduces the probability that more than one motor interacts with a microtubule from 0.04 to about 2%. Thus, I had single-molecule conditions with 98% confidence if not more than 25% of the spheres show motility.

7.6. Force feedback

The study of the mechanics of single kinesin-8 proteins including the detection of single steps and the motor response to constant forces required an optimized setup with respect to the signal-to-noise ratio. Furthermore, to apply a constant force I used a force feedback. For the feedback, I used a proportional-integral-derivative controller (PID) in two dimensions. In the force-clamp mode, the trapping laser was moved with two piezo-mirrors (see Section 2.3.1) relative to the sample with an update rate of 200 Hz. This movement maintained a constant offset Δx between the microsphere and the trap center (see Fig. 8.1, Section 8.1), resulting in a constant force $F_{\text{trap}} = \kappa \Delta x$. The offset was set and held constant using a software developed in Labview.

The force feedback was tested and optimized by simulating microsphere steps. Therefore, I immobilized $0.59 \mu\text{m}$ PS microspheres on an easy-cleaned glass surface, by screening the repulsive electrostatic forces with 1 M KCL (Fig. 7.9 a) [152]. In an additional experiment, I bound kinesin-8-coated microsphere to surface immobilized microtubules by AMP-PNP (adenosin 5'-(β,γ -imido)triphosphate, 1 mM, Jena Bioscience), a non-hydrolyzable ATP analog (Fig. 7.9 b). I simulated 10 nm diffusive steps of the microsphere by moving the piezo stage. I followed the microsphere movement with the optical tweezers in zero-force-clamp mode with an update rate of 200 Hz. The microsphere movement was reflected in the monitored laser movement plus the measured displacement of the microsphere relative to the laser (Fig. 7.9). For both immobilizations, I could clearly resolve the 10 nm steps. The spatial resolution of the kinesin-coated

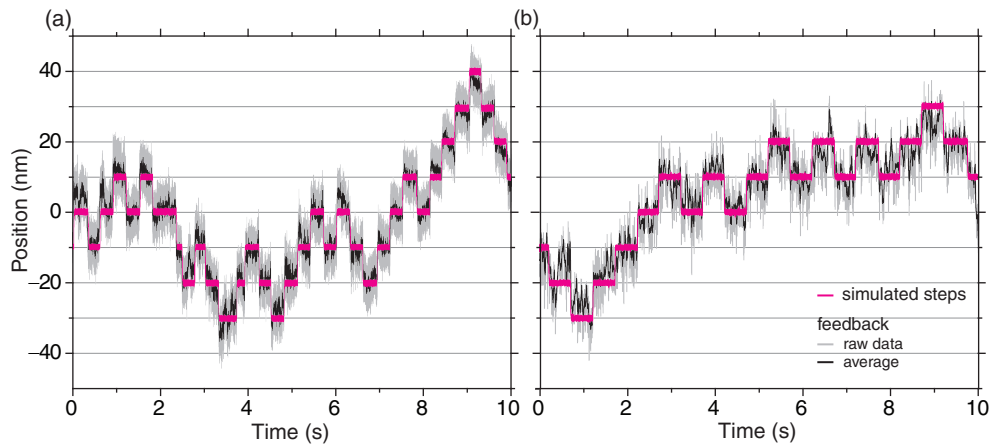


Figure 7.9.: *Performance of the force feedback.* The flow cell with the microspheres was moved by the piezo stage with 10 nm diffusive steps (—). (a) The microsphere was immobilized directly on the surface. (b) The kinesin-8-functionalized microsphere was immobilized on a microtubule with AMPPNP. The force feedback moved the laser via two piezo mirrors to follow the microsphere position (— raw data, —, box-car filtered to 400 Hz) with an offset of 0.5 pN. The trap stiffness was 0.034 pN/nm.

microsphere was worse, due to the flexible PEG linker between the kinesin and the microsphere. The resolution can be increased by stretching the PEG linker with a higher load force.

Chapter 8

Kinesin-8 is a low-force motor protein with a weakly-bound slip state

*Different kinesin-8 family members have been shown in vivo to control the length of microtubules by interacting with their plus ends. To reach these ends, the motors have to be able to take many steps without dissociating from the microtubule. However, the underlying mechanism for this high processivity and how stepping is affected by force is unclear. Here, I tracked the motion of yeast (*Kip3*) and human (*Kif18A*) kinesin-8s with high precision under varying loads using optical tweezers. Surprisingly, both kinesin-8 motors stalled at loads of only 1 pN, much less than the stall forces of other kinesins. Furthermore, the motors displayed a force-induced stick-slip motion: the motors frequently slipped, recovered from this state, and then resumed normal stepping motility without detachment from the microtubule. The low forces are consistent with kinesin-8s being regulators of microtubule dynamics rather than cargo transporters. The slip state, in which the motor remains weakly-bound to the microtubule, may be an adaptation for high processivity: in the absence of force, such a slip state corresponds to a diffusive state which would facilitate the rebinding of the motor and resumption of stepping.*

8.1. Kinesin-8 is a slow and weak motor protein

To determine how the translocation of the kinesin-8 motors was affected by load, I tracked the position of single-motor-powered microspheres as a function of time while applying controlled, constant loads with the optical tweezers operated in a force-clamp mode (Fig. 8.1). Due to the high processivity of kinesin-8, I could apply a large range of both hindering and assisting forces during a *single* run of a *single* molecule (Fig. 8.2 a). Overall, I analyzed the motion of 26 (11) different single *Kip3* (*Kif18A*) molecules. For all *Kip3* (*Kif18A*) molecules, I applied different forces ranging from -5 to $+5$ pN (-2.5 to $+2.5$ pN). For each force, I used on average 30 independent traces excluding slip events (see Section 8.3) and fitted lines to intervals of 1 s. I averaged the resulting slopes and plotted the corresponding mean velocity.

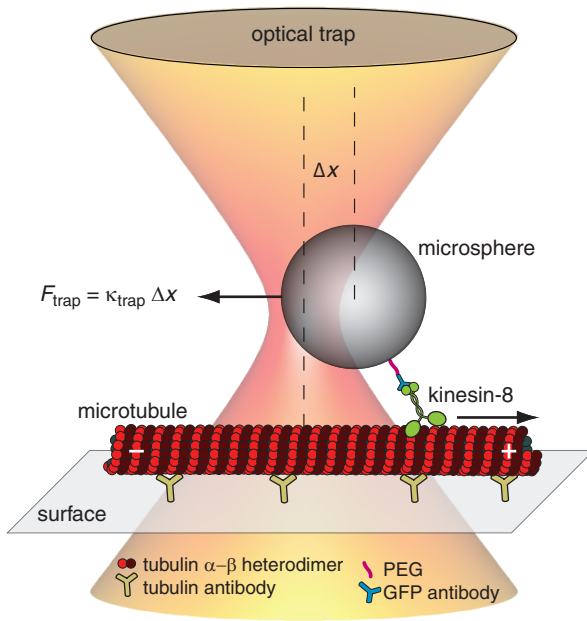


Figure 8.1: Schematic of the optical tweezers experiment. (not to scale). A kinesin-8-coated microsphere is trapped by a focused laser near an immobilized microtubule. The motor moves on the microtubule and displaces the microsphere from the trap center by Δx . In the force-clamp mode, the laser follows the protein movement with a constant force F_{trap} .

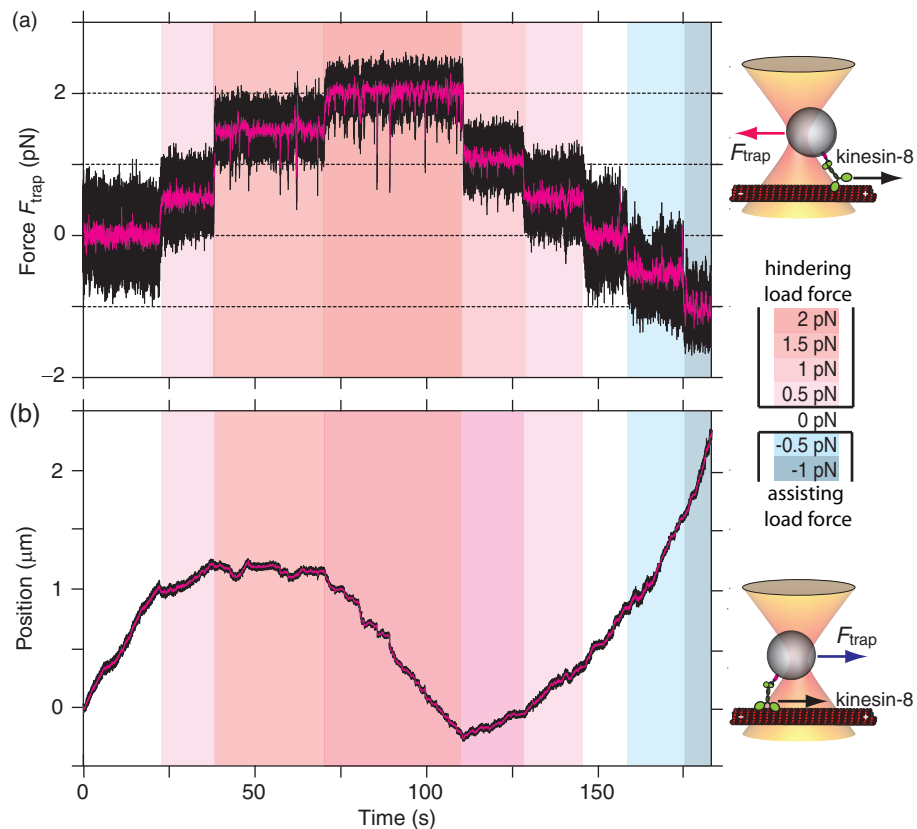


Figure 8.2: Exemplary trace of a single *Kip3* motor. Left: (a) Time trace of the load force acting on the microsphere. (b) Time trace of the corresponding position. The data — (—) was box-car filter to 2 kHz (100 Hz). Right: Hindering or assisting load forces, defined as positive (■), are directed toward the microtubule minus end; assisting load forces (■), respectively, towards the microtubule plus end.

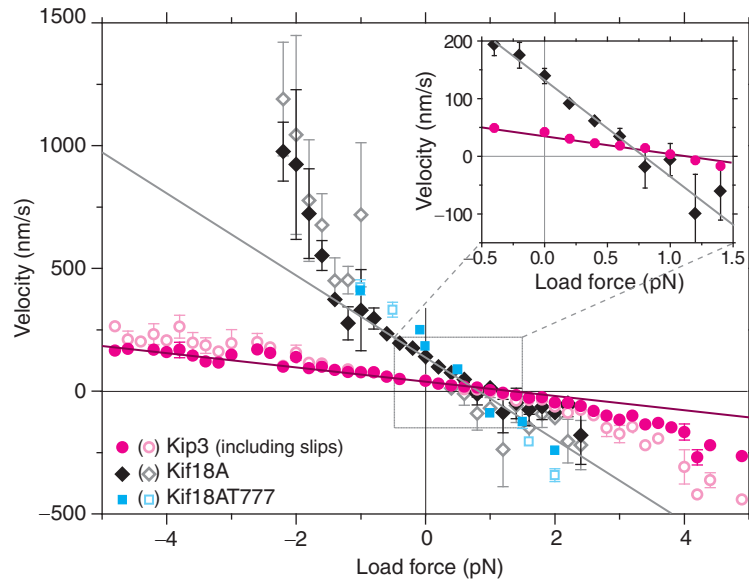


Figure 8.3.: *Force-velocity relation.* Velocity of Kip3 (●), full-length Kif18A (◆), and a truncated Kif18AT777 (■) as a function of force: positive is a hindering and negative is an assisting load force (mean±SEM). Open symbols (○, ◇, □) include slip events resulting in up to 2.5× faster velocities. Inset: Zoom of the positive quadrant showing the zero-force velocity and stall force. Solid lines (—, —) are linear fits to the data shown in the inset.

I defined a hindering load force to be positive (red shaded) and an assisting force negative (blue shaded). The exemplary trace of position versus time (Fig. 8.2 b) shows that already for small hindering load forces of $\lesssim 1$ pN, the microsphere slowed down and eventually stalled. For higher loads, the motor moved backwards. For assisting loads, the movement was accelerated.

To quantify the motor movement, I determined the average speed for the different forces by linear regressions of the position traces (Fig. 8.3). I observed a zero-force speed of 42 ± 4 nm/s (130 ± 42 nm/s) for Kip3 (Kif18A) (inset Fig. 8.3; mean±SEM if not noted otherwise). These speeds were consistent with the ones determined for motor-driven microspheres tracked with the optical trap turned off (see Section 7.3) or free motors tracked by TIRF measurements [107, 135, 143]. I measured a stall force, where the mean speed of the motor was zero, of 1.11 ± 0.07 pN (0.76 ± 0.06 pN) for Kip3 (Kif18A). While Kip3 had a nearly linear force-velocity relation over the measured force range, the Kif18A relation showed a non-linear acceleration for assisting forces. In comparison to conventional kinesin-1 [11], both kinesin-8s were much slower and weaker.

8.2. Kinesin-8 moves in 8 nm steps

During the regular mechano-chemical cycle, kinesin-8 took ≈ 8 nm steps. A zoom into the position traces for 1.5 pN assisting force (Fig. 8.4 a) revealed individual discrete steps with a size consistent with the 8.2 nm-spacing between tubulin dimers [100] (Fig. 8.4 b). The dwell time distribution of the steps was best fitted by a single-exponential with a relaxation time of 0.10 ± 0.02 s (reduced χ^2 -value: 1.2) (Fig. 8.4 c). The reduced χ^2 -value for a double-exponential fit was 1.3. The single-exponentially distribution of the dwell times between steps indicate a single, rate-limiting step. Thus, stepping was as expected

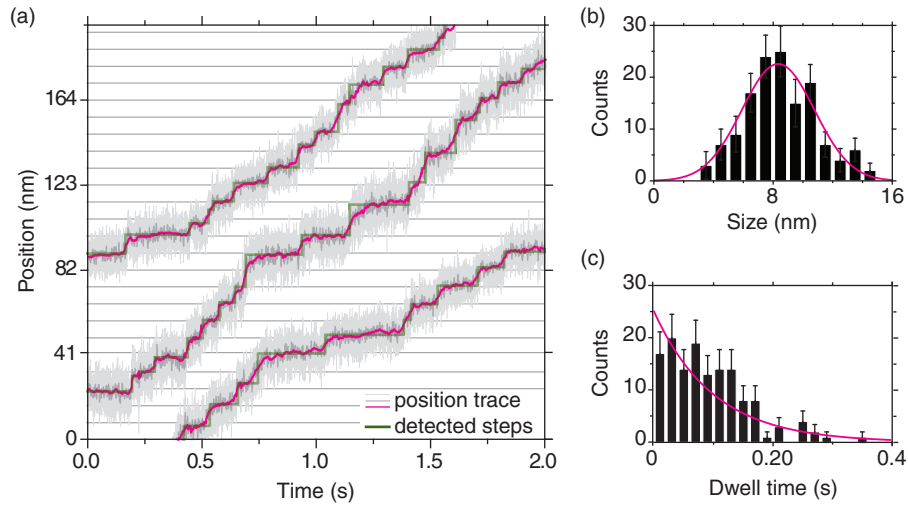


Figure 8.4.: *Exemplary forwards steps.* Zoom of exemplary position traces for Kip3 recorded with -1.5 pN assisting load force (— raw data, — [—]: box-car filtered to 400 Hz [100 Hz], — step detector [143]). The grid has a 8.2 nm periodicity. (b) Histogram of step sizes with a mean of 8.3 ± 0.2 nm (SE, $N = 139$) based on a Gaussian fit (—). (c) Dwell time distribution of steps fitted by single-exponential with a relaxation time of 0.10 ± 0.02 s (reduced χ^2 -value: 1.2).

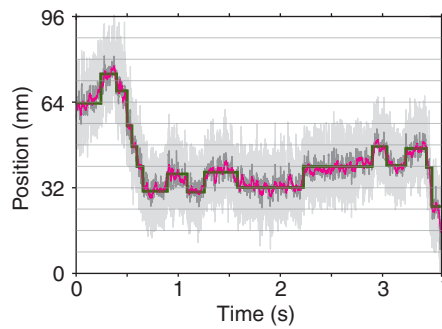


Figure 8.5: *Forward and backward steps at stall force.* Zoom of exemplary position traces for Kip3 recorded with 1 pN hindering load (— raw data; — [—] box-car filtered to 400 Hz [100 Hz]; — step detector [143]). The trace shows forward and backwards steps. The grid has a 8 nm periodicity.

for a kinesin [120]. Furthermore, under hindering load force kinesin-8 made backward steps. Figure 8.5 shows ≈ 8 nm forward and backward steps under 1 pN hindering load force. Due to the poor signal-to-noise ratio at 0 pN load force, I could not observe steps at 0 pN load force.

To objectively determine the step size, without using a step-finding algorithm, I performed a fluctuation analysis. The fluctuation analysis is based on a velocity power spectrum method developed by Charvin *et al.* [153]. The principle behind the analysis is that the random occurrence of steps contributes most to the power spectrum of the velocity at low frequencies. For a Poisson stepper moving consistently in one direction with a single rate-limiting step, the spectrum is expected to have a low-frequency asymptote. The amplitude of this asymptote, p , is related to the step size δ and velocity v according to $p = 2v\delta$. Such a plateau at low frequencies indicates that the microsphere moved in a stepwise manner (Fig. 8.5 b). For traces measured near the stall force, I expected an overestimated step size, because of the mixture of forward and backward steps (Fig. 8.6 a) [154]. An analysis of all Kip3 position traces—excluding traces recorded at 0.5-1.5 pN hindering load forces—gave a step size of 8.1 ± 0.2 nm (SEM, $N = 62$). One example fluctuation power spectrum for 0 pN load force is given in Fig. 8.6 a.

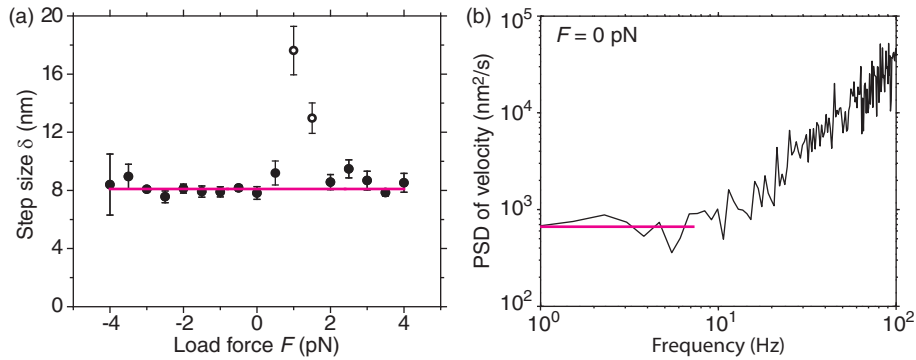


Figure 8.6.: *Fluctuation analysis.* (a) Step size δ (●) as a function of load force. Near the stall force the step size was overestimated due to backward steps. Step sizes determined at 1.0 – 1.5 pN (○) were excluded from the constant fit (—). (b) Example fluctuation analysis (velocity power spectral density) of a position traces for Kip3 recorded with 0 pN load force. The plateau $p = 2v\delta$ at low frequencies indicates that the microsphere moved in a stepwise manner. With the average plateau value (—) and the velocity ($v=40$ nm/s), the step size δ could be calculated to 7.9 ± 0.5 nm (mean $\pm \delta / \sqrt{N_{\text{fit points}} N_{\text{spectra}}}$) for this example.

8.3. Kinesin-8 slips on microtubules under load

Close inspection of the time-traces revealed that the motor frequently slipped along the microtubule in the direction of the applied force (Fig. 8.2, Fig. 8.7). During a slip, the microsphere moved with a fast and almost constant velocity. Since these events were faster than the response time of the force-clamp feedback, I could not automatically detect slip events when the amplitude of force spikes exceeded a threshold of 4 (≈ 6) standard deviations of the unfiltered (box-car filtered to 400 Hz) force noise. (spikes in Fig. 8.2). For each slip event, I determined the average force F_{mean} , the duration τ_s , and distance x_s that the motor slipped as illustrated by the green lines in Fig. 8.7.

Independent of force, the slip distance was a multiple of ≈ 8 nm (Fig. 8.8 a), though I could not resolve individual 8-nm steps during a slip. After each slip, the motor resumed its regular mechano-chemical cycle with ≈ 8 nm steps (Fig. 8.4, Fig. 8.7). To gain further insight into the slip state and how it may be related to the regular mechano-chemical cycle, I analyzed how the slip parameters—slip distance x_s , time τ_s , frequency f_s , and slip velocity v depended on force. The slip distance x_s increased with hindering or assisting load forces (Fig. 8.8 b). However, the slip time τ_s remained constant (Fig. 8.8 c); it was *independent* of force. Interestingly, for Kip3, the slip time significantly differed depending on the pulling direction (magenta open vs. closed circles in Fig. 8.8 c, d). The number of detected slip events per second f_s depended linearly on force with a threshold force of ≈ 0.6 pN (Fig. 8.8 e). Furthermore, based on the slip time and distance, the mean slip speed $v_s = x_s / \tau_s$ as a function of the mean force F_{mean} (Fig. 8.8 f) revealed very fast movements of the microsphere of up to $9.6 \mu\text{m/s}$ ($4.1 \mu\text{m/s}$) for Kip3 (Kif18A). One explanation for the slips would be a short detachment of the motor from the microtubule. During such a detachment, the optical tweezers would pull the microsphere towards the trap center. How long it would take for the microsphere to move the observed slip distances depends on the applied force, the displacement from the trap center, its stiffness, and the drag coefficient of the microsphere. It is given by $\tau_{\text{trap}} = -(\gamma_0 / \kappa) \ln(1 - \kappa x_s / F) < 0.6$ ms where γ_0 is the surface-distance dependent hydrodynamic drag coefficient of the microsphere [18]. For our parameters, this relax-

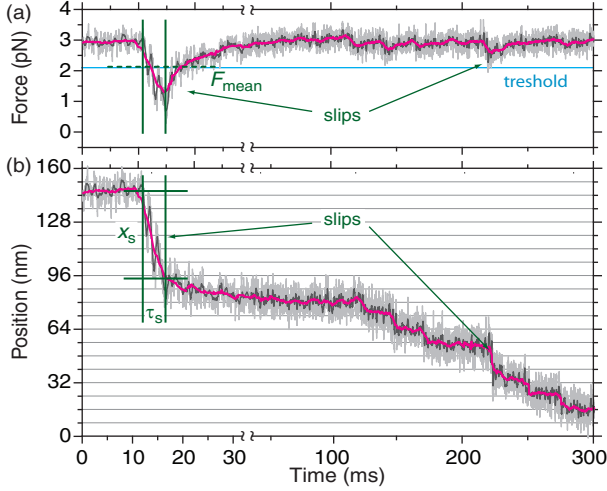


Figure 8.7: Exemplary slip events. Exemplary slip events and backward steps of a Kip3 motor under a 3 pN load force. (a) Time trace of force (— raw data; — [—] box-car filtered to 400 Hz [100 Hz]). The start and end of the large slip event are marked with green lines. The dashed green line shows the mean force F_{mean} during that slip. The threshold force for detecting slips in the raw data is marked with a blue horizontal line. (b) Time trace of microsphere position. I determined the slip time τ_s and distance x_s based on the rise time of the force spike. After a slip, kinesin-8 made regular 8 nm (here, backward) steps.

ation time in the trap τ_{trap} was much faster compared to all slip times τ_s (green line, Fig. 8.8 c). Correspondingly, the relaxation speed x_s/τ_{trap} of a free microsphere would be at least $60 \mu\text{m/s}$ ($30 \mu\text{m/s}$) in case of Kip3 (Kif18A)—much faster than the observed values (Fig. 8.8 f). Therefore, the motors must have remained in contact with the microtubule. Moreover, during slips of control measurements, the motors also sustained additional sideways loads without microtubule detachment [155]. Taken together, these results indicate that the motor switched to a different, weakly-bound, state. Biased motor movement in a weakly-bound state implies friction between the motor and its track [143]. Interestingly, I also observed slipping for a truncated Kif18AT777 motor (blue squares in Fig. 8.8), which lacked the microtubule-binding tail domain. Thus, the processivity-enhancing tail domain is not the origin for slipping.

To quantitatively compare the friction during a slip with the one measured in the presence of ADP [143], we developed an analytical stepping model. Based on our previous measurements [143], we assumed that in the slip state both kinesin heads form weakly-bound contacts to the microtubule at discrete binding sites spaced a distance $\delta \approx 8 \text{ nm}$ apart. The slip speed is then given by

$$|v_s| = \left| \frac{x_s}{\tau_s} \right| = \delta |k_+ - k_-| + v_{\text{offset}}^\pm = |v_+ - v_-| + v_{\text{offset}}^\pm \quad (8.1)$$

where k_\pm are the effective forward and backward stepping rates. v_{offset}^\pm is an offset, which depends on the direction of slipping, and arises, in part, from our ability to resolve only the beginning and ending of the slip events (see below). The model assumes that the forward and backward slip speed v_\pm depend in an Arrhenius-type fashion on force

$$v_\pm = v_0 \exp \left[\pm \frac{F_{mean}(\frac{1}{2}\delta \pm \varepsilon)}{k_B T} \right]. \quad (8.2)$$

The zero-force velocity $v_0 = \delta k_0$ is determined by the step size and zero-force stepping rate k_0 . Here, we have assumed a single, rate-limiting barrier with an asymmetric position characterized by the parameter ε [143]. In this case, the sum of the distances to the transition state in the forward and backward direction is equal the binding site spacing δ . For $F_{mean}(\frac{1}{2}\delta \pm \varepsilon) \ll k_B T$, a linearized force-velocity relation $|F_{mean}| = \gamma(|v_s| - v_{\text{offset}}^\pm)$ results in the frictional drag coefficient $\gamma = (k_B T)/(\delta v_0)$.

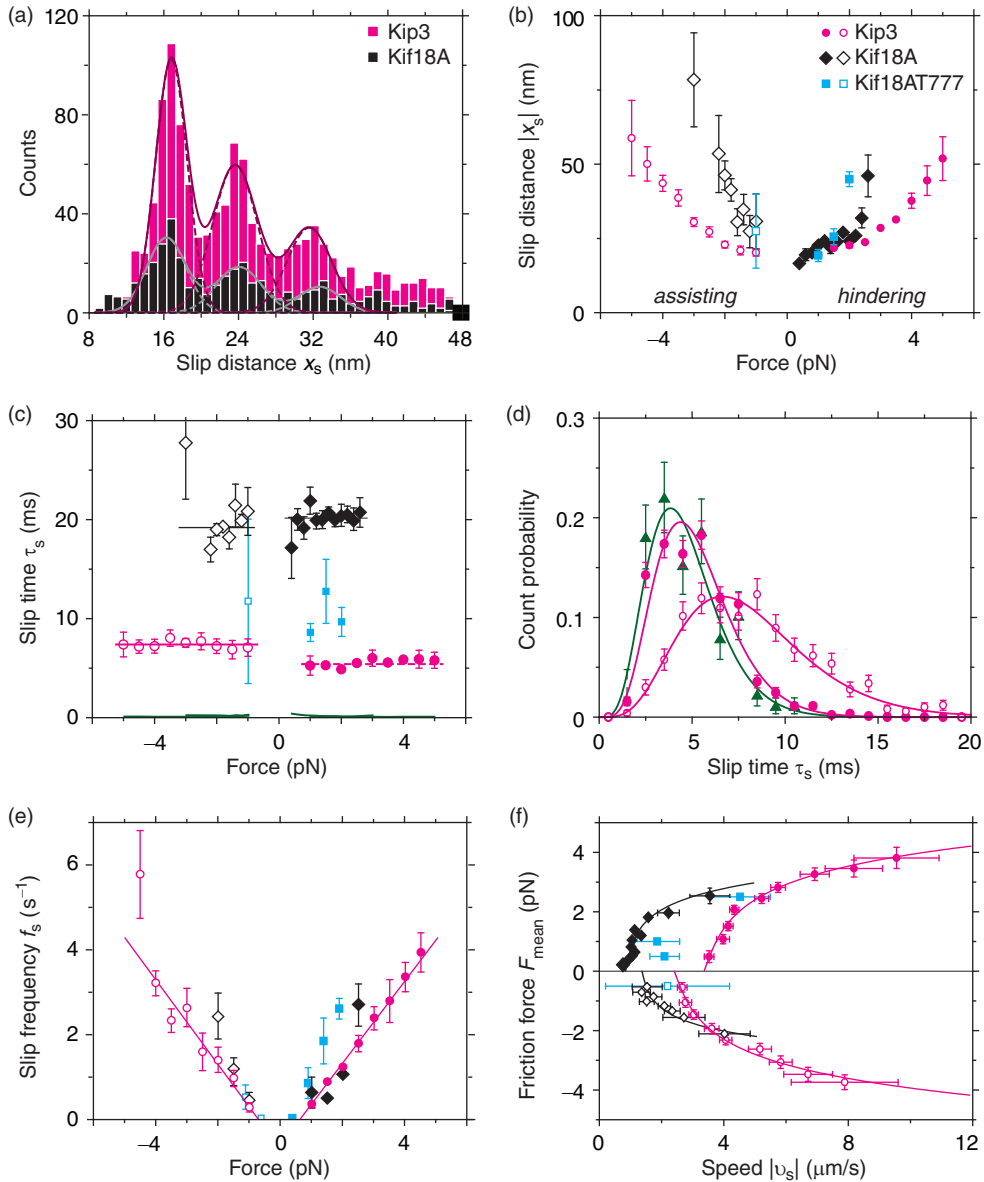
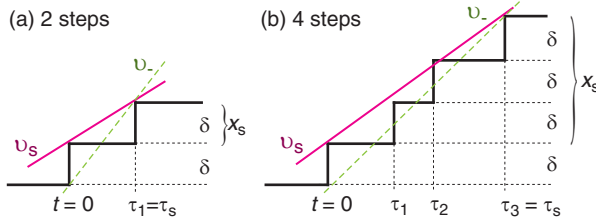


Figure 8.8.: *Slip parameters.* (a) Histogram of slip distance x_s of all observed slip events (Kip3 (■): 1402 events, Kif18A (■): 475 events). The mean of the Gaussian fits (—, —) were for Kip3: 16.5 ± 0.2 , 23.6 ± 0.3 , and 31.9 ± 0.2 nm and for Kif18A: 16.0 ± 0.3 , 24.1 ± 0.2 , and 32.4 ± 0.6 nm corresponding to multiples of ≈ 8 nm. Slips of 8 nm cannot be distinguished from 8 nm steps and could, therefore, not be detected. (b) Slip distance x_s , (c) slip time τ_s and (e) number of slips per seconds f_s as a function of force at slip start (Kip3 ●; full-length Kif18A ◆; truncated Kif18AT777 ■; open symbols (○, ◇, □) correspond to assisting and solid symbols to load force). (c) For Kif18A, the mean slip time was 20.1 ± 0.3 ms (19.2 ± 0.4 ms) and, for Kip3, 5.4 ± 0.1 ms (7.4 ± 0.1 ms) for hindering (assisting) load forces. The relaxation time in the trap τ_{trap} is plotted as a faint green line. (d) Histograms for Kip3 slip times. Load (●) and assisting (○) forces were best-fit by a gamma distribution with a shape parameter of 5.0 ± 0.6 and 4.2 ± 0.4 , respectively. Green triangles correspond to a subset of hindering-load slip events with distances of 16 ± 3 nm and shape parameter of 5.7 ± 0.8 . (f) Mean friction force as a function of slip speed.

A fit of Eq. (8.1) to the Kip3 (Kif18A) force-velocity data (Fig. 8.8f) resulted in the parameters listed in Table 8.1. The step sizes agreed within two standard errors with the expected ≈ 8 nm step size. The 8-nm slip distance is consistent with the binding

Table 8.1.: Parameters of Eq. (8.1). Parameters of Eq. (8.1) fitted to the data of Fig. 8.8 f (Mean \pm SEM)

	δ (nm)	v_0 (nm/s)	γ (μ Ns/m)	ε (nm)	v_{offset}^+ (μ m/s)	v_{offset}^- (μ m/s)
Kip3	7.5 ± 0.7	185 ± 53	3.0 ± 0.9	0.1 ± 0.1	3.5 ± 0.1	2.5 ± 0.1
Kif18A	13 ± 3	64 ± 39	4.9 ± 3.2	0.9 ± 0.3	0.9 ± 0.1	1.4 ± 0.2

**Figure 8.9:** Schematic of minimal slip. In any slip event [(a) 'two steps', (b) 'four steps'] there is always one more spatial step compared to the number of dwell times. The difference between v_s (—) and v_- (---) defines the offset velocity v_{offset}^\pm .

at the canonical motor-microtubule strong-binding sites [143] for which there is only one per tubulin dimer; the distance is not consistent with binding to the negatively-charged E-hooks [156] for which there is one binding site per tubulin monomer (i.e. every 4 nm). The extrapolated, effective zero-force stepping rates $k_0 = v_0/\delta$ were about 23 s^{-1} (8 s^{-1}) for Kip3 (Kif18A) assuming 8 nm steps. For both motors, the frictional drag coefficient was about $4\ \mu\text{Ns/m}$. For Kip3, this coefficient of the weakly-bound slip state was comparable (about $3\times$ higher) to the one measured in the presence of ADP but much smaller (at least $10\times$) compared to the nucleotide free state [143]. For Kif18A, the interaction potential may be slightly asymmetric, while for Kip3 the asymmetry parameter was not significantly different from zero. The velocity offset, v_{offset} from Fig. 8.8 c and Table 8.1 was for Kip3 $3.5\pm 0.1\ \mu\text{m/s}$ and $2.5\pm 0.1\ \mu\text{m/s}$ for hindering and assisting load forces, respectively ($0.9\pm 0.1\ \mu\text{m/s}$ and $1.4\pm 0.2\ \mu\text{m/s}$ for Kif18A). This corresponds to failing to detect events with less than two net steps in the direction of load: $(v_{\text{offset}}\tau_s)/\delta = 2.2\pm 0.2$, where we averaged over loading directions and motors. This value of the minimal number of steps per slip event is reasonable because (i) in any slip event there is always one more spatial step compared to the number of dwell times (see Fig. 8.9) and (ii) our spatial resolution to detect slip events was limited by the short duration and comparatively low load forces (Fig. 8.8 c). The latter point entails that I cannot resolve (back-) steps during a slip event and cannot distinguish an 8-nm slip from a normal 8-nm step. So, I miss slip events with, for example, one forward and one backward step. When this detection limitation was included, the model described the data very well.

8.4. Discussion

Our measurements show that kinesin-8 is a slow and weak motor protein. While other kinesins have been shown to be slow [157, 158], a stall force of $\approx 1\text{ pN}$ is much smaller compared to any other mechanically-characterized kinesin (kinesin-1: $5\text{--}6\text{ pN}$ [11], kinesin-2: $\approx 4\text{ pN}$ [159], (dimerized) kinesin-3: $\approx 6\text{ pN}$ [160], kinesin-5: typically 5 pN , occasionally up to 7 pN [157], kinesin-7: 6 pN [158]). This finding is not consistent with kinesin-8 being a transport motor because even small cytoplasmic obstructions are likely to stall the motor or switch it into a slip state.

The strong force-dependence of the kinesin-8s suggest that they operate by a Brownian ratchet—rather than a power stroke mechanism as defined in [161]. Approximating stall as a reduction in stepping speed to $1/e^2 = 13.5\%$ and assuming an exponential force dependence, results in a distance to the transition state of $x^\ddagger \approx 2k_B T / F_{\text{stall}} = 7.4$ nm (11 nm) for Kip3 (Kif18A). This distance x^\ddagger is close to or even larger than the stepping distance δ . In a potential-energy-landscape model, the motor-head thermally fluctuates around its initial state until it reaches the transition state. For both motors, it is close to the final state where the head is trapped by a chemical change during its mechano-chemical cycle: Thus, in contrast to other kinesins such as kinesin-1, kinesin-8 stepping follows a Brownian ratchet mechanism [161].

We discovered another unique feature of kinesin-8s: during ATP-driven motion it slips on the microtubule without detaching. To gain insight into the slip state, I analyzed the friction between the motor and the microtubule during slips. Since the ATP state is presumably a strongly-bound state, we attribute the increased frictional drag coefficient, intermediate between ADP and no nucleotide, to one head being in the ADP- P_i state. The other head must also be in a weakly-bound state. If ATP is hydrolyzed before ADP is dissociated from the other head [162], then one head is likely to be in the ADP- P_i and the other in the ADP state (Fig. 8.10). The different nucleotides in the heads may explain the directional asymmetry in the slip time: depending on whether the ADP- or ADP- P_i -bound head detaches first, the slip times may differ. The difference in slip times may also be due to the microtubule polarity or the motor's directionality. With both heads weakly-bound, the motor enters an off-pathway of its regular mechano-chemical cycle, in which the heads alternate between strongly and weakly-bound states (Fig. 8.10).

The motor slipped multiple steps per nucleotide. Since ATP-driven stepping is slow and ADP is nearly absent in solution, the multiple steps during the short-lived slip events (Fig. 8.8 a) are likely to proceed without exchange of the nucleotides, though it is possible that they are associated with the release of phosphate. This implies that the slip distance divided by the step size gives a direct measure for the number of steps that the motor can take per nucleotide in a weakly-bound state. This number was 3.5 ± 0.1 for load and 4.2 ± 0.1 for assisting forces. Therefore, during previous diffusion and friction measurements [143], ADP was likely exchanged every few steps—not every step and not just once per diffusive or sliding event.

Termination of a slip event or sticking occurs when one motor head releases its nucleotide. Since the slip time was independent of force (Fig. 8.8 c), this nucleotide release most likely occurred at a free, non-load-bearing head while it was taking the next step. Interestingly, though the slip time was independent of force, the distribution of slip times was not a simple exponential (Fig. 8.8 d). The distribution was best-fit by a gamma distribution with a shape parameter of 4–5 implying this many independent steps during a slip event. Since this number is close to the average number of steps per slip event, the shape of the gamma distribution may be due to the number of physical steps the motor takes during a slip. However, the slip time distribution (green triangles in Fig. 8.8 d) for the short, two-step slips (16 ± 3 nm in Fig. 8.8 a) had a shape parameter of 5.7 ± 0.8 inconsistent with merely two physical steps. Thus, the gamma distribution seems to stem from multiple biochemical steps during a slip.

A slip state at zero force should be equivalent to a diffusive state. While I did not observe such a state under zero force (in part due to our detection limit; Fig. 8.8 e), it may

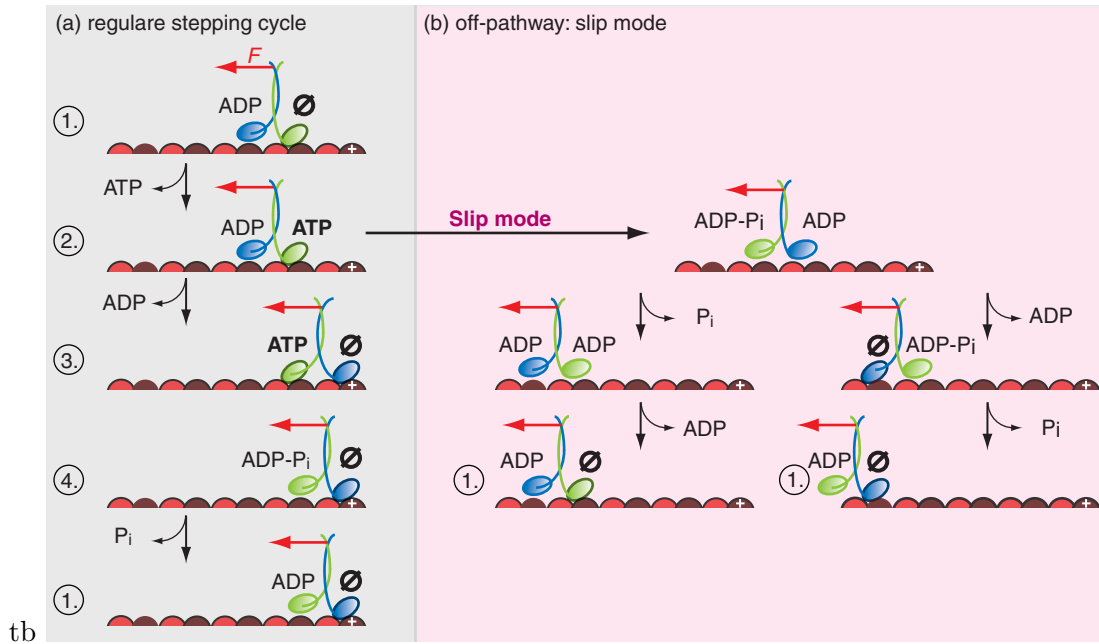


Figure 8.10.: *Schematic of mechano-chemical cycle.* (a) Schematic of regular mechano-chemical cycle (1.-4.). One 8 nm step is associated with one cycle of ATP hydrolysis. During processive movement, at least one head is tightly-bound (**ATP**, \emptyset) to the microtubule. (b) Possible off-pathway during the slip mode. If ATP is hydrolyzed before ADP is dissociated from the other head, then one head is likely to be in the ADP- P_i and the other in the ADP state. After the release of the P_i and/or one ADP, one motor domain is in the nucleotide free state (1.) and binds again tightly to the microtubule. In this manner, the motor recovers from the weakly-bound slip state and resumes normal stepping.

be present under different, physiological conditions. Furthermore, the tail microtubule binding site may enable the motor to bridge microtubules. Then, loading and slip events are possible. For kinesin-1, such a diffusive state may correspond to the one where the motor detaches from the microtubule. For kinesin-8, this diffusive or slip state may have been strengthened such that it acts as a safety leash for kinesin-8. This leash, in addition to the tail-microtubule-binding domain, may enable the very high processivity of the motor to regulate the dynamics of microtubules at their ends.

Chapter 9

Outlook

In summary, with the improvements in performance of optical tweezers and their probes new experiments in physics and biology are possible. In this chapter, I want to give a brief outlook of the various aspects of my work.

Optical tweezers are often approximated as a Hookean spring, where the force is linearly proportional to the displacement. This is only valid near the trap center. For large microsphere-trap displacements the linear approximation breaks down. Our measurements and calculations of the complete force field allowed us a detailed validation of the force-displacement relation. We found that an optical trap with back-focal-plane detection is foremost a sensor of force and not of position. That means, that the force scales linearly with the detected volt-signal, but not with the actual displacement. Recent work showed that optimized back-focal-plane detection can directly measure forces due to momentum conversation [163]. Thus, the full force range and therefore higher forces could be used, if the displacement is not important to know. For example, for $2\ \mu\text{m}$ PS microsphere only 35 % of the maximal force is in the linear range (see Fig. 3.3 and Fig. 3.4).

Furthermore in this thesis, we showed that we can design photonicly-structured probes with an optimized trap efficiency. We started with $1\ \mu\text{m}$ titania core-shell particles. For this size, we achieved the highest trap efficiency and were able to measure force of more than one nanonewton. In principle, titania is bio-compatible, but for most biological protocols carboxylated microsphere are used. Therefore, the next step should be the functionalization of the titania surface. A possible problem that could occur during the functionalization is that amorphous titania is a porous structure. For example, the fluorescence dye was small enough to diffuse into the pores. This problem could be solved by a mixed titania-silica sintered shell instead of the amorphous shell. The correct mixture of silica ($n = 1.45$) and anatase titania ($n = 2.3$) should have the same refractive index like the amorphous titania ($n = 1.75$) [72]. Another solution could be a thin coating of silica or PS. For many experiments, smaller or bigger microspheres are the preferred choice. Unfortunately, the trap stiffness of PS and silica depends strongly on the size and decrease dramatically for microspheres smaller or bigger than 900 nm. The titania core-shell particles could also be optimized for smaller or bigger particles. For example, as predict from the theory (see Fig. 4.1) 500 nm microsphere have a $1.6\times$ higher trap stiffness than PS microspheres of the same size. For bigger particles, the improvement is even more significant. For example, ideal coated titania core-shell particles with a

diameter of $2.3\ \mu\text{m}$ have a $7\times$ higher trap stiffness than PS microspheres of the same size. In general, the theory could be used to design photonically-structured probes of different materials with an optimized trap efficiency for any size, any wavelength and any optical tweezers setup.

Furthermore, the high trap efficiency of the anti-reflection coated titania microspheres in combination with significantly larger microspheres compared to the $1\ \mu\text{m}$, should enable us to measure resonances associated with the colored nature of thermal noise that drives Brownian motion. Typically an optical trap can be described by an overdamped harmonic oscillator. However, we observed indications of a resonance enhancement at high frequencies [77]. Goal of future projects are to characterize the colored noise of Brownian motion and the resonance effect in more detail. For this purpose, one should use bigger anti-reflection coated titania microspheres, while retaining a high trap efficiency. A resonant optical trap may be used as a novel tool and sensor probing anything that affects its resonance frequency.

In addition, I found a quantitative agreement between Mie theory calculations and experiments in different setups ($\lesssim 10\%$ deviation). If the toolbox parameters are optimized to the optical tweezers setup, the theory can be used for predictions, like the trapping characteristics of core-shell particles. Furthermore, the quantitative agreement implies that a force calibration is not necessary anymore, if the achieved accuracy of $\approx 10\%$ is sufficient.

Last but not least, we found that kinesin-8 is a low-force motor protein with a weakly-bound slip state. The low-force is consistent with kinesin-8 not being a transport motor. The unique feature of the kinesin-8 class to slip on microtubules without detaching, in addition to the tail-microtubule-binding domain, may enable its very high processivity. Kinesin-8 regulates the dynamics of microtubule by interacting with the plus-end. So, reaching the end of the microtubule is very important for this motor. *In vivo*, several motors and microtubule-associated proteins compete for binding to microtubules. Therefore, the weakly-bound slip state could act as a safety leash to prevent detaching from the microtubule in the case of obstacles. Furthermore, it is interesting to understand the mechanics of the depolymerization process. So far, it was observed that a single Kip3 stays up to 90 s at the end of the microtubule [107]. In this time the protein did not fall off, but randomly stepped forward and backward [142]. The time decreased significantly when a second Kip3 molecule arrived at the microtubule end [109]. This suggested that a second Kip3 has to arrive to bump the end-bound Kip3 molecule together with the bound end-tubulin dimer off the microtubule. As a consequence of this cooperative depolymerization model, one Kip3 molecule should leave the microtubule end with one tubulin dimer. Varga *et al.* [109] determined the ratio of Kip3 molecules releasing the microtubule to severed tubulin dimers to be ≤ 2 . The bump off mechanism cannot be proofed with single-molecule fluorescence tracking due to the lack of the positional resolution to visualize the end activity of single Kip3 molecules. We could use our setup to follow a single Kip3 during its processive run to the microtubule plus end with high precision. Using the force feedback, we could apply different forces to a single Kip3 molecule attached to a microsphere. If the time, while the Kip3 stays at the end, changed with applied force we could determine the Kip3 microtubule end binding strength. Another possible experiment would be the addition of free Kip3 molecules. Based on the bump off model, we expect a reduction in end residence time. The analysis of the measurements will be complicated, but could prove the model.

Finally, with this thesis new research possibilities are opened. First, we demonstrated the optimization of probes for optical tweezers. With the optimized probes many new experiments are now possible concerning optical tweezers. However, there is more potential for further developments. And last, we observed a unique slip-state, which is maybe an explanation for the high processivity. But how a single kinesin-8 depolymerizes a microtubule is still unknown. It will be an exciting task for the future to answer this question.

Appendix A

Protocols

A.1. Titania particles synthesis

Synthesis of anatase titania core

- add 0.46 w% titanium butoxid to ethylene glycol and mix for more than 4 h
- add 2.03 mM Tween 20 to analytical acetone
- add 10-17 ml 2.03 mM Tween 20 : acetone to 100 ml 0.46 w% titanium butoxid : ethylene glycol
- the amount of 2.03 mM Tween 20 : acetone determines the particles size; for \approx 500 nm anatase cores we used 14 ml
- let it react for 10-16 h, already after 10 min the solution becomes milky
- wash the amorphous titania particles $2\times$ in technical ethanol (20 min centrifuge with 5000 rpm), discard supernatant and resuspend the particles in ethanol by sonicating them)
- in the last washing step resuspend the particles in only 1 ml ethanol and put the solution in a 20 ml scintillation vial
- dry the particles in an oven (50-100 °C) till the ethanol is evaporated
- calcine the dried particles at 550 °C for 30-60 min
- resuspend the particles in 5 ml ethanol by sonicating them

Coating of anatase titania cores with amorphous titania

- use cooled (4 °C), analytical ethanol for the synthesis
- take 1.5-3 ml of the anatase particles (seeds) solution and fill up to 10 ml with the cooled analytical ethanol
- add 0.08 ml 0.1 M Lutensol ON 50 to the 10 ml ethanol-seed solution
- add 0.15-0.2 ml titanium butoxid to 10 ml ethanol
- mix the Lutensol-ethanol-seed solution with the titanium-butoxide-ethanol solution and sonicate the mixture for 30 min in ice water

- the amount of seeds and titanium butoxid determines the thickness of the coating and potential second nucleations
- wash the titania core-shell particles 2× in technical ethanol (20 min centrifuge with 5000 rpm), discard supernatant and resuspend the particles in ethanol by sonicating them)
- in the last washing step, resuspend the particles in only 1 ml ethanol and put the solution in a glass vial
- dry the particles in an oven (50-100 °C) till the ethanol is evaporated
- resuspend the core-shell particles in ethanol by sonicating them and store them at 4 °C

Reagent list

- Aceton, analytical (Merk)
- Ethylene glycol (Merk)
- Ethanol, technical (Sigma-Aldrich)
- Ethanol, analytical (J.K.Baker)
- Lutensol On 50 (BASF)
- Titanium butoxid (Sigma-Aldrich)
- Tween 20 (Sigma-Aldrich)

A.2. PS-PEG-anti-eGFP microspheres

Activation

- wash 25 μ l microspheres 2× in 1000 μ l MES, 13000 rpm, 3 min
- resuspend microspheres pellet in 250 μ l MES
- dissolve sulfo-NHS (1.62 mg) and EDC (1.42 mg) in MES
- first add sulfo-NHS then EDC
- incubate 15 min at 37 °C, 600 rpm
- wash 2× in 500 μ l MES, 13000 rpm, 3 min
- resuspend microsphere pellet in 250 μ l Borate buffer

PEG coupling

- dissolve PEG [1:9] in Borate buffer
- 3 kDa NH₂-PEG-COOH (2.6 mg) : 2 kDa NH₂-PEG-CH₃O (9.36 mg)
- add PEG to activated microspheres
- incubate 2 h at 37 °C, 600 rpm
- wash 5× in 500 μ l Borate buffer
- resuspend microsphere pellet in 250 μ l MES

Activation

- identical to first activation
- resuspend microsphere pellet in 250 μ l PBS

Antibody coupling

- add 10 μ l eGFP antibody to activated PEG microspheres
- incubate 2 h at 37 °C, 600 rpm
- wash 3 \times in PBS
- resuspend in 250 μ l PBS

Chemicals

- anti-eGFP (antibody facility, MPI-CBG, Dresden, Germany), 3 mg/ml in PBS
- Borate (sodium borate) buffer pH = 8.5, filtered
- EDC (1-ethyl-3-[3-dimethylaminopropyl]carbodiimide hydrochloride) MW 191.7 g/mol
- MES (2-(N-morpholino)ethanesulfonic acid) 50 mM, pH = 6.0, filtered
- PBS (phosphate buffered saline), pH = 7.0, filtered
- PS Microspheres: functionalized with carboxyl groups, Bangs Laboratories (PC03N/6487), diameter $d = 0.59 \mu\text{m}$
- Sulfo-NHS (N-hydroxysulfosuccinimide) MW 217.1 g/mol
- 3 kDa NH₂-PEG-COOH, 2 kDa NH₂-PEG-CH₃O, Rapp Polymere

A.3. Kinesin-8 stepping assay

Polymerization of GMPCPP-stabilized microtubules

- mix 'polymerization solution' (Tab. A.1), incubate on ice for 5 min, incubate at 37 °C for 2 h
- dilute the polymerized microtubules with 400 μ l BRB80
- spin down the microtubules (Beckman airfuge, 25 psi, 5 min)
- after spinning, aspirate the supernatant carefully and resuspend the pellet in 200 μ l BRB80

Flow cell for stepping assay

The flow cell was constructed with silanized coverslips. Parafilm was used to form channels. The flow cell was filled with the following reagents (Tab. A.2):

Table A.1.: Polymerization solution

Volume	Reagents	Stock concentration	Final concentration
2.5 μ l	RTU tubulin	4mg/ml	2 μ M
5 μ l	GMPCPP	10 mM	1 mM
0.5 μ l	MgCl ₂	100 mM	1 mM
42 μ l	BRB80		
50 μl	Final volume		

Table A.2.: Flow into the channel

	Volume	Reagents	Incubation time
1.	20 μ l	BRB80	10 min
2.	20 μ l	Anti-tub2.1 (2 mg/ml), 100 \times diluted in BRB80	10 min
3.	20 μ l	wash with BRB80	
4.	20 μ l	F-127 (1 w% in BRB80)	20 min
5.	3 \times 20 μ l	wash with BRB80	
6.	20 μ l	microtubules	15 min
7.	20 μ l	kinesin-8 reaction mix	

Kinesin-8 reaction mix

- mix 'motility buffer' (Tab. A.3)
- dilute kinesin-8 solution in 'motility buffer' ($\approx 1000 \times$ for single-molecule conditions)
- dilute (10 \times) Anti-eGFP-PEG-PS microspheres in 'motility buffer'
- add 2 μ l diluted Anti-eGFP-PEG-PS microspheres to 2 μ l diluted kinesin-8 solution
- mix 40 \times (≈ 30 s) carefully with pipet
- incubate 7 min at room temperature

Table A.3.: Motility buffer

Volume	Reagents	Stock concentration	Final concentration
448.75 μ l	BRB80		
18.75 μ l	KCL	3 M	112.5 mM
10 μ l	Casein	8 mg/ml	112.5 mM
5 μ l	D-glucose	2 M	20 mM
5 μ l	Glucose oxidase	2 mg/ml	0.02 mg/ml
5 μ l	Catalase	0.8 mg/ml	0.008 mg/ml
2.5 μ l	BME	100 %	0.5 Vol.%
5 μ l	ATP	≈ 100 mM	≈ 1 mM
500 μl	Final volume		

List of reagents

- anti-beta-tubulin SAP4G5 (Sigma T7816), diluted in BSA and stored at 4 °C several weeks
- BME: beta-mercaptoethanol (Sigma M3148), stored at 4 °C
- BRB80 buffer: 80 mM PIPES/KOH pH 6.9, 1 mM EGTA, 1 mM MgCl₂, stored at 4 °C
- BSA: bovine serum albumin (Sigma A3059)
- catalase (Sigma C9322), diluted in BRB80, snap frozen and stored at -20 °C
- EGTA: ethylene glycol tetaacetic acid (Sigma, E4378)
- F-127: pluronic F-127 (Sigma P2443) dissolved in BRB80 (1 w%), filtered and stored at 4 °C
- D-glucose (Sigma, G7016), diluted in BRB80, snap frozen and stored at -20 °C
- glucose oxidase (Sigma, G7016) diluted in BRB80, snap frozen and stored at -20 °C
- GMPCPP: Guanosin-5'-[(α , β)-methyleno]triphosphate (Jena Bioscience #NU-405), stored at -80 °C
- MgCl₂: magnesium chlorid (Merck 1.05833.0250)
- KOH: potassium hydroxide, 0.1 M (Sigma, P-5310)
- PIPES (Sigma P6757)
- RTU: 25 % rhodamin-labeled tubulin (purified from porcine brain), 4 mg/ml

Abbreviation

		τ	relaxation time
		τ_s	slip time
		τ_{trap}	relaxation time of microsphere in a trap
		$\tilde{x}(f)$	Fourier transform
		v	velocity
		v_s	slip velocity
ε	asymmetry parameter	v_{escape}	escape speed
β	displacement sensitivity	v_{offset}	offset velocity
Δx	relative displacement	c	speed of light
Δx_A	microsphere distance to the analyzing trap	D	diffusion coefficient
δ	step size	d	microsphere diameter
η	viscosity	d_{coat}	thickness of the coating
γ	drag coefficient	d_{core}	core diameter
γ_0	Stokes drag	f	frequency
κ	trap stiffness	f_ℓ	characteristic zero-crossing frequency
λ	wavelength	f_ν	characteristic viscous frequency
n_{coat}	refractive index of the coating	f_c	corner frequency
n_{core}	refractive index of the core	f_m	characteristic inertial frequency
n_{PS}	refractive index of PS	f_{stage}	stage frequency
n_{SiO_x}	refractive index of silica	f_s	frequency
$n_{\text{H}_2\text{O}}$	refractive index of water	k	stepping rate
$\rho_{\text{amorphous}}$	density of amorphous titania	k_B	Boltzmann constant
ρ_{anatase}	density of anatase titania	L	Kip3 length plus PEG linker
ρ_{titania}	density of the core-shell titania particles	l	surface distance to microsphere center
ρ_{water}	density of water	m	mass of the microsphere

M_2	beam quality factor	$F_{x \setminus y}$	force parallel (x) and perpendicular (y) to the trap polarization
P	laser power		
p	amplitude of asymptote on spectrum	ADP	adenosine diphosphate
P_0	plateau value	AFM	atomic force microscopy
$P_\ell(f)$	power spectral density for the microsphere position with Fourier transform	AMP-PNP	adenosin 5'-(β, γ -imido)-triphosphate
T	temperature	ATP	adenosine triphosphate
t	time	BSA	bovine serum albumin
x^\ddagger	transistion state	ddH ₂ O	demineralized water
x_{\max}^{linear}	linear displacement response	DIC	differential interference contrast
x_s	slip distance	EDC	1-Ethyl-3-[3-dimethylamino-propyl]carbodiimide hydrochloride
$x_{C,A}$	distance between strong calibration and analyzing trap	eGFP	enhanced green fluorescent protein
1D	one-dimensional	GDP	guanosine-5'-diphosphate
2D	two-dimensional	GMPCPP	guanosine-5' [α, β -methylene]-triphosphate
3D	three-dimensional	GTP	guanosine-5'-triphosphate
F_A	optical force of analyzing trap	Kif18A	6xHis-Kif18A-eGFP
F_C	optical force of strong calibration trap	Kif18AT777	6xHis-Kif18A777-eGFP, AA-1-777
F_{grad}	gradient force	Kip3	6xHis-Kip3-eGFP
F_{\max}	maximum optical force	MPI-CBG	Max Planck Institut of Cell Biology and Genetics, Dresden
F_{mean}	mean optical force	N	number of measurements
F_{scat}	scattering force	NA	numerical aperture
F_{thermal}	thermal force	Nd:YVO ₄	neodymium yttrium orthovanadate crystal
F_{trap}	trapping force		
F_{vis}	viscous force	PBS	phosphate buffered saline

PEG	polyethylene-glycol	SLS	static light scattering
PID	proportional-integral-derivative	Sulfo-NHS	N-hydroxysulfosuccinimide
PS	polystyrene	T-Matrix	transition matrix
PSD	position sensing device	TEM	transmission electron microscope
QPD	quadrant photo diode	TiO _x	titania core-shell
SDS-PAGE	sodium dodecyl sulfate polyacrylamide gel electrophoresis	TIRF	total internal reflection fluorescence microscope

List of Figures

2.1. Geometric optics description of gradient and scattering force	7
2.2. Schematic drawing of the MPI-CBG optical tweezers setup	10
2.3. Schematic drawing of the BIOTEC optical tweezers setup 'Aswad'	11
2.4. Schematic drawing of the BIOTEC optical tweezers setup 'Pinky'	13
2.5. Solid works drawing of the BIOTEC optical tweezers setup 'Pinky'	14
2.6. Schematic drawing of a flow cell	14
2.7. Calibrated power spectral density	16
3.1. Dual-optical trap setup	18
3.2. Optical force map	20
3.3. Force profile and trap stiffness	21
3.4. Force - detector signal relation	22
4.1. Mie theory calculations of trap stiffness for coated titania microsphere	27
4.2. Synthesis of titania core-shell particles	28
4.3. Fluorescence confocal image of titania core-shell particles	28
4.4. Transmission electron microscope pictures of titania core-shell particles	29
4.5. Static light scattering measurements	30
4.6. Digital holographic microscope measurements	31
4.7. Trap stiffness of anti-reflection coated titania	32
4.8. Trap stiffness as a function of laser power in the focus	32
4.9. Escape force measurements in oil	33
5.1. High-precision power spectral density of an anti-reflection-coated titania microsphere	40
5.2. High-precision power spectra as a function of surface distance	41
6.1. Schematic structure of a microtubule	47
6.2. Schematic structure of conventional kinesin	48
7.1. SDS-Page of purification of 6xHis-Kip3-eGFP	52
7.2. Bradford measurement	52
7.3. Schematic drawing of the kinesin-8 microsphere coupling	53

7.4. Schematic of carboxyl group activation and cross linking	53
7.5. Schematic of a stepping assay	54
7.6. Kymographs of Kip3 molecules	56
7.7. DIC movie of Kip3 functionalized microsphere	56
7.8. Single molecule conditions determined with Poisson statistics	57
7.9. Performance of the force feedback	58
8.1. Schematic of the optical tweezers experiment	60
8.2. Exemplary trace of a <i>single</i> Kip3 motor	60
8.3. Force-velocity relation	61
8.4. Exemplary forwards steps	62
8.5. Forward and backward steps at stall force	62
8.6. Fluctuation analysis	63
8.7. Exemplary slip events	64
8.8. Slip parameters	65
8.9. Schematic of a minimal slip	66
8.10. Schematic of mechano-chemical cycle	68

List of Tables

4.1. Size of different titania core-shell particle batches	31
5.1. Fit parameters of Eq. (5.1)	42
8.1. Parameters of Eq. (8.1)	66
A.1. Polymerization solution	76
A.2. Flow into the channel	76
A.3. Motility buffer	76

Contributions

Chapter 3 - Complete force field of an optical trap

The measurements were performed by Marcus Jahnel and Martin Behrndt (Grill group, MPI-CBG Dresden). The work was supervised by Erik Schäffer and Stephan W. Grill.

Chapter 4 - Nanonewton optical forces by trapping anti-reflection-coated titania microspheres

The synthesis of the particles, the TEM and the SLS measurements were done together with Ahmet F. Demirörs. The digital holographic microscopy measurements were done together with Peter D. J. van Oostrum. Alfons van Blaaderen advised the synthesis. Peter D. J. van Oostrum performed the theoretical calculations with spherical aberrations included. The work was supervised by Erik Schäffer.

Chapter 5 - Colored nature of the thermal noise of Brownian motion

Mohammed Mahamdeh contributed equally to the work. Erik Schäffer gave support on the theory.

Chapter 7 - Kinesin-8 assay

Marko Storch expressed and purified the Kif18A and supervised the expression and purification of Kip3. Volker Bormuth established the single Kip3 optical tweezers assay.

Chapter 8 - Kinesin-8 is a low-force motor protein with a weakly-bound slip state

Volker Bormuth first observed the slip state and stall force of Kip3. Jonathon Howard provided advice. The work was supervised by Erik Schäffer.

Publications related to this thesis

- ***Kinesin-8 is a low-force motor protein with a weakly-bound slip state***
A. Jannasch, M. Storch, V. Bormuth, J. Howard and E. Schäffer
submitted (2012)
- ***Nanonewton optical force trap employing anti-reflection coated, high-refractive index titania microspheres***
A. Jannasch, A.F. Demirörs, P.D.J. van Oostrum, A. van Blaaderen and E. Schäffer
in print Nature Photonics (2012)
- ***Inertial effects of a small Brownian particle cause a colored power spectral density of thermal noise***
A. Jannasch^{*}, M. Mahamadeh^{*} and E. Schäffer
Physical Review Letters **107**, 228301 (2011)
- ***Measuring the complete force field of an optical trap***
M. Jahnel^{*}, M. Behrndt^{*}, A. Jannasch, E. Schäffer and S.W. Grill
Optics Letters **36**, 1260-1262 (2011)
- ***Seeded growth of titania colloids with refractive index tunability and fluorophore-free luminescence***
A.F. Demirörs, A. Jannasch, P.D.J. van Oostrum, E. Schäffer, A. Imhof and A. van Blaaderen
Langmuir **27**, 1626-1634 (2011)

* these authors contributed equally to the work

Bibliography

- [1] J. Kepler 'Harmonices Mundi' (1619).
- [2] J. C. Maxwell 'A treatise on electricity and magnetism' (1873).
- [3] G. F. Hull and E. F. Nichols 'A preliminary communication on the pressure of heat and light radiation' *Phys. Rev.* **13**, 293 (1901).
- [4] P. N. Lebedev 'Untersuchungen über die Druckkräfte des Lichtes' *Ann. Phys.* **6**, 433 (1901).
- [5] A. Ashkin 'Acceleration and trapping of particles by radiation pressure' *Phys. Rev. Lett.* **24**, 156 (1970).
- [6] A. Ashkin, J. M. Dziedzic, J. E. Bjorkholm and S. Chu 'Observation of a single-beam gradient force optical trap for dielectric particles' *Opt. Lett.* **11**, 288 (1986).
- [7] A. Ashkin and J. M. Dziedzic 'Optical trapping and manipulation of viruses and bacteria' *Science* **235**, 1517–1520 (1987).
- [8] A. Ashkin, J. M. Dziedzic and T. Yamane 'Optical trapping and manipulation of single cells using infrared laser beams' *Nature* **330**, 769–771 (1987).
- [9] S. Chu, J. E. Bjorkholm, A. Ashkin and A. Cable 'Experimental observation of optically trapped atoms' *Phys. Rev. Lett.* **57**, 314–317 (1986).
- [10] W. D. Phillips, P. L. Gould and P. D. Lett 'Cooling, stopping, and trapping atoms' *Science* **239**, 877–883 (1988).
- [11] K. Svoboda and S. M. Block 'Biological applications of optical forces' *Annu Rev. Biophys. Biomol. Struct.* **23**, 247–285 (1994).
- [12] A. Ashkin 'Optical trapping and manipulation of neutral particles using laser' *Proc. Natl. Acad. Sci. U.S.A.* **94**, 4853–4860 (1997).
- [13] K. C. Neuman and S. M. Block 'Optical trapping' *Rev. Sci. Instrum.* **75**, 2787–2809 (2004).
- [14] D. G. Grier 'Optical tweezers in colloid and interface science' *Curr. Opin. Colloid Interface Sci.* **2**, 264–270 (1997).
- [15] D. G. Grier 'A revolution in optical manipulation' *Nature* **424**, 810–816 (2003).
- [16] A. D. Mehta, M. Rief, J. A. Spudich, D. A. Smith and R. M. Simmons 'Single-molecule biomechanics with optical methods' *Science* **283**, 1689–1695 (1999).

- [17] C. Bustamante, Z. Bryant and S. B. Smith 'Ten years of tension: single-molecule DNA mechanics' *Nature* **421**, 423–427 (2003).
- [18] E. Schäffer, S. Nørrelykke and J. Howard 'Surface forces and drag coefficients of microspheres near a plane surface measured with optical tweezers' *Langmuir* **23**, 3654–3665 (2007).
- [19] L. P. Ghislain, N. A. Switz and W. W. Webb 'Measurement of small forces using an optical trap' *Rev. Sci. Instrum.* **65**, 2762–2768 (1994).
- [20] F. Gittes and C. F. Schmidt 'Volume 55: Laser tweezers in cell biology' *Methods Cell Biol.* (1998).
- [21] A. Pralle, M. Prummer, E. L. Florin, E. H. K. Stelzer and J. K. H. Hörber 'Three-dimensional high-resolution particle tracking for optical tweezers by forward scattered light' *Microsc. Res. Tech.* **44**, 378–386 (1999).
- [22] A. Rohrbach and E. H. K. Stelzer 'Three-dimensional position detection of optically trapped dielectric particles' *App. Phys.* **91**, 5474–5488 (2002).
- [23] K. C. Neuman and A. Nagy 'Single-molecule force spectroscopy: optical tweezers, magnetic tweezers and atomic force microscopy' *Nat. Meth.* **5**, 491–505 (2008).
- [24] Y. Harada and T. Asakura 'Radiation forces on a dielectric sphere in the Rayleigh scattering regime' *Opt. Comm.* **124**, 529–541 (1996).
- [25] A. Ashkin 'Forces of a single-beam gradient laser trap on a dielectric sphere in the ray optics regime' *Biophys. J.* **61**, 569–582 (1992).
- [26] D. Vossen, A. van der Horst, M. Dogterom and A. van Blaaderen 'Optical tweezers and confocal microscopy for simultaneous three-dimensional manipulation and imaging in concentrated colloidal dispersions' *Rev. Sci. Instrum.* **75**, 2960–2970 (2004).
- [27] P. A. Maia Neto and H. M. Nussenzveig 'Theory of optical tweezers' *Europhys. Lett.* **50**, 702–708 (2000).
- [28] J. D. Jackson 'Classical Electrodynamics' *Wiley & Sons, New York, 2nd edition* (1975).
- [29] C. F. Bohren and D. R. Huffman 'Absorption and scattering of light by small particle' *Wiley-VCH* (2004).
- [30] H. C. van de Hulst 'Light scattering by small particle' *Dover Publications, New York* (1957).
- [31] K. N. Liou 'An introduction to atmospheric radiation' *Academic Press, International geophysics series* **84**, (2002).
- [32] A. Mazolli, P. A. Maia Neto and H. M. Nussenzveig 'Theory of trapping forces in optical tweezers' *Proceed. of the Roy. Soc. A* **459**, 3021–3041 (2003).
- [33] G. Gouesbet, B. Maheu and G. Grehan 'Light scattering from a sphere arbitrarily located in a Gaussian beam, using a Bromwich formulation' *J. Opt. Soc. Am. A* **5**, 1427 (1988).
- [34] A. Rohrbach and E. H. K. Stelzer 'Optical trapping of dielectric particles in arbitrary fields' *J. Opt. Soc. Am. A* **18**, 839–853 (2001).

- [35] A. Rohrbach 'Stiffness of optical traps: Quantitative agreement between experiment and electromagnetic theory' *Phys. Rev. Lett.* **95**, 168102 (2005).
- [36] J. A. Lock, S. Y. Wrbanek and K. E. Weiland 'Scattering of a tightly focused beam by an optically trapped particle' *Appl. Opt.* **45**, 3634–3645 (2006).
- [37] T. A. Nieminen, V. L. Loke, A. B. Stilgoe, G. Knöner, A. M. Branczyk, N. R. Heckenberg and H. Rubinsztein-Dunlop 'Optical tweezers computational toolbox' *J. Opt. A* **9**, S196–S203 (2007).
- [38] T. A. Nieminen, H. Rubinsztein-Dunlop and N. R. Heckenberg 'Multipole expansion of strongly focussed laser beams' *J. Quant. Spectrosc. Radiat. Transfer* **79-80**, 1005–1017 (2003).
- [39] T. A. Nieminen, H. Rubinsztein-Dunlop and N. R. Heckenberg 'Calculation of the T-matrix: general considerations and application of the point-matching method' *J. Quant. Spectrosc. Radiat. Transfer* **79-80**, 1019–1029 (2003).
- [40] P. C. Waterman 'Symmetry, unitarity, and geometry in electromagnetic scattering' *Phys. Rev. D* **3**, 825–839 (1971).
- [41] M. I. Mishchenko, L. D. Travis and A. A. Lacis 'Scattering, absorption, and emission of light by small particles' *Cambridge University Press* (2002).
- [42] T. A. Nieminen, N. R. Heckenberg and H. Rubinsztein-Dunlop 'Computational modeling of optical tweezers' *Proceed. of SPIE* **5541**, 514–523 (2004).
- [43] C. Mätzler 'MATLAB functions for Mie scattering and absorption version 2' *Institute of Applied Physics, University of Bern IAP Research Report* (2002).
- [44] E. Fällman and O. Axner 'Design for fully steerable dual-trap optical tweezers' *Appl. Opt.* **36**, 2107–2113 (1997).
- [45] V. Bormuth, J. Howard and E. Schäffer 'LED illumination for video-enhanced DIC imaging of single microtubules' *J. Microsc.* **226**, 1–5 (2007).
- [46] M. Mahamdeh and E. Schäffer 'Optical tweezers with millikelvin precision of temperature-controlled objectives and base-pair resolution' *Opt. Express* **17**, 17190–17199 (2009).
- [47] M. Mahamdeh, C. Pérez Campos and E. Schäffer 'Under-filling trapping objectives optimizes the use of the available laser power in optical tweezers' *Opt. Express* **19**, 11759–11768 (2011).
- [48] Y. Huang, J. Wan, M-C. Cheng, Z. Zhang, S. M. Jhiang and C-H. Menq 'Three-axis rapid steering of optically propelled micro/nanoparticles' *Rev. Sci. Instrum.* **80**, 063107 (2009).
- [49] S. F. Tolic-Nørrelykke, E. Schäffer, J. Howard, F. S. Pavone, F. Jülicher and H. Flyvbjerg 'Calibration of optical tweezers with positional detection in the back focal plane' *Rev. Sci. Instrum.* **77**, 103101 (2006).
- [50] K. Berg-Sørensen and H. Flyvbjerg 'Power spectrum analysis for optical tweezers' *Rev. Sci. Instrum.* **75**, 594–612 (2004).
- [51] M. Jahnel, M. Behrndt, A. Jannasch, E. Schäffer and S. W. Grill 'Measuring the complete force field of an optical trap' *Opt. Lett.* **36**, 1260–1262 (2011).

- [52] C. Bustamante, Y. R. Chemla and J. R. Moffitt 'High-resolution dual-trap optical tweezers with differential detection' *CSH Protocols* **10**, 72 (2009).
- [53] A. C. Richardson, S. N. S. Reihani and L. B. Oddershede 'Non-harmonic potential of a single beam optical trap' *Opt. Express* **16**, 15709–15717 (2008).
- [54] F. Gittes and C. F. Schmidt 'Interference model for back-focal-plane displacement detection in optical tweezers' *Opt. Lett.* **23**, 7–9 (1998).
- [55] K. Dholakia and T. Cizmar 'Shaping the future of manipulation' *Nat. Photon.* **5**, 335–342 (2011).
- [56] M. Padgett and R. Bowman 'Tweezers with a twist' *Nat. Photon.* **5**, 343–348 (2011).
- [57] J. Glückstad 'Optical manipulation: Sculpting the object' *Nat. Photon.* **5**, 7–8 (2011).
- [58] F. M. Fazal and S. M. Block 'Optical tweezers study life under tension' *Nat. Photon.* **5**, 318–321 (2011).
- [59] S. B. Smith, Y. Cui and C. Bustamante 'Overstretching B-DNA: The elastic response of individual double-stranded and single-stranded DNA molecules' *Science* **271**, 795–799 (1996).
- [60] B. Maier, L. Potter, M. So, H. S. Seifert and M. P. Sheetz 'Single pilus motor forces exceed 100 pN' *Proc. Natl. Acad. Sci. U.S.A.* **99**, 16012–16017 (2002).
- [61] M. C. Leake, D. Wilson, M. Gautel and R. M. Simmons 'The elasticity of single titin molecules using a two-bead optical tweezers assay' *Biophys. J.* **87**, 1112–1135 (2004).
- [62] J. Dong, C. E. Castro, M. C. Boyce, M. J. Lang and S. Lindquist 'Optical trapping with high forces reveals unexpected behaviors of prion fibrils' *Nat. Struct. Mol. Biol.* **17**, 1422–1430 (2010).
- [63] E. Peterman, F. Gittes and C. F. Schmidt 'Laser-induced heating in optical traps' *Biophys. J.* **84**, 1308–1316 (2003).
- [64] N. B. Simpson, D. McGloin, K. Dholakia, L. Allen and M. J. Padgett 'Optical tweezers with increased axial trapping efficiency' *J. Modern Opt.* **45**, 1943–1949 (1998).
- [65] M. L. Juan, M. Righini and R. Quidant 'Plasmon nano-optical tweezers' *Nat. Photon.* **5**, 349–356 (2011).
- [66] S. N. Reihani and L. B. Oddershede 'Optimizing immersion media refractive index improves optical trapping by compensating spherical aberrations' *Opt. Lett.* **32**, 1998–2000 (2007).
- [67] V. Bormuth, A. Jannasch, M. Ander, C. M. van Katz, A. van Blaaderen, J. Howard and E. Schäffer 'Optical trapping of coated microspheres' *Opt. Express* **16**, 13831–13844 (2008).
- [68] Y. Hu, T. A. Nieminen, N. R. Heckenberg and H. Rubinsztein-Dunlop 'Antireflection coating for improved optical trapping' *J. App. Phys.* **103**, 093119 (2008).
- [69] A. van der Horst, P. D. J. van Oostrum, A. Moroz, A. van Blaaderen and M. Dogterom 'High trapping forces for high-refractive index particles trapped in dynamic arrays of counterpropagating optical tweezers' *Appl. Opt.* **47**, 3196–3202 (2008).

- [70] E. Hecht 'Optics, 4th. edition' *Addison Wesley* (2002).
- [71] M. Born and E. Wolf 'Principles of optics' *Cambridge University Press, seventh edition* (1999).
- [72] A. F. Demirörs, A. Jannasch, P. D. J. van Oostrum, E. Schäffer, A. Imhof and A. van Blaaderen 'Seeded growth of titania colloids with refractive index tunability and fluorophore-free luminescence' *Langmuir* **27**, 1626–1634 (2011).
- [73] S. Walheim, E. Schäffer, J. Mlynek and U. Steiner 'Nanophase-separated polymer films as high-performance antireflection coatings' *Science* **283**, 520–522 (1999).
- [74] H. K. Yu, G.-R. Yi, J.-H. Kang, Y.-S. Cho, V. N. Manoharan, D. J. Pine and S.-M. Yang 'Surfactant-assisted synthesis of uniform titania microspheres and their clusters' *Chem. Mater.* **20**, 2704–2710 (2008).
- [75] S. Eiden-Assmann, J. Widoniak and G. Maret 'Synthesis and characterization of porous and nonporous monodisperse colloidal TiO₂ particles' *Chem. Mater.* **16**, 6–11 (2004).
- [76] S.-H. Lee, Y. Roichman, G.-R. Yi, S.-H. Kim, S.-M. Yang, A. van Blaaderen, P. D. J. van Oostrum and D. G. Grier 'Characterizing and tracking single colloidal particles with video holographic microscopy' *Opt. Express* **15**, 18275–18282 (2007).
- [77] A. Jannasch, M. Mahamdeh and E. Schäffer 'Inertial effects of a small Brownian particle cause a colored power spectral density of thermal noise' *Phys. Rev. Lett.* **107**, 228301 (2011).
- [78] J. Moffitt, Y. R. Chemla, K. Aathavan, S. Grimes, P. J. Jardine, D. L. Anderson and C. Bustamante 'Intersubunit coordination in a homomeric ring ATPase' *Nature* **457**, 446–450 (2009).
- [79] B. Geiseler and L. Fruk 'Bifunctional catechol based linkers for modification of TiO₂ surfaces' *J. Mater. Chem.* **22**, 735–741 (2012).
- [80] T. Franosch, M. Grimm, M. Belushkin, F. Mor, G. Foffi, L. Forró and S. Jeney 'Resonances arising from hydrodynamic memory in Brownian motion' *Nature* **478**, 85–88 (2011).
- [81] P. Galajda and P. Ormos 'Complex micromachines produced and driven by light' *Appl. Phys. Lett.* **78**, 249–251 (2001).
- [82] D. Palima, A. R. Bañas, G. Vizsniczai, L. Kelemen, P. Ormos and J. Glückstad 'Wave-guided optical waveguides' *Opt. Express* **20**, 2004–2014 (2012).
- [83] G. E. Uhlenbeck and L. S. Ornstein 'On the theory of the Brownian motion' *Phys. Rev.* **36**, 823–841 (1930).
- [84] P. Hänggi and P. Jung 'Colored noise in dynamical systems' *Adv. Chem. Phys.* **89**, 239–326 (2007).
- [85] R. F. Fox and G. E. Uhlenbeck 'Contributions to non-equilibrium thermodynamics. I. Theory of hydrodynamical fluctuations' *Phys. Fluids* **13**, 1893–1902 (1970).
- [86] T. S. Chow and J. J. Hermans 'Effect of inertia on the Brownian motion of rigid particles in a viscous fluid' *J. Chem. Phys.* **56**, 3150–3154 (1972).

- [87] E. H. Hauge and A. Martin-Löf 'Fluctuating hydrodynamics and Brownian motion' *J. Stat. Phys.* **7**, 259–281 (1973).
- [88] D. Bedeaux and P. Mazur 'Brownian motion and fluctuating hydrodynamics' *Physica* **76**, 247–258 (1974).
- [89] Y. Pomeau and P. Résibois 'Time dependent correlation functions and mode-mode coupling theories' *Phys. Rep.* **19**, 63–139 (1975).
- [90] L. D. Landau and E. M. Lifshits 'Fluid mechanics' *Butterworth-Heinemann* (1987).
- [91] B. J. Alder and T. E. Wainwright 'Velocity autocorrelations for hard spheres' *Phys. Rev. Lett.* **18**, 988–990 (1967).
- [92] K. Berg-Sørensen and H. Flyvbjerg 'The colour of thermal noise in classical Brownian motion: a feasibility study of direct experimental observation' *New J. Phys.* **7**, 38 (2005).
- [93] H. Mao, J. R. Arias-Gonzalez, S. B. Smith, I. Tinoco and C. Bustamante 'Temperature control methods in a laser tweezers system' *Biophys. J.* **89**, 1308–1316 (2005).
- [94] S. M. van Netten 'Hydrodynamics of the excitation of the cupula in the fish canal lateral line' *J. Acoust. Soc. Am.* **89**, 310–319 (1991).
- [95] J. C. M. Gebhardt, T. Bornschlögl and M. Rief 'Full distance-resolved folding energy landscape of one single protein molecule' *Proc. Natl. Acad. Sci. U.S.A.* **107**, 2013–2018 (2010).
- [96] M. Hinczewski, Y. Hansen and R. R. Netz 'Deconvolution of dynamic mechanical networks' *Proc. Natl. Acad. Sci. U.S.A.* **107**, 21493–21498 (2010).
- [97] http://en.wikipedia.org/wiki/Colors_of_noise 'Colors of noise' *modified on 6 August at 16:02* (2011).
- [98] B. Alberts, A. Johnson, J. Lewis, K. Ra and P. Walter 'Molecular Biology of the Cell, 4th edition' *Garland Science* (2002).
- [99] F. Gittes, B. Mickey, J. Nettleton and J. Howard 'Flexural rigidity of microtubules and actin filaments measured from thermal fluctuations in shape' *J. Cell Biol.* **120**, 923–934 (1993).
- [100] J. Howard 'Mechanics of motor proteins & the cytoskeleton' *Sinauer Associates* (2001).
- [101] T. Mitchison and M. Kirschner 'Dynamic instability of microtubule growth' *Nature* **312**, 232–237 (1984).
- [102] A. Desai and T. J. Mitchison 'Microtubule polymerization dynamics' *Annu. Rev. Cell Dev. Biol.* **13**, 83–117 (1997).
- [103] J. Howard and A. A. Hyman 'Dynamics and mechanics of the microtubule plus end' *Nature* **422**, 753–758 (2003).
- [104] A. A. Hyman, S. Salser, D. N. Drechsel, N. Unwin and T. J. Mitchison 'Role of GTP hydrolysis in microtubule dynamics: information from a slowly hydrolyzable analogue, GMPCPP' *Mol. Biol. Cell* **3**, 1155–1167 (1992).

- [105] G. J. Brouhard, J. H. Stear, T. L. Noetzel, J. Al-Bassam, K. Kinoshita, S. C. Harrison, J. Howard and A. A. Hyman 'XMAP215 is a processive microtubule polymerase' *Cell* **132**, 79–88 (2008).
- [106] J. Helenius, G. Brouhard, Y. Kalaidzidis, S. Diez and J. Howard 'The depolymerizing kinesin MCAK uses lattice diffusion to rapidly target microtubule ends' *Nature* **441**, 115–119 (2006).
- [107] V. Varga, J. Helenius, K. Tanaka, A. A. Hyman, T. U. Tanaka and J. Howard 'Yeast kinesin-8 depolymerizes microtubules in a length-dependent manner' *Nat. Cell Biol.* **8**, 957–962 (2006).
- [108] M. I. Mayr, S. Hümmer, J. Bormann, T. Grüner, S. Adio, G. Woehlke and T. U. Mayer 'The human kinesin Kif18A is a motile microtubule depolymerase essential for chromosome congression' *Curr. Biol.* **17**, 488–498 (2007).
- [109] V. Varga, C. Leduc, V. Bormuth and J. Diez 'Kinesin-8 motors act cooperatively to mediate length-dependent microtubule depolymerization' *Cell* **138**, 1174–1183 (2009).
- [110] M. K. Gardner, M. Zanic, C. Gell, V. Bormuth and J. Howard 'Depolymerizing kinesins Kip3 and MCAK shape cellular microtubule architecture by differential control of catastrophe' *Cell* **147**, 1092–1103 (2011).
- [111] J. Al-Bassam, R. S. Ozer and D. Safer 'MAP2 and tau bind longitudinally along the outer rigdes of microtubule protofilament' *J. Cell Biol.* **157**, 1187–1196 (2002).
- [112] C. J. Lawrence, R. K. Dawe, K. R. Christie, D. W. Cleveland, S. C. Dawson, S. A. Endow, L. S. B. Goldstein, H. V. Goodson, N. Hirokawa, J. Howard et al. 'A standardized kinesin nomenclature' *J. Cell Biol.* **167**, 19–22 (2004).
- [113] H. Miki, Y. Okada and N. Hirokawa 'Analysis of the kinesin superfamily: insights into structure and function' *Trends Cell Biol.* **15**, 467–476 (2005).
- [114] J. Howard 'Molecular motors: structural adaptations to cellular functions' *Nature* **389**, 561–567 (1997).
- [115] L. C. Kapitein, E. J. G. Peterman, B. H. Kwok, J. H. Kim, T. M. Kapoor and C. F. Schmidt 'The bipolar mitotic kinesin Eg5 moves on both microtubules that it crosslinks' *Nature* **435**, 114–118 (2005).
- [116] N. Tokai, A. Fujimoto-Nishiyama, Y. Toyoshima, S. Yonemura, S. Tsukita, J. Inoue and T. Yamamota 'Kid, a novel kinesin-like DNA binding protein, is localized to chromosomes and the mitotic spindle' *EMBO J.* **15**, 457–467 (1996).
- [117] R. A. Walker, E. D. Salmon and S. A. Endow 'The Drosophila claret segregation protein is a minus-end directed motor molecule' *Nature* **347**, 780–782 (1990).
- [118] K. Svoboda and S. M. Block 'Force and velocity measured for single kinesin molecules' *Cell* **77**, 773–784 (1994).
- [119] S. M. Block, L. S. Goldstein and B. J. Schnapp 'Bead movement by single kinesin molecules studied with optical tweezers' *Nature* **348**, 348 (1990).
- [120] K. Svoboda, C. F. Schmidt, B. J. Schnapp and S. M. Block 'Direct observation of kinesin stepping by optical trapping interferometry' *Nature* **365**, 721–727 (1993).

- [121] J. Howard 'The movement of kinesin along microtubules' *Annu. Rev. Physiol.* **58**, 703–729 (1996).
- [122] C. L. Asbury, A. N. Fehr and S. M. Block 'Kinesin moves by an asymmetric hand-over-hand mechanism' *Science* **302**, 2130–2134 (2003).
- [123] A. N. Fehr, C. L. Asbury and S. M. Block 'Kinesin steps do not alternate in size' *Biophys. J.* **94**, 20–22 (2008).
- [124] M. J. Schnitzer and S. M. Block 'Kinesin hydrolyses one ATP per 8-nm step' *Nature* **388**, 386–390 (1997).
- [125] D. L. Coy, M. Wagenbach and J. Howard 'Kinesin takes 8-nm steps for each ATP that it hydrolyzes' *J. Biol. Chem.* **274**, 3667–3671 (1999).
- [126] S. Rice, A. W. Lin, D. Safer, C. L. Hart, N. Naber, B. O. Carragher, S. M. Cain, E. Pechatnikova, E. M. Wilson-Kubalek, M. Whittaker et al. 'A structural change in the kinesin motor protein that drives motility' *Nature* **402**, 778–784 (1999).
- [127] S. Uemura and S. Ishiwata 'Loading direction regulates the affinity of ADP for kinesin' *Nat. Struct. Biol.* **10**, 308–311 (2003).
- [128] A. Yildiz, M. Tomishige, A. Gennerich and R. D. Vale 'Intramolecular strain governs kinesin stepping behavior along microtubules' *Cell* **134**, 1030 (2008).
- [129] T. Wittmann, A. Hyman and A. Desai 'The spindle: a dynamic assembly of microtubules and motors' *Nat. Cell Biol.* **3**, 28–34 (2001).
- [130] G. Goshima, R. Wollman, N. Stuurman, J. M. Scholey and R. D. Vale 'Length control of the metaphase spindle' *Curr. Biol.* **15**, 1979–1988 (2005).
- [131] M. K. Gardner, D. J. Odde and K. Bloom 'Kinesin-8 molecular motors: putting the brakes on chromosome oscillations' *Trends Cell Biol.* **18**, 307–310 (2008).
- [132] L. E. Hough, A. Schwabe, M. G. Glaser, J. R. McIntosh and M. D. Betterton 'Microtubule depolymerization by the kinesin-8 motor Kip3p: A mathematical model' *Biophys. J.* **96**, 3050–3064 (2009).
- [133] Y. Du, C. A. English and R. Ohi 'The kinesin-8 Kif18A dampens microtubule plus-end dynamics' *Curr. Biol.* **20**, 374–380 (2010).
- [134] C. Peters, K. Brejc, L. Belmont, A. J. Bodey, Y. Lee, M. Yu, J. Guo, R. Sakowicz, J. Hartman and C. A. Moores 'Insight into the molecular mechanism of the multi-tasking kinesin-8 motor' *EMBO J.* **29**, 3437–3447 (2010).
- [135] M. I. Mayr, M. Storch, J. Howard and T. U. Mayer 'A non-motor microtubule binding site is essential for the high processivity and mitotic function of kinesin-8 Kif18A' *PLoS ONE* **6**, e27471 (2011).
- [136] X. Su, W. Qiu, M. L. Gupta Jr., J. B. Pereira-Leal, S. L. Reck-Peterson and D. Pellman 'Mechanisms underlying the dual-mode regulation of microtubule dynamics by Kip3/kinesin-8' *Mol. Cell* **43**, 751–763 (2011).
- [137] J. Stumpff, Y. Du, C. A. English, Z. Maliga, M. Wagenbach, C. L. Asbury, L. Wordeman and R. Ohi 'A tethering mechanism controls the processivity and kinetochore-microtubule plus-end enrichment of the kinesin-8 Kif18A' *Mol. Cell* **43**, 764–775 (2011).

- [138] J. Stumpff, G. Dassow, M. Wagenbach, C. L. Asbury and L. Wordeman 'The kinesin-8 motor Kif18A suppresses kinetochore movements to control mitotic chromosome alignment' *Develop. Cell* **14**, 252–262 (2008).
- [139] L. N. Weaver, S. C. Ems-McClung, J. R. Stout, C. LeBlanc, S. L. Shaw, M. K. Gardner and C. E. Walczak 'Kif18A uses a microtubule binding site in the tail for plus-end localization and spindle length regulation' *Curr. Biol.* **21**, 1500–1506 (2011).
- [140] R. D. Vale, T. Funatsu, D. W. Pierce, L. Romberg, Y. Harada and T. Yanagida 'Direct observation of single kinesin molecules moving along microtubules' *Nature* **380**, 451–453 (1996).
- [141] A. B. Kolomeisky and M. E. Fisher 'Molecular motors: A theorist's perspective' *Annu. Rev. Phys. Chem.* **58**, 675–695 (2007).
- [142] V. Bormuth 'Optimized optical tweezers to study the mechanics of kinesin-8: stepping, slipping, protein friction' *PhD thesis* (2008).
- [143] V. Bormuth, V. Varga, J. Howard and E. Schäffer 'Protein friction limits diffusive and directed movements of kinesin motors on microtubules' *Science* **325**, 870–873 (2009).
- [144] B. Brenner, M. Schoenberg, J. M. Chalovich, L. E. Greene and E. Eisenberg 'Evidence for cross-bridge attachment in relaxed muscle at low ionic-strength' *Proc. Natl. Acad. Sci. U.S.A.* **79**, 7288–7291 (1982).
- [145] T. Guérin, J. Prost, P. Martin and J. F. Joanny 'Coordination and collective properties of molecular motors: theory' *Curr. Opin. Cell Biol.* **22**, 14–20 (2010).
- [146] J. Gorman and E. C. Greene 'Visualizing one-dimensional diffusion of proteins along DNA' *Nat. Struct. Mol. Biol.* **15**, 768–774 (2008).
- [147] L. C. Kapitein, B. H. Kwok, J. S. Weinger, C. F. Schmidt, T. M. Kapoor and E. J. G. Peterman 'Microtubule cross-linking triggers the directional motility of kinesin-5' *J. Cell Biol.* **182**, 421–428 (2008).
- [148] J. R. Cooper and L. Wordeman 'The diffusive interaction of microtubule binding proteins' *Curr. Opin. Cell Biol.* **21**, 68–73 (2009).
- [149] M. M. Bradford 'A rapid and sensitive method for the quantitation of microgram quantities of protein utilizing the principle of protein-dye binding' *Anal. Biochem.* **72**, 248–254 (1976).
- [150] V. Varga 'Characterization of *Saccharomyces cerevisiae* kinesin-8 by single-molecule fluorescence microscopy' *PhD thesis* (2008).
- [151] G. T. Hermanson 'Bioconjugate techniques' *Academic Press* (2008).
- [152] J. N. Israelachvili 'Intermolecular & surface forces, Second Edition' *Academic Press* (1991).
- [153] G. Charvin, D. Bensimon and V. Croquette 'On the relation between noise spectra and the distribution of time between steps for single molecular motors' *Single Mol.* **3**, 43 (2002).
- [154] N. Thomas, Y. Imafuku and K. Tawada 'Molecular motors: thermodynamics and the random walk' *Proc. R. Soc. Lond. B* **268**, 2113–2122 (2001).

- [155] M. Bugiel 'Protofilament switching of kinesin-8 investigated with optical tweezers' *Diploma thesis* (2011).
- [156] Y. Okada and N. Hirokawa 'Mechanism of the single-headed processivity: Diffusional anchoring between the K-loop of kinesin and the C terminus of tubulin' *Proc. Natl. Acad. Sci. U.S.A.* **97**, 640–645 (2000).
- [157] M. T. Valentine, P. M. Fordyce, T. C. Krzysiak, S. P. Gilbert and S. M. Block 'Individual dimers of the mitotic kinesin motor Eg5 step processively and support substantial loads in vitro' *Nat. Cell Biol.* **8**, 470–476 (2006).
- [158] H. Yardimci, M. van Duffelen, Y. Mao, S. S. Rosenfeld and P. R. Selvin 'The mitotic kinesin CENP-E is a processive transport motor' *Proc. Natl. Acad. Sci. U.S.A.* **105**, 6016–6021 (2008).
- [159] M. Brunnbauer, F. Mueller-Planitz, S. Kösem, T. H. Ho, R. Dombi, J. C. M. Gebhardt, M. Rief and Z. Ökten 'Regulation of a heterodimeric kinesin-2 through an unprocessive motor domain that is turned processive by its partner' *Proc. Natl. Acad. Sci. U.S.A.* **107**, 10460–10465 (2010).
- [160] M. Tomishige, D. R. Klopfenstein and R. D. Vale 'Conversion of Unc104/KIF1A kinesin into a processive motor after dimerization' *Science* **297**, 2263–2267 (2002).
- [161] J. Howard 'Protein power strokes' *Curr. Biol.* **16**, R517–R519 (2006).
- [162] B. E. Clancy, W. M. Behnke-Parks, J. O. L. Andreasson, S. S. Rosenfeld and S. M. Block 'A universal pathway for kinesin stepping' *Nat. Struct. Mol. Biol.* **18**, 1020–1027 (2011).
- [163] A. Farré, F. Marsà and M. Montes-USategui 'Optimized back-focal-plane interferometry directly measures forces of optically trapped particles' *Opt. Express* **20**, 12270–12291 (2012).

Thanks to...

This project was a wonderful experience for me. I want to say thank you to many people who contributed directly or indirectly to this work.

I want to say thank you to Erik Schäffer for giving me the possibility to work in his group, for his advices, support and commitment to making sure this project was a success. Erik's enthusiasm, perfectionism, deep understanding of physics and his never ending knowledge and experiences formed me over time. Thank you Erik for supervising and having always an open ear for me!

A special thank you goes to the people of the Nanomechanics group: Mohammed (Master of 'Aswad', for a lot of philosophical discussions and doing the colored noise project together), Marcel, Avin (for nice indian evenings and continuing with 'Pinky'), Michael (the other Kip3 guy, for the nice beer hours), Mario and Elisa (the LabView souls), Steve, Tobias and Christine (for teaching me some biology), Mohammad, Gero and Heike. Furthermore, I want to thank the former lab members Adrian, Deepikaa, Freddy, and Magdalena. You guys make the Lab a great place to work.

I want to say thank you to Joe Howard for his support, expertise and advice. I want to thank the whole Howard group for always providing an excellent atmosphere and for great support. I'm deeply grateful to Volker Bormuth who instructed me in the kinesin-8 project, Marko Storch for teaching me a lot of biological crafts and Anastasiya Trushko for discussions. It was a great pleasure to work with you together.

I am grateful to Alfons van Blaaderen for hosting me some month in his group where I enjoyed the great atmosphere and worked together with Ahmet F. Demirörs on the synthesis of the titania particles. Thank you Ahmet for your help in the lab and the introduction into wet chemistry. Thank you also to Peter van Oostrum for doing some optical tweezers calculations and for great scientific discussions.

I want to say thank you to Marcus Jahnel, Martin Behrndt and Stephan Grill for the great collaboration on the complete force field project.

I want to say thank you to my reviewers Joe Howard and Stefan Diez for taking the time to read this thesis. Furthermore, I want to thank Stefan Diez and Michael Schroeder for examine me in my Rigorosum.

I want to thank you Ralf Seidel and his group for great discussions.

Thanks to Erik, Michael and Marko for carefully proof reading of this thesis.

That is just a part of the whole story. I would like to thank all the people who accompanied me during my PhD time: Friedrich für die vielen kreativen Pausen. Ich hätte mir keinen besseren Nachbarn in unserem überschaubaren Büro vorstellen können. Simone,

Daniel und Matthias, dass ihr mich zu etlichen Kickerspielen entführt habt. Colditzer, Manu und Martin für die spannend Skatabende. Gunnar, für die etlichen Essen die ich zu später Stund bei dir geniessen durfte. Peter, Bienchen, Jörg, Gunnar, Jokkel und Martin für die heldenhaften und waghalsigen Abenteuer die ich mit euch erleben durfte. Marko, Veikko, Gunnar, Jörg, Susann und vielen mehr für eure Freundschaft. Roxana, multumesc mult de tot pentru prietenia ta.

Martin, mein Engel und kleiner Psycho, vielen Dank fuer deine Liebe mit der du mich unterstützt hast und ohne die ich heute nicht die wäre die ich bin.

Zu guter Letzt danke ich den Menschen, die mich seit knapp 30 Jahren begleiten und unterstützen. Liebe Familie vielen Dank für eure Liebe, dass ihr immer für mich da wart und an mich geglaubt habt.

Live long and prosper!